

Cover Page



Universiteit Leiden



The handle <http://hdl.handle.net/1887/63238> holds various files of this Leiden University dissertation.

Author: Castellanos Nash, P.

Title: Breaking & Entering : PAH photodissociation and top-down chemistry

Issue Date: 2018-06-28

Breaking & Entering
PAH photodissociation and top-down chemistry

P. Castellanos Nash

ISBN/EAN: 978-94-028-1068-4

Cover design by P. Castellanos.

Original cover image by S. Burkard.

The images on the top-right corner of odd pages are intended to create a flipbook animation. This represents an idealized example of hydrogen roaming along the edge of a PAH (ovalene in this case). From a classical PAH, one hydrogen moves to create an aliphatic group in the same ring, later it jumps to a tertiary carbon, only to end up in a neighbouring ring. Afterwards, the process is reversed to end up with the original PAH.

BREAKING & ENTERING
PAH PHOTODISSOCIATION AND TOP-DOWN CHEMISTRY

PROEFSCHRIFT

ter verkrijging van
de graad van Doctor aan de Universiteit Leiden,
op gezag van de Rector Magnificus Prof. mr. C. J. J. M. Stolker,
volgens besluit van het College voor Promoties
te verdedigen op donderdag 28 juni 2018
klokke 11:15 uur

door
Pablo Castellanos Nash
geboren te La Habana, Cuba
in 1987

Promotiecommissie

Promotor: Prof. dr. A. G. G. M. Tielens

Promotor: Prof. dr. H. V. J. Linnartz

Overige leden: Prof. dr. C. Joblin (*Paul Sabatier University*)
Prof. dr. J. Oomens (*Radboud University*)
Prof. dr. E. Peeters (*University of Western Ontario*)
Prof. dr. H. J. A. Röttgering (*Leiden University*)
Prof. dr. P. P. van der Werf (*Leiden University*)

A mi familia, con y sinsanguínea

“No importa el resultado, sólo el esfuerzo vale.”
— MIGUEL DE CERVANTES, Don Quijote

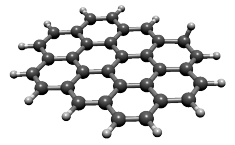
INDEX

I	INTRODUCTION	1
1.1	Astrochemistry and organic inventory	4
1.2	Historical overview on interstellar PAHs	9
1.3	Observational characterization of PAHs	13
1.3.1	Photodissociation regions	14
1.3.2	Spectral variations of PAHs	16
1.4	Top-down chemistry	17
1.5	Research methods	19
1.5.1	Theoretical studies	20
1.5.2	Laboratory studies	21
1.6	Experimental set-up	22
1.6.1	Quadrupole ion-trap	22
1.6.2	Mass isolation	24
1.6.3	Time-of-flight mass spectrometry	25
1.7	Thesis contents	28
1.8	Outlook	29
II	FULLERENES IN PHOTODISSOCIATION REGIONS	31
2.1	Introduction	32
2.2	Sources	34
2.2.1	NGC 2023	34
2.2.2	Ced 201	36
2.2.3	RCW 49	37
2.2.4	Additional sources	39
2.3	Data	39
2.3.1	IRS Data	39

Index

2.3.2	PACS Data	40
2.4	Analysis	40
2.4.1	Spectral fit	40
2.4.2	Spectral maps	43
2.4.3	UV field calculation	45
2.4.4	The atomic hydrogen density	49
2.4.5	Carbon fraction variations	50
2.5	Discussion	53
2.6	Conclusions	55
III FORMATION OF FULLERENES FROM PAHS		59
3.1	Introduction	60
3.2	Experimental methods	61
3.3	Results	61
3.4	Discussion	65
3.5	Astrophysical relevance	66
3.6	Conclusion	67
IV PHOTOINDUCED PAH DEHYDROGENATION		69
4.1	Introduction	70
4.2	Experimental methods	71
4.3	Theoretical methods	74
4.3.1	Density functional theory calculations	74
4.3.2	Reaction rates	74
4.3.3	Monte-Carlo simulations	75
4.4	Results	75
4.4.1	Experiments	76
4.4.2	Dehydrogenation channels and isomerization	81
4.4.3	Monte-Carlo simulations	83
4.5	Discussion	92
4.6	Conclusions	94
4.A	Monte-Carlo with tertiary H-hopping	96
V MOLECULAR HYDROGEN FORMATION IN PDRS		99
5.1	Introduction	100
5.2	Methods	101
5.3	Results	103
5.4	Discussion and Conclusions	107
BIBLIOGRAPHY		111

NEDERLANDSE SAMENVATTING	119
ENGLISH SUMMARY	123
RESUMEN EN CASTELLANO	127
PUBLICATIONS	131
CURRICULUM VITAE	133
ACKNOWLEDGMENTS	135



I

INTRODUCTION

“Lo que se abre ante nuestros ojos es el mundo anterior al hombre. Abajo, en los grandes ríos, quedaron los saurios monstruosos, las anacondas, los peces con tetas, los laulaus cabezones, los escualos de agua dulce, los gimnotos y lepidosirenas que todavía cargan con su estampa de animales prehistóricos, legado de las dragonadas del Terciario. Aquí, aunque algo huya bajo los helechos arborescentes, aunque la abeja trabaje en las cavernas, nada parece saber de seres vivientes. Acaban de apartarse las aguas, aparecida es la Seca, hecha es la yerba verde, y, por primera vez, se prueban las lumbreras que habrán de señorear en el día y en la noche. Estamos en el mundo del Génesis al fin del Cuarto Día de la Creación. Si retrocediéramos un poco más, llegaríamos adonde comenzara la terrible soledad del Creador — la tristeza sideral de los tiempos sin incienso y sin alabanzas, cuando la tierra era desordenada y vacía y las tinieblas estaban sobre la faz del abismo.”

— ALEJO CARPENTIER, Los pasos perdidos.

I. Introduction

Not a hundred years have passed since the discovery of the very first interstellar molecule — methylidyne (CH; Swings & Rosenfeld 1937) — and, to date, more than 200 different molecules have been detected, either in the gas phase, or as ices around dust grains.¹ Of these, polycyclic aromatic hydrocarbons (PAHs) are among the largest, most stable species detected thus far (Tielens 2008). PAHs are a family of molecules characterized by a graphene-like skeleton of carbon atoms with hydrogens terminating the edge of the molecules. They are identified through their common mid-infrared (mid-IR) emission features that are seen towards most lines of sight, but are specially prominent in regions with strong ultraviolet (UV) fields. This is aided by their high stability, as they can survive better than other species when subjected to harsh radiation.

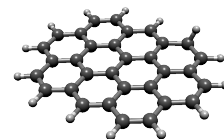
The interest in interstellar molecules is not only limited to the chemical reactions involved in their formation and destruction, but is also related to astrophysics in general. Line emission/absorption and certain chemical processes are related to the physical conditions of the environment. As such, the molecular inventory acts as a tracer of temperatures, densities and other physical parameters that would be otherwise hard to probe.

The vast majority of the molecular species detected in space contain carbon and hydrogen atoms, signifying the important role of organic chemistry in understanding the molecular diversity of the universe. From simple chains, up to the largest observed carbon cage-like molecules, these species play a determinant role as the base for the chemistry and biology that eventually takes place on planetary systems (Herbst & van Dishoeck 2009, and references therein). The chemical pathways available in the interstellar medium (ISM) that can lead to the formation of these molecules are radically different from those commonly found on Earth. Under typical interstellar conditions of extremely low densities and temperatures, and a near constant bombardment of high energy photons, the survival of any type of chemical compounds must be accounted for when trying to understand the initial chemical makeup of newly formed planets.

For most complex molecules, direct formation via atomic or molecular reactions in the gas phase of the ISM has been proven to be highly inefficient and, as a consequence of this, alternative pathways have been proposed and investigated (Berné & Tielens 2012). The formation mechanism most commonly considered relies on reactions taking place in the ice mantles of interstellar dust grains. Such ices act as a reservoir of molecules as well as a third body capable of absorbing the excess formation energy, effectively catalyzing surface reactions even at low temperatures (Tielens 2013, and references therein). Indeed, a combination of experiments and modeling of ice mediated formation routes has led to successfully explaining the abundance of a multitude of molecules. Nevertheless, there remains the question of the chemical evolution in regions where a higher temperature and UV-field would quench to the formation of the same ice mantles. In such environments, “bottom-up” formation schemes — merging small species to create larger ones — are less effective. All this, combined with trends that speak of active formation of molecules within environments extremely hostile to this pathway, beg for the search of different types of reactions.

The detection of fullerenes and small hydrocarbons within photodissociation regions

¹<http://www.astro.uni-koeln.de/cdms/molecules>



(PDRs; Sellgren et al. 2010; Boersma et al. 2012), supports the case for a formation pathway involving the photodestruction of larger precursor species. The mid-IR bands of fullerenes in particular, show a clear increase in intensity as the radiation field of the PDR becomes harsher. This is coupled with a decrease of other mid-IR bands associated with PAHs, which have been postulated as a starting point in the origin of fullerenes in PDRs (Berné & Tielens 2012). The connection of PAHs and fullerenes has led to the suggestion of an alternative formation route in the ISM, involving unimolecular photodissociation of fairly stable species (such as large PAHs). This “top-down” interstellar chemistry can give rise to fullerenes, PAH derivatives — such as dehydrogenated species or hydrocarbon chains — and can even contribute to the formation of H_2 . Given that both the bottom-up and top-down processing mechanisms can occur at different evolutionary stages or, to an extent, in tandem, it must be stressed here that they should not be considered as independent and separated processes. For instance, the small hydrocarbon products of PAH dissociation can, after drifting to a different interstellar environment, be incorporated in ice mantles and act as previously unavailable precursors for a new generation of molecules (Tielens 2013).

In order to study these processes, astronomical observations cannot be used as a single, isolated tool. A variety of laboratory techniques have been proven successful in investigating a variety of solid state and gas phase reactions, providing critical parameters that can be compared to observational data (Wiesenfeld et al. 2018). These parameters include reaction rates, spectroscopic information and the characterization of the involved reaction networks. In addition, these experiments can also shed light into processes not previously considered, which have historically helped in reconciling apparent contradictions between model predictions and observations. The development of the field of experimental astrochemistry has been crucial for such advances. While the contributions from chemistry into astronomy cannot be overstated, the characterization of molecules and compounds under the exotic conditions of the ISM are not an obvious avenue of research within that field. The continued advancement within astrochemistry not only allow for the interpretation of astronomical data, but also sheds light into the working of chemical reactions that are simply not available within an earthbound context.

Much progress has been made in mimicking the conditions of a variety of interstellar environments but, even under the most favorable of circumstances, they only provide an approximation to the actual physical conditions encountered within the ISM. In particular, the timescales involved in most astronomical processes are completely beyond the realm of experimental feasibility. It is in bridging these gaps that modeling tools become not only relevant, but absolutely essential for understanding the large scale impact of molecular processing. Furthermore, quantum chemical calculations have continuously helped in understanding the molecular characteristics that contribute to the reactions observed within experimental works and in predicting how similar molecules will behave in a manner that is more time efficient than rigorous experiments. This is not to say that continued experiments are no longer required, given that the validity of the trends derived in this manner needs to be carefully scrutinized and corroborated (Wiesenfeld et al. 2018).

The overall goal of this thesis is to gain new experimental, theoretical and observa-

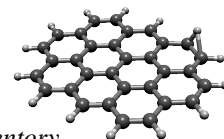
1. Introduction

tional knowledge of the photofragmentation of PAHs and their relation to interstellar top-down chemistry. The focus will be on the identification of stable photoproducts and the characterization of the main reactions leading to them. In particular, we will explore the formation of both fullerenes and molecular hydrogen. A chemical connection between PAHs and fullerenes has indeed been suggested before, but further exploration of this hypothesis, together with experimental evidence for this process, is presented here. The production of H_2 in dense PDRs has proven to be an elusive question, with observational estimates of the formation rate differing by as much as an order of magnitude with respect to the processes taken into account (Habart et al. 2004). The first step in the photofragmentation of PAHs involves their dehydrogenation, with one of its possible pathways including the release of an H_2 molecule as part of the process (Ling et al. 1995; Zhen et al. 2014). We study here the significance of this fragmentation channel and present its relevance for molecular hydrogen production in the ISM.

This introduction will expand on the topics touched upon thus far, detailing the astronomical context and main questions regarding the interstellar organic inventory in general and PAHs in particular. A brief historical overview on the development of the PAH hypothesis and related species will be provided as well, together with future research prospects involving the next generation of space telescopes. We will also discuss the variations observed in the mid-IR spectra of interstellar PAHs and how they have been related to subfamilies within the broader category of aromatic molecules. Theoretical and experimental results related to trends within PAHs will follow, as well as a discussion of their excitation/deexcitation mechanisms and the fragmentation pathways that have been characterized up to this point. Finally, we will delve into the top-down formation route, linking together the information thus far presented within this introduction as a launching pad for the main topics discussed within this thesis.

1.1. ASTROCHEMISTRY AND ORGANIC INVENTORY

Figure 1.1 shows a non-exhaustive sample of the molecules that have been detected in the ISM, as well as how the number of identifications has evolved over time. From the first detections at the end of the 30's, there were barely any new molecules reported until the 70's, when the rate of positive identifications exploded and with 4–5 new identifications per year has remained nearly constant since then. The first generation of molecules observed (CH , CH^+) were detected through their absorption in the visible spectrum, although the lack in theoretical and experimental data delayed the confirmation of these detections (McKellar 1940). The great increase in the total number of molecules identified from the 70's onwards relied mostly on the refinement of radioastronomy, as well as on an extended catalog of molecular rotational transitions, thus allowing for the detection of the first true polyatomic molecule, formaldehyde (H_2CO ; Zuckerman et al. 1970). These early identifications were dependent on the observation of rotational transitions, which are found at millimeter/submillimeter wavelengths. However, this is not the only spectral range within which molecular transitions can be found. The infrared hosts a variety of vibrational and rovibrational transitions of different molecules, although vibrational bands are more sensitive to the nature of spe-



1.1. Astrochemistry and organic inventory

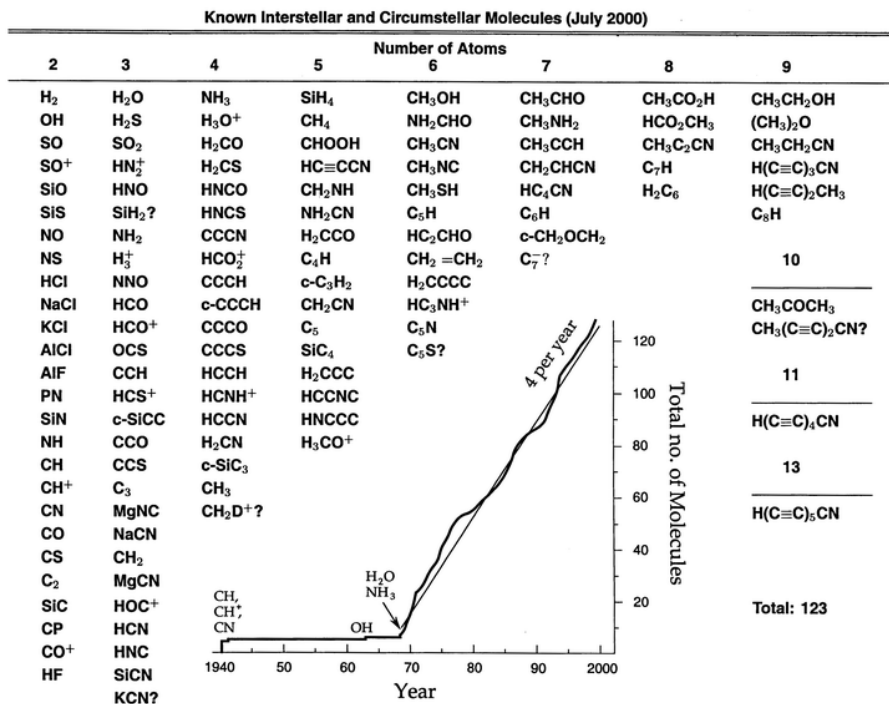


Figure 1.1.: List of molecules detected in interstellar and circumstellar material up to the year 2000, organized by the number of atoms in the molecule in question. Note that all molecules with six or more atoms contain at least one carbon in their structure. The inset shows the evolution in the number of molecules discovered as a function of year (Figure taken from Thaddeus & McCarthy 2001).

cific bonds within the molecule rather than the full molecular structure (Badger 1934). The development of infrared astronomy has progressed more slowly, due to the atmosphere being opaque to a large part of this range of the electromagnetic spectrum and thus generally requiring observations from space or with very high altitude telescopes.

The molecules identified thus far in the ISM reveal a large range of chemical reactions and atoms involved in the molecular complexity of the universe. Nevertheless, a clear trend is apparent from Fig. 1.1; carbon bearing molecules dominate the overall population of detected species, particularly towards larger masses. No molecule with six or more atoms lacking carbon has up to date been identified, making organic chemistry a prominent field within astrochemistry. This is not due to any particular kind of bias in the detected molecules, but it is to be expected due to interstellar abundances and the atomic properties of carbon. Being the fourth most abundant element in the universe — behind hydrogen, helium and oxygen — the ubiquitousness of organic molecules is no surprise. Further cementing the preponderance of carbon bearing molecules is the possibility for carbon to create large complex molecules and bond in a

I. Introduction

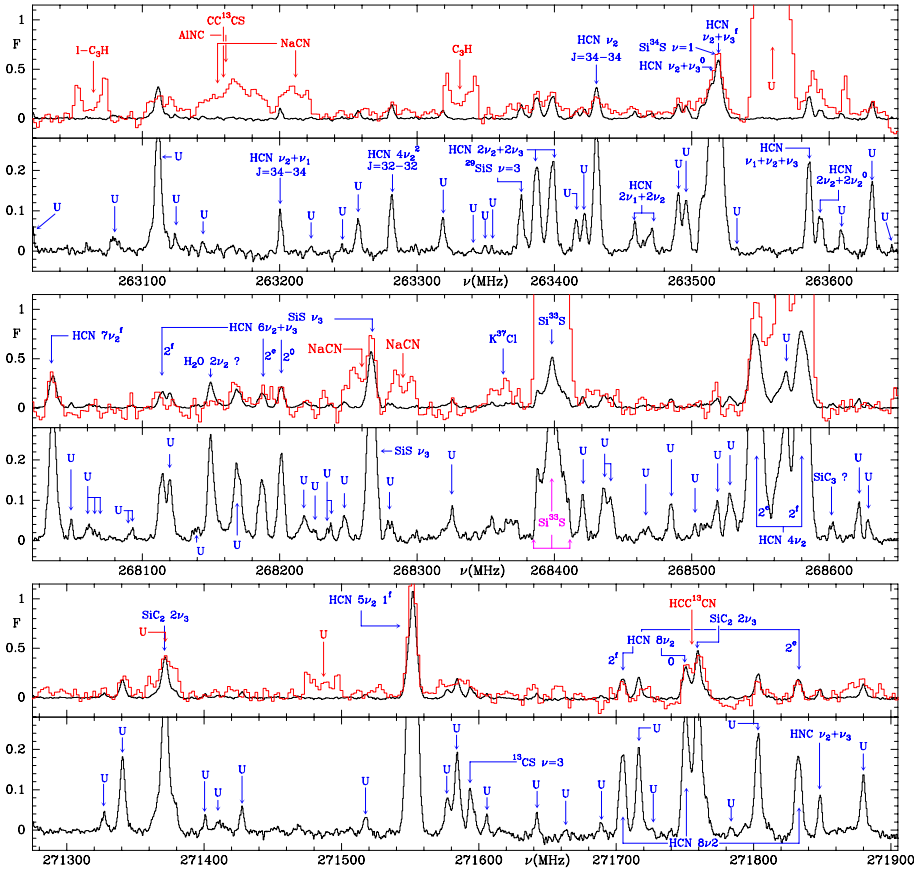


Figure 1.2.: Comparison of ALMA (black) and 30-m IRAM spectra (red) of IRC+10216. The intensity scale is in units of Jy beam^{-1} . The bottom panel shows a zoom-in of the ALMA observations. Molecular transitions labeled in red were detected with the single dish of IRAM, but filtered out by the ALMA interferometer. Lines labeled U correspond to emission lines as of yet unidentified (Figure taken from Cernicharo et al. 2013).

variety of forms. This very same property has made organic chemistry so determinant for the formation and evolution of complex life here on Earth. In recent years, a wide arrange of complex organic molecules have been detected in space, including a sugar (glycolaldehyde, HOCH_2CHO ; Jørgensen et al. 2012), a simple amino-acid (glycine, $\text{NH}_2\text{CH}_2\text{COOH}$; Kuan et al. 2003) — although this detection remains somewhat uncertain (Snyder et al. 2005) — and an example of a chiral molecule (1,2-propylene oxide, $\text{CH}_3\text{CHCH}_2\text{O}$; McGuire et al. 2016). With the advent of the ALMA interferometer, a veritable forest of weak unidentified transitions has been detected (Fig. 1.2), suggesting that further detections might be ahead.

The variety of the bonding characters available for carbon relates to the formation of hybrid orbitals, which involve the mixing of individual atomic orbitals that can later

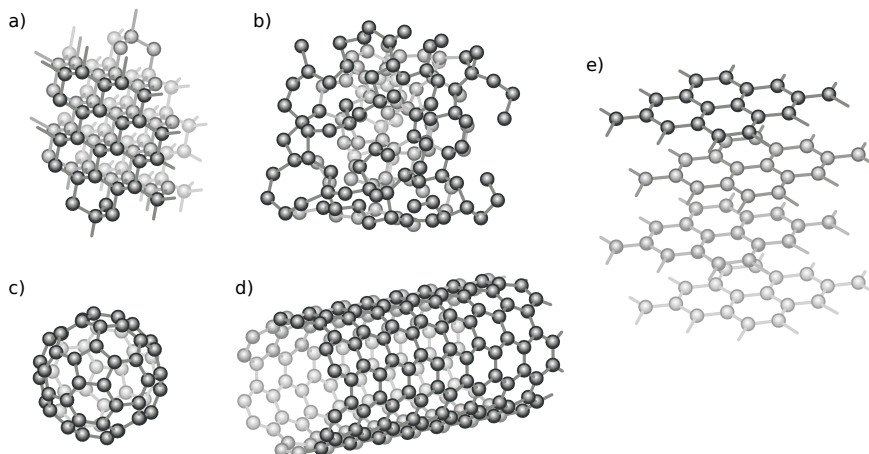
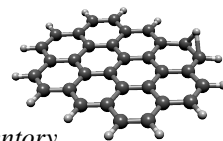


Figure 1.3.: Different allotropic forms of pure carbon materials. a) Crystalline structure of diamond, showcasing a pure sp^3 hybridization. b) Amorphous carbon can display a mixture of the three possible hybridizations, with the exact ratios depending on the particular structure. c) Buckminsterfullerene (C_{60}); the fullerene family displays sp^2 hybridization. d) Carbon nanotubes can be seen as a one-dimensional extension of fullerenes, and as such are also an example of sp^2 hybridization. e) Graphite consists on weakly bounded graphene (sp^2) sheets, which are representative of the structure of PAHs (Figure by J. Sivek/CC BY-SA 4.0).

pair electrons to form covalent bonds, with the character of the bond established by the type of hybridization involved. Carbon can be found in a variety of hybridization types, mixing a number of $2s$ and $2p$ orbitals, which in turn lead to diverse geometrical arrangements of bond structures. These hybridized orbitals include sp^3 , sp^2 and sp , which allow for the formation of four, three and two σ bonds, respectively. The remaining electrons in unhybridized atomic orbitals in the case of sp^2 and sp hybridization can be used for one or two additional π bonds, respectively. Figure 1.3 displays different allotropic forms of carbonaceous materials together with their respective hybridization. Of these, fullerenes have been conclusively detected in the ISM (Cami et al. 2010), along with diamondoids (Guillois et al. 1999) and PAHs (Allamandola et al. 1985), the hydrogenated molecular forms of diamond and graphene, respectively. The different hybridizations of carbon are also represented among the simpler carbon bearing molecules detected in the ISM. For instance, methane (CH_4) has four σ bonds and is thus both sp^3 hybridized and fully saturated, while acetylene (C_2H_2) has sp hybridization and the triple bond between the carbon atoms consists of one σ and two π bonds. Carbon molecules with double bonds are representative of sp^2 hybridized orbitals.

The case of interstellar PAHs is of particular interest for the organic inventory of the ISM. A standard PAH molecule has a honeycomb-like structure of linked hexagonal carbon rings terminated in hydrogen atoms, examples of which are presented in Fig. 1.4. This results in thousands of possible geometries, varying in size and compactness. While the identification of a specific PAH has remained elusive — barring

1. Introduction

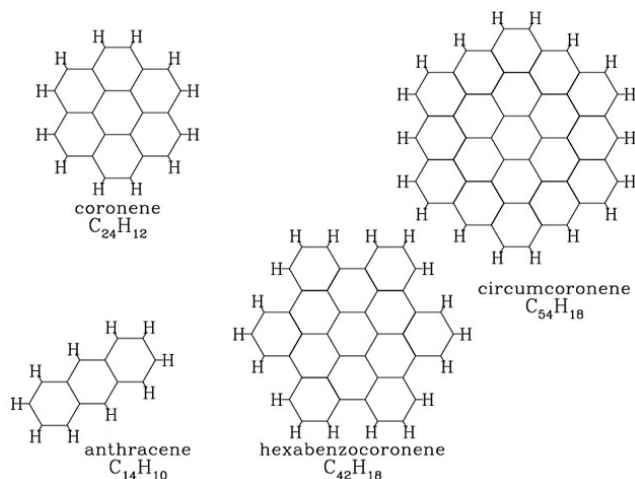
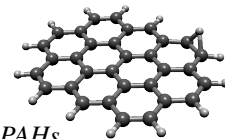


Figure 1.4.: Example of PAH molecules spanning a large range in sizes, from three fused rings (anthracene) to nineteen (circumcoronene). The hexagonal carbon rings are characteristic of standard PAHs, but modified structures with five and/or seven membered rings can also be found (Figure adapted from Draine 2010).

a tentative detection through blue fluorescence of anthracene and pyrene in the Red Rectangle (Vijh et al. 2004) —, the mid-IR spectra of most galactic objects and several extragalactic sources betrays their ubiquitous presence (Tielens 2008). The spectral characteristics of PAHs will be discussed in detail later on (Sect. 1.5.1), but suffice it to say here that their mid-IR bands are characteristic of specific atomic bonds rather than of particular molecules. PAHs are among the largest molecules found in the ISM, containing about 50–100 C-atoms each and observational evidence suggests that they lock up to 10–20% of all elemental carbon (Allamandola et al. 1989). Besides their near universal presence in the ISM, laboratory studies indicate that they can form more complex organic molecules through hydrogenation, oxygenation and hydroxylation when locked up in ices, paving the way towards amino-acids and other biological molecules (Gudipati & Yang 2012). PAH evolution in the gas phase has also sparked considerable interest, as they are postulated to be a starting point for top-down interstellar chemistry (Berné & Tielens 2012), as their fragmentation can give rise to a variety of molecules not accessible through solid state reactions (a more in-depth view into this mechanism will be provided in Sect. 1.4).

PAHs are not only relevant for astronomy on the grounds of their involvement in the chemistry of the ISM, but also because they can act as tracers for the physical conditions of the variety of regions where they are found. PAHs, specially as their size increases, have relatively low ionization potentials, making them a primary source of electrons in PDRs, where most of the atomic gas is neutral. This, coupled with their efficient recombination with electrons, in turn sets the ionization balance of the neutral medium of the galaxy. The ionization of PAHs is also determinant in controlling the



1.2. Historical overview on interstellar PAHs

energy balance of HI regions, via the photoelectric effect, which is known to be the dominant heating mechanism in these regions (Hollenbach & Tielens 1999). While the photoelectric effect from prototypical dust grains also takes part in heating the neutral medium, the heating efficiency is dominated by the lower end of the size distribution, which is thought to overlap with that of the largest PAHs.

The mid-IR emission bands from PAHs are also used to trace the hardness of the UV-field. These bands are emitted by vibrationally excited PAHs cascading down to their ground state following the absorption of an energetic far-UV photon originating from the interstellar radiation field. The absorbed photon will directly lead to an excited electronic state, the energy is then transferred into the vibrational modes via internal conversion and intramolecular vibrational redistribution in a short timescale of $\sim 10^{-9}$ s (Allamandola et al. 1989). This connection between PAH emission and the intensity of the UV-field has proven particularly useful for tracing star forming regions in high redshift galaxies (Genzel et al. 1998). Signs of PAH emission can help distinguish between excitation due to active galactic nuclei (AGNs) and that due to massive stellar formation (Pope et al. 2007). Thus far this technique has allowed for the identification of star forming galaxies up to $z \sim 3$, but the imminent launch of the *James Webb Space Telescope (JWST)* is expected to push this limit much farther back.

As remarkable as the progress of the last fifty or so years has been, several lingering questions remain within astrochemistry in general, and PAHs in particular. Laboratory evidence suggests that the formation of biomolecules such as amino-acids is indeed feasible under interstellar conditions, observational confirmation on the presence of such species is still lacking (Nuevo et al. 2014). There is as well the issue of up to what extent molecular complexity can develop in the ISM prior to planet formation and, perhaps more importantly, which species can survive and effectively be delivered to newly formed planets along the evolutionary stages of collapsing dense clouds, proto-planetary disks and the formation of young stellar objects and new planetary systems (Kwok 2016, and references therein). PAHs are a crucial piece of this puzzle given their widespread presence in the ISM and the significant amount of carbon locked up in them. The processing of PAHs under UV radiation holds the potential to open up previously unconsidered chemical pathways and may deliver the precursors of biologically significant species (Tielens 2013). The studies presented in this thesis focus on such processing, in order to examine which products are the most stable ones, to study the details of the reactions that can produce them and what is their impact on interstellar chemistry.

1.2. HISTORICAL OVERVIEW ON INTERSTELLAR PAHs

While the origin of IR astronomy can be traced back all the way to the 19th century, its development in earnest had to wait until the 1960's and 1970's (Rieke 2009). A fundamental step in this direction came with the use of airborne telescopes, such as the Kuiper Airborne Observatory (KAO Cameron 1976), and later with space based telescopes, such as the *Infrared Astronomical Satellite (IRAS)*; Neugebauer et al. 1984). Spectroscopic observations with ground based telescopes and KAO showed from early

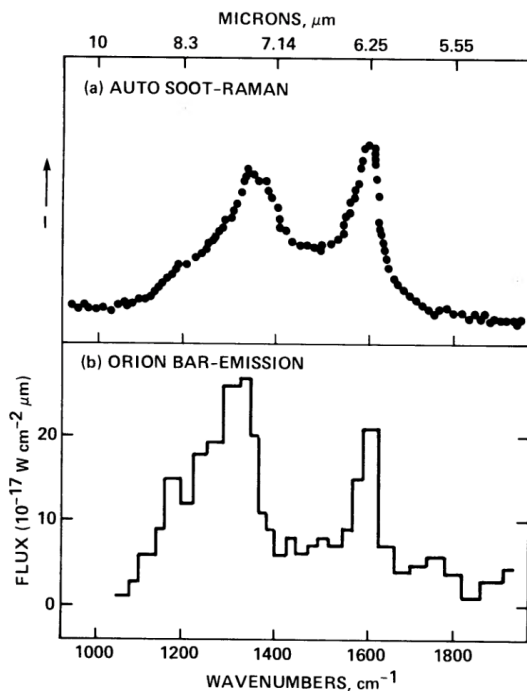
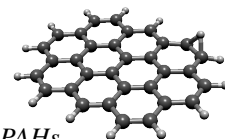


Figure 1.5.: Comparison of an experimental Raman spectrum of soot from a car exhaust, which is dominated by emission of PAHs (Rosen & Novakov 1978) (a), and astronomical observations of the Orion bar reflection nebula (b) in the 5 to 10 μm spectral range (Bregman et al. 1983) (Figure taken from Allamandola et al. 1985).

on a series of previously unknown emission bands, with the strongest found at 3.3, 6.2, 7.7, 8.6 and 11.2 μm (Gillett et al. 1973; Russell et al. 1977). These emission bands were dubbed the unidentified infrared bands (UIB). Additionally, an excess emission was detected with *IRAS*, most prominently in the band at 12 μm (Aumann et al. 1984). This mid-IR excess could not be explained by dust in radiative equilibrium alone, since this could only be explained with unrealistically high dust grain temperatures. A population of very small grains (VSGs) were proposed to account for the observation, given that the low heat capacity would transiently excite these molecules to high temperatures. As such, this grain population would not be in radiative equilibrium, but rather be stochastically heated (Sellgren 1984; Léger & Puget 1984). The VSG hypothesis required a range in grain sizes corresponding to a few hundred atoms, which could more properly be considered large molecules

The presence of aromatic molecules in the ISM had already been proposed in the form of the carriers of the UV extinction bump at 2175 Å (Draine & Lee 1984). However, the interest in this family of molecules was renewed with the realization that they fulfilled the main tenants of the VSG hypothesis (Léger & Puget 1984). A crucial step forward in identifying PAHs as the carriers of the UIBs came from the comparison of



1.2. Historical overview on interstellar PAHs

astronomical spectra to laboratory experiments on soot from car exhaust, as shown in Fig. 1.5 (Allamandola et al. 1985). The exhaust gases consist of a mixture of PAHs and other graphitic material, which are known to be the result of incomplete combustion (Rosen & Novakov 1978). This positive identification helped bringing along collaborations with experimentalist and theoretical chemists. The combined efforts of these disciplines have resulted in a vast spectroscopic database of different PAHs and related species, all of which support the connection between the mid-IR bands and PAHs (e.g., Boersma et al. 2014; Hudgins & Sandford 1998; Oomens et al. 2006). As the evidence mounted, and the PAH hypothesis started gathering widespread acceptance, the UIBs came to be known as the aromatic infrared bands (AIB). It must be noted though, that a fair share of criticism has also been leveled at the hypothesis, with carriers such as hydrogenated amorphous carbon (HAC) being proposed as an alternative (Zhang & Kwok 2015).

Analogous to the known formation mechanism of PAHs in soot, a formation route was proposed in the shell of asymptotic giant branch (AGB) and post-AGB stars (Frenklach & Feigelson 1989; Cherchneff et al. 1992). The formation of interstellar dust in general has also been associated with these latter stages in stellar evolution, and whether the formation leads to carbonaceous or silicate based grains will depend on the C:O ratio in the envelope of these dying stars. Experiments aimed at understanding the relevance of this formation mechanism were key in identifying a new allotrope of carbon: fullerenes (Kroto et al. 1985). The prototypical icosahedral C_{60} fullerene had actually been proposed as a new molecular form of carbon in the 1970's, but it failed to gain traction in those days (see Throrer 1999, for a historical overview). It was later noticed that fullerene formation in soot-like environments was not only confined to laboratory conditions and was a much more general process (Krätschmer et al. 1990). Twenty-five years had yet to pass from the finding of fullerenes to their detection in the ISM (Fig. 1.6a; Cami et al. 2010; Sellgren et al. 2010). As was the case for PAHs, their mid-IR bands were determinant in identifying their presence in planetary nebulae (PNe) and PDRs.

Once the ubiquitousness of PAHs in the ISM had been well established, the search for evidence of electronic and rotational transitions started as well. One avenue of research was the attempt at identifying PAH signatures among the diffuse interstellar bands (DIBs) which are observed in absorption towards most stars within the galaxy (Snow 2001). DIBs have been recognized and classified since the interwar years (Heger 1922), and it has been well established that they are interstellar in origin (Merrill et al. 1937; Merrill & Sanford 1938). Electronic transitions of neutral PAHs typically fall at wavelengths shorter than those of most DIBs, but PAH cations have their main absorptions further to the red. For this reason, research connecting the DIBs and PAHs has been mostly limited to charged species (Snow et al. 1998). However, a positive match of one or more DIBs to any particular PAH has proven elusive to this day. More success has recently been found in terms of identifying fullerenes as carriers of some of the DIBs. Although C_{60}^+ was proposed as the source of two near-IR DIBs (at 9577 and 9632 Å; Foing & Ehrenfreund 1994), this first assignment was based on the results of matrix spectroscopy and thus the identification was not deemed conclusive (Maier 1994). It would not be until Campbell et al. (2015) measured the gas-phase absorption

I. Introduction

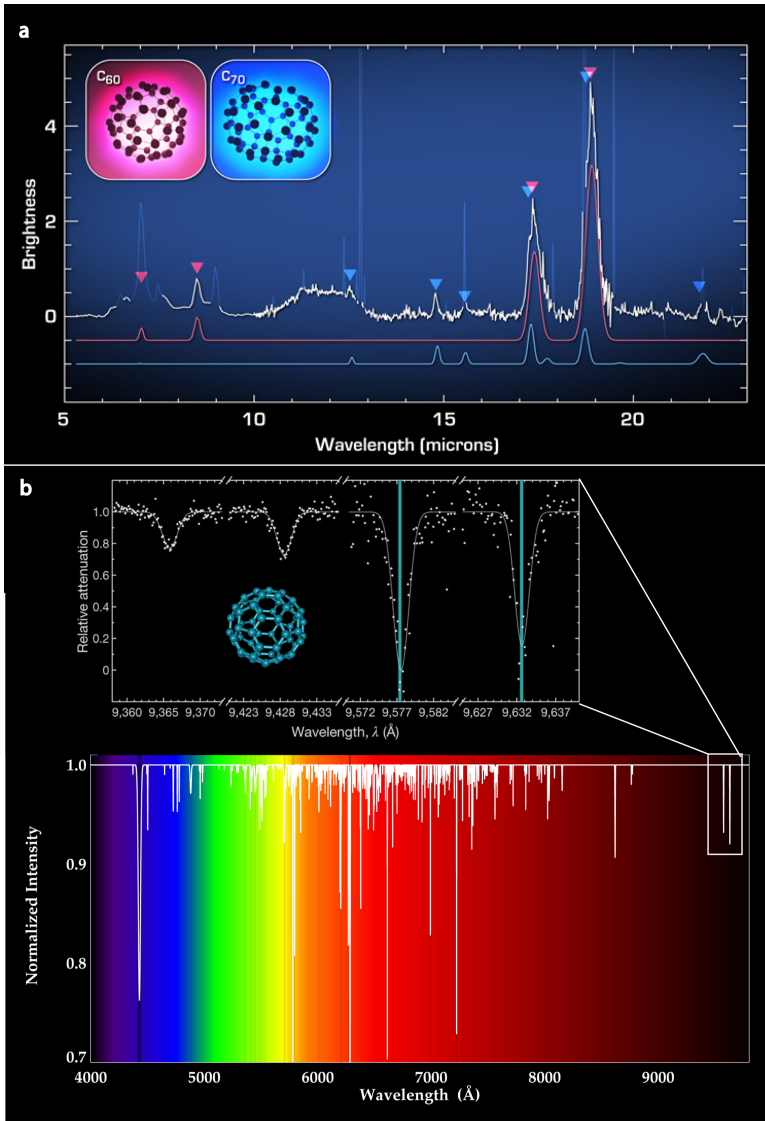
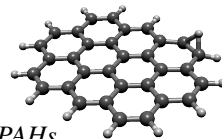


Figure 1.6.: Observational evidence for the presence of fullerenes in the ISM. a) *Spitzer* mid-IR spectrum of the planetary nebula Tc 1 (white), compared with theoretical spectra of the C₆₀ (red) and C₇₀ (blue) fullerenes (Cami et al. 2010). b) Near-UV to near-IR spectrum showcasing the main known DIB absorption bands. The inset presents the experimental gas-phase spectra of C₆₀⁺ with the two vertical lines highlighting the position of the DIBs first associated to these absorptions (Campbell et al. 2015). The two other experimental bands also seem to have DIB counterparts. Image credits for DIB spectrum: J. Cami; for Tc 1 spectrum: NASA/JPL-Caltech/J. Cami (Figure provided by A. Candian).



1.3. Observational characterization of PAHs

of helium tagged C_{60}^+ in a cryogenic ion trap that stronger evidence on the origin of these bands was provided (Fig. 1.6b).

The search for pure rotational transitions of PAHs presents a different type of challenge. Traditional PAHs lack a permanent dipole moment, because of their high symmetry, thus making such transitions forbidden. Nevertheless, an interest on the rotational spectroscopy of these molecules arose out of the detection of a previously undiscovered galactic foreground in observations aimed at mapping the cosmic microwave background (Leitch et al. 1997). This foreground, dubbed anomalous microwave emission (AME), peaks at around centimeter wavelengths and it has been theorized to arise from rapidly rotating VSGs (Draine & Li 2001). As was the case in the identification of the AIBs, these VSGs straddle the line between large molecules and bulk materials, and the possible contribution of PAHs to the AME has been considered from the beginning. In order to circumvent the lack of permanent dipole moment, research has focused on modified PAHs, whether through the addition of subgroups, partial fragmentation or non-planar (bowl-shaped) PAHs (Pilleri et al. 2009). As with the DIBs, an incontrovertible identification of PAHs through AME has not been possible thus far.

Although research on interstellar PAHs has not been limited to mid-IR spectroscopy, it is indubitable that this has been the most successful technique and a large part of future work on this topic remains tied to it. From the first detections of the AIBs with the instruments of KAO, advances in technology and multinational collaborations have done much in order to advance the field. The first orbital telescope with spectroscopic capability in the mid-IR was the *Infrared Space Observatory (ISO)* (Kessler et al. 1996). It helped cementing the bases of the PAH hypothesis and its higher spectral resolution allowed for the creation of a classification of AIB spectra, based on variations in band intensities and shapes. The next generation IR orbiting observatory came with the *Spitzer Space Telescope* (Werner et al. 2004), which added the capability of creating spectral maps. This tool allowed for the first time to observe AIB spectral variations within a single source, and was indispensable in establishing the relationship between the photodestruction of PAHs and the formation of fullerenes in PDRs. The imminent launch of *JWST* promises to extend on this capabilities with its improved spectral and spatial resolution.

1.3. OBSERVATIONAL CHARACTERIZATION OF PAHs

As mentioned in the previous section, observational studies have been a driving force behind our current understanding of the evolution of PAHs in space. Their resilience against photofragmentation allows for these molecules to survive for longer periods of time in a wide variety of interstellar and circumstellar environments, whereas other species are easily fragmented and revert to their atomic components when outside highly UV-shielded regions. Their mid-IR signatures have been detected in the diffuse ISM, PNe, post-AGB stars, star forming regions and protoplanetary disks, both within our galaxy and in extragalactic sources (e.g. Fig. 1.7; see Tielens 2008, and references therein). The driving physical mechanism behind IR fluorescence requires

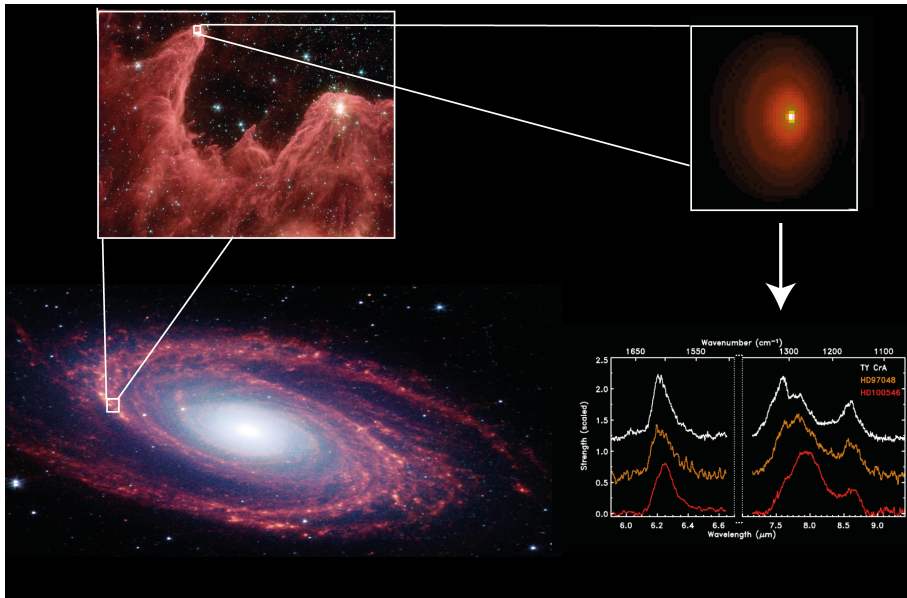
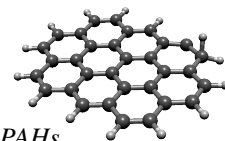


Figure 1.7.: PAHs dominate the mid-IR emission in the universe. Lower-left: Composite image of M 81 as taken by *Spitzer*. Red corresponds to emission at $8.0 \mu\text{m}$, which is dominated by PAHs. Upper-left: The Mountains of Creation in the Soul Nebula (IC 1871), with red again associated with the $8.0 \mu\text{m}$ filter of *Spitzer*. Top-right: Protoplanetary disk around HD 97048 observed with the $8.6 \mu\text{m}$ filter of the Very Large Telescope (VLT; image adapted from Doucet et al. 2007). Lower-right: PAH spectra of three different protoplanetary disks (image adapted from Boersma et al. 2008). Image credits for M 81, Mountains of Creations: NASA/JPL-Caltech/Harvard-Smithsonian CfA (Figure provided by A. Candian).

the presence of strong UV-fields for the AIBs to be observed. In addition to this, it is expected that in well shielded environments PAHs will coagulate or be incorporated into the ice mantles of dust grains. This thesis focuses on the chemical evolution of PAHs within PDRs associated with star forming regions, which begs for a description of the physical and chemical conditions most commonly found in these regions.

1.3.1. PHOTODISSOCIATION REGIONS

PDRs can be briefly described as mostly neutral regions in the ISM where intense UV-fields dominate the energy balance and chemical conditions of the gas (Hollenbach & Tielens 1997, 1999). It is within these environments that a transition from largely atomic to largely molecular gas takes place. Their structure follows a layered pattern as the gas temperature, T_{gas} , decreases, beginning from the transitional area where protons and electrons recombine into hydrogen atoms (Fig. 1.8). The first molecule to be formed is H_2 , for which the transition occurs at $A_V \simeq 2$. This zone also corresponds to the peak of PAH emission, where they are found to be mostly ionized owing to their



1.3. Observational characterization of PAHs

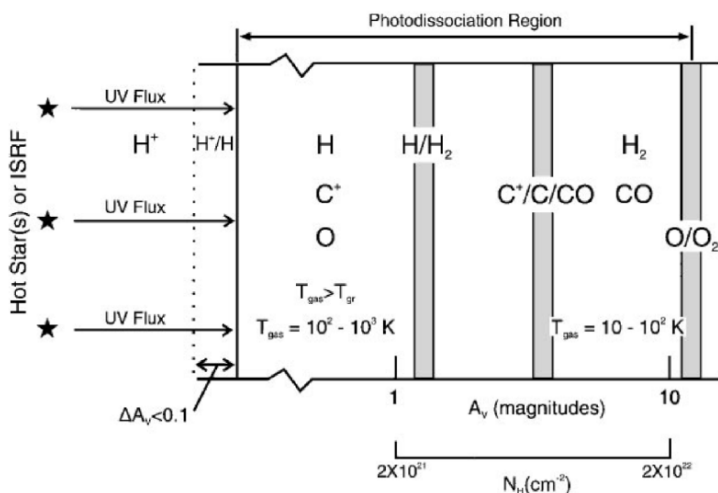


Figure 1.8.: Diagram of the typical structure of PDRs, with the HII dominated region to the left and the molecular cloud on the right. The main atomic to molecular transition regions are sketched above, together with typical gas temperatures and column densities (Figure taken from Hollenbach & Tielens 1997).

low ionization potential (typically from 6 to 10 eV). Carbon atoms also remain ionized deeper into the PDR, up to $A_V \simeq 4$, at which point they will be able to recombine and quickly react with atomic oxygen to form CO, the second most abundant interstellar molecule. The edge of the PDR on the molecular cloud side is roughly defined by the area in which the remaining oxygen can be turned into O_2 , at which point almost all the gas is in molecular form.

The aforementioned structure of the PDR is determined by the number density of the region in question, n , and the intensity of the incident UV-field expressed in units of the average UV interstellar radiation field (Habing 1968) — i.e., $G_0 = 1$ equals $1.6 \times 10^{-3} \text{ erg cm}^{-2} \text{ s}^{-1}$. Under these circumstances it is clear that the parameter G_0/n will dominate most processes within the PDR, including the ionization balance. While the term PDR is generally used to refer to the dense medium surrounding star forming regions, in reality it encompasses most of the diffuse ISM, as well as the circumstellar material irradiated by the remnants of evolved stars. The flared sections of protoplanetary disks can also be considered PDRs on their own right, as the cold molecular gas and dust in the mid-plane transition towards regions where simple molecules formed in ices can be evaporated and subsequently photodissociated.

The far-UV fields dominate most processes within PDRs but, considering the outlined structure of these regions, there are limits to the photon energies available. Photons with energies above 13.6 eV — the ionization potential (IP) of atomic hydrogen — can exclusively be found in HII regions bordering PDRs, and are thus not significant within. Carbon can remain ionized throughout a large portion of the PDR, owing to its IP being 11.3 eV, and the same is true for most PAHs. Molecular hydrogen has a

1. Introduction

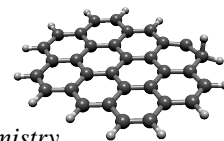
bond dissociation energy of 4.3 eV, but the H/H_2 transition happens much earlier than carbon recombination. The first electronically excited state of H_2 is unbound, but due to it being a triplet state makes the transition from the singlet ground state forbidden. As such, photodissociation goes through the absorption of a UV photon in allowed transitions (the closest one requiring 11.2 eV) followed by spontaneous emission into the vibrational continuum of the ground state (Abgrall et al. 1992). While the energy of this process is similar to that of carbon ionization, the fact that the photon absorption in the former process occurs through discrete transitions makes self-shielding efficient, as the presence of foreground H_2 molecules will use up most photons with at frequency.

PAHs are found throughout all zones in PDRs, although they are subject to different types of processes depending on their size and location. The IP of the smallest PAHs is about 7–8 eV and it decreases as the size increases. Ionization of PAHs is the most important source of gas heating within PDRs, together with photoelectric heating from dust grains (Bakes & Tielens 1994). When reaching the H_2 photodissociation front, PAH fragmentation starts to take place. As photons are absorbed and the electronic energy is transferred into the vibrational degrees of freedom, different bonds within the molecule can be severed and a series of fragments can be released. The first dissociation channels to open up involve hydrogen loss, whether atomic or molecular but, as the energy increases, carbon containing fragments can be lost as well (Jochims et al. 1994). Observations of small hydrocarbons, unaccounted for in chemical models of PDRs, suggest that they could be formed following fragmentation of PAHs (Pety et al. 2005). Additionally, the intensity of PAH bands has been observed to decrease when approaching the radiation source, while bands associated to fullerenes become more prominent (Berné & Tielens 2012).

The formation of H_2 in PDRs remain an open question. Observational constrains show a high formation rate that cannot be accounted for solely based on dust grain catalyzed reactions (Habart et al. 2004; Wakelam et al. 2017). Attempts have been made in matching the observed formation rate with reactions involving superhydrogenated PAHs, but it has been found not to be an efficient channel given the low binding energies for additional carbons (Bron et al. 2014; Andrews et al. 2016). Direct photodissociation via H_2 -loss has also been considered, but so far it relies on extrapolation of dissociation parameters of small PAHs and has failed to account for the high H_2 formation rate in PDRs (Andrews et al. 2016).

1.3.2. SPECTRAL VARIATIONS OF PAHS

The AIBs correspond to emission from vibrationally excited PAHs, with the main bands lying at 3.3, 6.2, 7.7, 8.6 and 11.2 μm . The band positions and their relative intensities carry information on the structure and ionization state of the emitting PAHs (Fig. 1.9). In the ISM, the only effective method to reach highly excited vibrational states is through photon absorption. However, in the case of PAHs and other organic molecules, direct photon absorption into vibrationally excited states is highly inefficient. The absorption of a UV photon creates an electronically excited molecule which then can then relax through several possible routes, such as ionization and collisional deexcitation. The former is important if the UV photon in question has an energy higher



1.4. Top-down chemistry

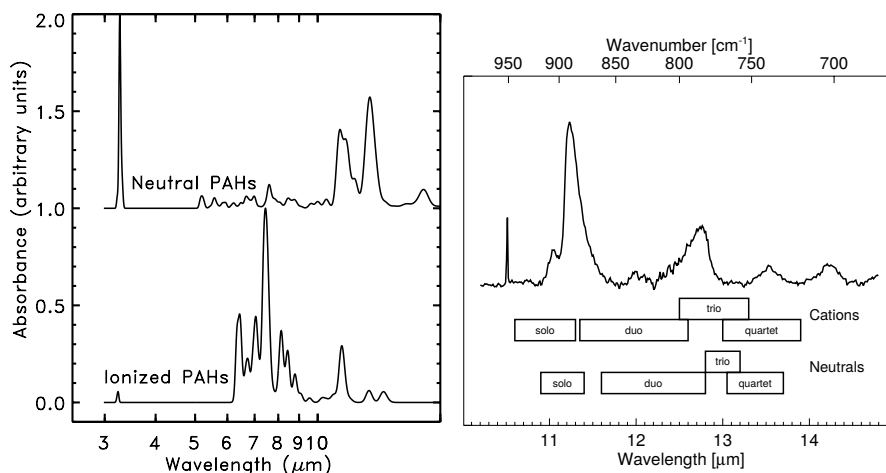


Figure 1.9.: Influence of charge and structure on the mid-IR bands of PAHs. Left: Laboratory measurements of variations in intensity due to charge. Neutral PAHs have the strongest modes in the $3 \mu\text{m}$ region (C–H in-plane modes) and $10\text{--}15 \mu\text{m}$ (C–H out-of-plane modes), while ionized PAHs are dominated by emission bands between 6 and $9 \mu\text{m}$ (C–C modes) (Figure taken from Allamandola et al. 1999). Right: Average mid-IR spectrum in the $10\text{--}15 \mu\text{m}$ region, with the band positions of C–H out-of-plane modes highlighted according to the associated edge structure (Figure taken from Hony et al. 2001).

than the IP of the particular PAH, while the latter is, as was mentioned before, usually negligible in the ISM. The PAH can rapidly ($\sim 10^{-12}$ s) undergo internal conversion (IC) into a highly vibrationally excited, lower lying electronic state. Intersystem crossing (ISC) is similar in nature to IC, but it happens at a slower rate ($\sim 10^{-9}$ s) since it involves an electronic state with a different multiplicity — e.g., from singlet to triplet states in small neutral PAHs. Both these processes are followed by intramolecular vibrational redistribution (IVR), which distributes the energy among all accessible vibrational modes in less than a nanosecond. After IVR has taken place, the relaxation process can follow through either fragmentation or IR fluorescence, which gives rise to the mid-IR band emission (Allamandola et al. 1989).

1.4. TOP-DOWN CHEMISTRY

For the most part, the formation of molecules in the ISM has focused on (ion-molecule) gas phase and solid state interactions of radicals within icy mantles surrounding dust grains. This follows a bottom-up approach, as smaller units join together to form larger compounds. This has been a fruitful research avenue, successfully reproducing observations in many cases, and providing multiple and efficient mechanisms of formation for a variety of molecules in molecular clouds, hot cores and protoplanetary disks (Herbst & van Dishoeck 2009). Furthermore, experiments aimed at reproducing

1. Introduction

reactions in interstellar ices have pointed at the possibility of forming highly complex molecules under these conditions, although they are yet to be detected (Nuevo et al. 2014). Despite this success, there are observational trends suggesting the active formation of large, complex molecules (particularly fullerenes) in environments where the deposition of atoms and molecules on ices is not effective. Ion-molecule reactions in the gas phase would also be ineffective since they would require too many steps to build up to such complex molecules. Due to this, alternative formation routes have been postulated for these species. The most prominent of such pathways — and central focus of this thesis — involves a top-down approach, with the fragmentation of large molecules leading to different products (Berné & Tielens 2012; Berné et al. 2015).

Several observational clues have hinted at the relevance of top-down chemistry, particularly within PDRs. Many small hydrocarbon chains and cyclic structures — C_2H , C_3H_2 , C_3H^+ and C_4H — have been detected towards the PDR at the edge of the Horsehead Nebula (B 33, Pety et al. 2005; Guzmán et al. 2015; Cuadrado et al. 2015). These molecules are only detected in regions of high UV photon flux and the models available failed to reproduce their presence. It was hypothesized that fragmentation of PAHs or other large, carbon bearing molecules could be responsible for the formation of these hydrocarbons. Furthermore, shortly after the discovery of fullerenes in the interstellar medium, it was realized that in NGC 7023 the fraction of carbon locked in PAHs shows a strong anticorrelation with the fraction of carbon locked in fullerenes. The increase in the population of fullerenes occurs in close proximity to the illuminating star of the PDR, again suggesting that the destruction of PAHs in particular leads to molecules whose formation in ices within these environments is highly unlikely (Berné & Tielens 2012).

The same work postulated the basis of top-down chemistry from PAHs, with the competition of fragmentation and isomerization leading to the formation of a multiple carbon and hydrocarbon molecules (Fig. 1.10). However, most of these species are highly susceptible to further dissociation, resulting in low lifetimes under interstellar conditions. For this reason, exploration into this hypothesis must by force be focused on the most stable products of PAH photofragmentation. The present formulation of top-down chemistry on the basis of fullerene observations is thus no coincidence, as these molecules are known to have high stability against dissociation. Nevertheless, other stable products can provide additional support for this type of processing. For instance, the formation of molecular hydrogen in PDRs is known to be larger than expected when considering formation on grains alone (Habart et al. 2004). Given that H_2 -loss is one of the dissociation channels associated with PAH photofragmentation, a detailed look into this process might hold the key in breaching this disparity.

Finally, photon induced top-down chemistry originating in PAHs fits within the generally accepted lifecycle of PAHs in the ISM (Andrews et al. 2015; Peeters et al. 2017). Carbonaceous grains represent a significant part of interstellar dust and are thought to be formed of amorphous carbon, with a significant graphitic fraction as inferred from the 2175 Å bump in the extinction curve. Collisions and irradiation can break down the dust grains, with the aromatic, graphite-like portions able to survive for extended periods of times. This results in a wide variety of PAHs being released into the gas phase, with different sizes and structures. The PAH population will eventually become dom-

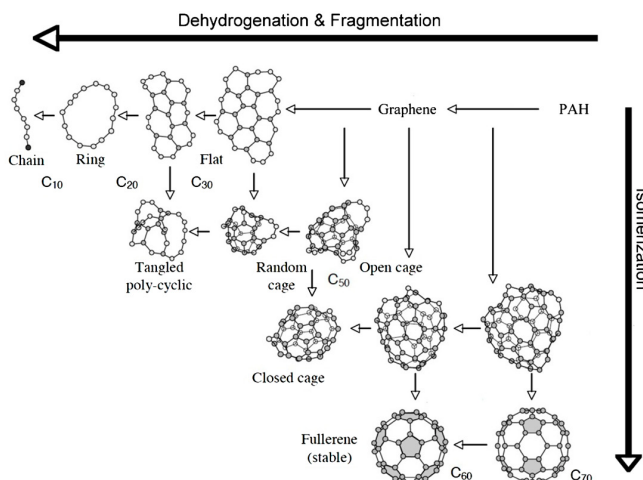
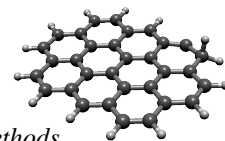


Figure 1.10.: Overview of top-down chemistry from PAHs showing possible products of PAHs through a mixture of fragmentation (right to left) and isomerization (top to bottom). Most of these fragments are themselves easily fragmented, but a few of them (such as C₆₀ and C₇₀) are stable enough to endure and build up their population. This diagram does not include secondary fragments such as H₂, C₂, C₂H₂, etc. (Figure taken from Berné & Tielens 2012).

inated by a selection of large, symmetric PAHs (grandPAHs), as only the most stable among them can withstand for long under the harsh UV irradiation. Eventually, even these grandPAHs will begin to fragment, giving rise to the aforementioned top-down chemistry, with a significant fraction of them ending up locked into fullerenes.

1.5. RESEARCH METHODS

PAHs have a range of structural characteristics which will affect their mid-IR bands and stability against photodissociation. An important factor influencing both these aspects has to do with the symmetry of PAHs, with more symmetric compact PAHs generally being more resistant to fragmentation. Symmetry also has an effect in the mid-IR bands, given that there is a larger number of IR active modes in irregular molecules. Additionally, PAHs can be found in superhydrogenated states, have heteroatom substitutions (where a carbon is replaced by another element), five-/seven-member ring defects or side-groups attached to the edge of the molecule. These deviations from a prototypical PAH decrease the molecular stability, but at the same time are the origin of spectral variations needed to account for the totality of the AIBs. For instance, superhydrogenation and/or the presence of aliphatic side-groups (which include sp^3 hybridized carbon) can account for the 3.4 μm band (Mackie et al. 2018; Tielens 2008, and references therein).

Another range of structural variations that have been studied encompass the possibility of isomerization. This includes hydride shifts, which consist of one of the peripheral

I. Introduction

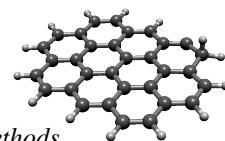
hydrogens moving along the edge of the PAH (Trinquier et al. 2017a; Alvaro Galué & Oomens 2012). However, isomerization is not limited to hydrogen roaming and can also affect the carbon skeleton. In this sense a variety of routes have been explored, including dangling ethynyl/vinyl groups and the rearrangement of rings into hepta/septa/octagons (Bouwman et al. 2016; Trinquier et al. 2017b). For isomerization reactions to take place, an energy barrier specific for the rearrangement needs to be overcome. Isomerized PAHs also display different fragmentation pathways and bond dissociation energies can change with respect to regular PAHs.

The effects of the variations outlined here are studied using a combination of theoretical and experimental techniques. All of these lead to a better understanding of the driving mechanisms in PAH fragmentation and IR emission, but it is important to keep in mind that these techniques do not evolve independently. Experimental findings guide theoretical studies, which in turn provide predictions that need to be tested in laboratory settings. The main experimental and theoretical tools used for PAH research are described in more detail here.

1.5.1. THEORETICAL STUDIES

Quantum chemical calculations have been invaluable when investigating the trends in stability and mid-IR emission associated with size and structural changes of PAHs. While experimental work is crucial in guiding and corroborating predictions from these calculations, they have technical limitations and time constraints which prevent the quick and efficient analysis of a large number of molecules. Laboratory work is limited by which molecules can be efficiently synthesized and carry a variety of instrumental effects, while quantum chemical calculations can tackle these issues on a large variety of molecular structures in a more time efficient manner. Nevertheless, theoretical calculations must be thoroughly corroborated against experiments to assess their range of validity. Among the theoretical tools available, density functional theory (DFT) is central to the work of this thesis and will be addressed in more detail. It must be noted, however, that this is by no means the only possible theoretical approach, which includes molecular dynamics and statistical methods as well.

The different energy levels within a molecule, whether electronic, vibrational or rotational, must be calculated using the Schrödinger equation. This relates the description of the kinetic and potential energy of the system to the energy values that are actually accessible. Unfortunately, none but the simplest of systems have analytic or even numerically exact solutions and thus, the use of approximations becomes imperative. In first place we have the Born-Oppenheimer approximation, which considers the nuclear motions independent from the electrons, as the former are much heavier than the latter. Using this it is possible to determine the equilibrium position for the nuclei and the electronic part of Schrödinger equation can then be solved independently. Here is where DFT comes into play, as the wavefunctions of individual electrons are replaced by an electron density, which is represented as a linear combination of functions which are part of the so called basis set. The electronic kinetic energy, together with the nuclei-electron and electron-electron interactions are then replaced by functionals of the electron density. Once this part of the equation has been solved, the nuclear po-



1.5. Research methods

sitions have to be readjusted and the process continues iteratively until convergence. There are a number of basis sets and functionals available for these calculations and the particularities of the system under consideration must be taken into account when deciding which ones to use.

The immediate result of this type of DFT calculations is the energy of the molecule. In works regarding the fragmentation of PAHs, the different bond dissociation energies (BDEs) can be calculated following this method. In the case of direct H-loss, for instance, the energy of the final structure can be obtained using the same approach. The energy of the parent molecule can then be subtracted from this value, together with the energy of the lost hydrogen atom, yielding the BDE for this particular bond cleavage. The energy of other reactions, including isomerization and loss of more complex units, can also be calculated by finding the transition state(s) involved in the reaction. This requires finding a maximum in the potential energy surface that connect the products and reactants.

DFT calculations can also be carried one step further, allowing for the calculation of the vibrational modes of the molecule. After solving for the electronic portion of Schrödinger equation, attention can be shifted back to the nuclear interactions, with the interaction potential again requiring simplifying assumptions. While recently there has been great progress in the use of anharmonic potentials, for the most part the work has been limited to a quadratic, harmonic approximation (Mackie et al. 2015; Maltseva et al. 2015). The latter generally yields a good match with experimental data once a scaling factor is applied to the computed vibrational frequencies. In this thesis, all DFT calculations are limited to using the harmonic approximation, given that anharmonic calculations are much more computationally expensive and the gain in accuracy is not critical unless high resolution comparisons are needed.

The success of DFT calculations has resulted in multiple spectral databases (Mallocci et al. 2007; Boersma et al. 2014), which in turn have guided the interpretation of astronomical mid-IR spectra. This has allowed for the classification and identification of shapes and intensities of mid-IR bands and plateaus as due to ionization, clustering and structurally different PAHs (e.g., Boersma et al. 2008; Rosenberg et al. 2014; Andrews et al. 2015).

1.5.2. LABORATORY STUDIES

Even with all the advances in quantum chemical calculations, experimental work remains crucial in testing the validity of theoretical studies and in guiding them. A wide range of experimental techniques are used to characterize different aspects of PAHs including, but not limited to, their spectra, reactivity and dissociation pathways. As usual, all of these have strengths and limitations, and it is through their combined use — with support from theory and models — that a full picture of the evolution of PAHs in space and their emission characteristics can be fully addressed.

Laboratory studies focus on (photo-)chemical reactions, exploring the dissociation channels and reactivity. The fragmentation pattern of PAHs upon irradiation has been well studied and found to always follow an overall similar pattern. The dehydrogenation shows enhanced intensity on even mass peaks with respect to odd ones (e.g., Ekern

I. Introduction

et al. 1998; Zhen et al. 2014). Whether this is due to molecular hydrogen release or a sequential loss with low barriers for odd losses has been explored as well in the case of small PAHs ($N_C \leq 24$). While the H_2 -loss pathway has indeed been detected it has generally been regarded as a minor channel with respect to sequential losses (Ling et al. 1995; Jochims et al. 1994). The process of superhydrogenation by interaction with carbon atoms has also been the subject of considerable studies, particularly as a potential pathway for H_2 formation (Thrower et al. 2012; Cazaux et al. 2016).

1.6. EXPERIMENTAL SET-UP

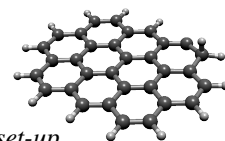
Experiments carried out as part of this thesis were performed with an in-house experimental set-up dubbed the “instrument for photodynamics of PAHs” (i-PoP; Zhen et al. 2014), which at its core consists of a commercially available quadrupole ion trap (QIT; Jordan C-1251) coupled to a time-of-flight mass spectrometer (TOF-MS; Jordan D-850). A diagram of the experimental set-up is shown in Fig. 1.11. These two units are located in separate high vacuum chambers, which are referred to as the source chamber and the detection chamber, respectively. Within the source chamber, the PAH/fullerene sample of interest is evaporated from an oven (Heat Wave Labs) by adjusting the temperature to that where the molecule under consideration begins to gently sublime. The oven temperature is monitored using a thermocouple and the power supply allows for a maximum working temperature of ~ 700 K, enough for the evaporation of species with up to 70–80 C-atoms. Once the molecules are brought into the gas phase, they are ionized via electron impact from an electron gun (e-gun; Jordan C-950) and guided into the QIT with an ion gate. This consists of two plates at different potentials to lead the newly formed ions and a split Einzel lens to control the direction of entrance into the QIT. A DC voltage pulser (D-1040) controls the closing and opening of the ion gate, by switching the voltage in one of the half-plates of the Einzel lens that will redirect any additional ion away from the QIT. The working pressures of the source and detection chambers are $\sim 10^{-7}$ and $\sim 10^{-8}$ mbar, respectively.

1.6.1. QUADRUPOLE ION-TRAP

The QIT consists of two hyperbolic metal electrodes at each end of the trap and a ring electrode set in the middle (Stafford et al. 1984). An AC voltage is applied to the ring electrode that allows for the ions to be trapped in the center, while their position oscillates in between the two end-cap electrodes. Given that no DC offset voltage is added, the stability of molecules within the ion trap is only determined by,

$$q_z = \frac{8eV}{m(r_0^2 + 2z_0^2)\Omega^2}, \quad (1.1)$$

where r_0 and z_0 are the dimensions of the trap, V and Ω are the amplitude and frequency of the AC voltage, respectively, and e and m are the charge and mass of the ion in question (for further details, see March 1997). Only molecules for which $q_z < 0.908$



1.6. Experimental set-up

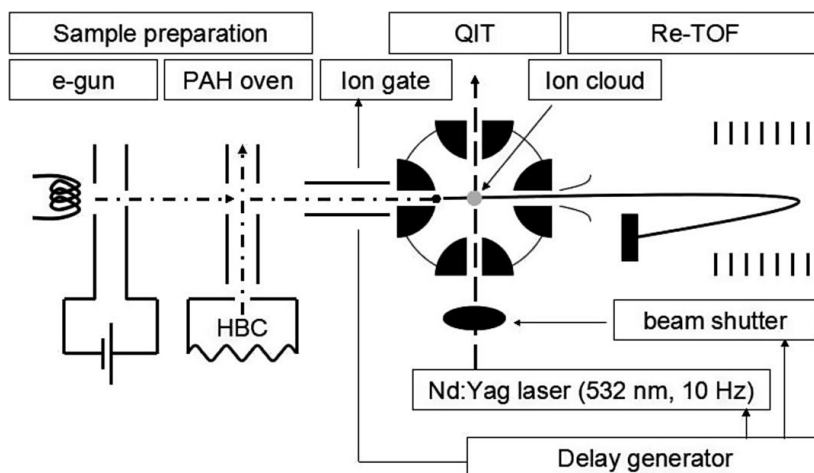


Figure 1.11.: Schematics of the instrument for photodynamics of PAHs (i-PoP). This diagram shows hexabenzocoronene (HBC) as the PAH sample. The sections of sample preparation and the QIT are part of the source chamber while the Re-TOF is part of the analysis chamber. The beam shutter and laser are situated out of vacuum. The operation cycle is controlled with a delay generator (Figure taken from Zhen et al. 2014).

fall inside the stability region of the QIT — i.e., ions below a certain mass-to-charge ratio are not trapped, with the specific cut-off given by the voltage amplitude used.

In order to remove excess kinetic energy from the PAH ions and thus increase the trapping efficiency, helium gas is leaked directly into the QIT. The pressure of this buffer gas results in an increased density of PAH ions within the QIT with respect to the background of the source chamber. By taking into account the pumping efficiency, it can be estimated that the pressure at the center of the QIT is 10^{-6} – 10^{-5} mbar (Zhen et al. 2014). Through collisions with the injected helium gas, the highly excited PAHs will quickly thermalize at about room temperature — the temperature of the gas reservoir. This in turn reduces the size of the ion cloud to ~ 1 mm (relevant for the overlap with the laser beam), concentrating the ions closely at the center of the QIT, increasing the trapping efficiency and helping as well in terms of the mass resolution.

Once the PAH ions have been trapped, they can be stored for a variable amount of time, during which mass isolation (described below) and/or irradiation can be set to occur. The irradiation can be conducted with the use of an Nd:YAG laser (DCR-3, Spectra-Physics) pumped dye laser (LiopStar-E with LSEH), or directly using only the former. In both cases doubling or tripling of the fundamental frequency can be applied and, by changing the particular dye, a wide range of wavelengths can be produced. Depending on the photon energy, the output of the laser will range from a maximum of ~ 120 mJ at 532 nm (using the second harmonic of the Nd:YAG laser) to ~ 10 mJ at 656 nm (the fundamental of the dye laser using DCM as a dye). The repetition rate of the laser system is 10 Hz, and the total number of pulses per experimental data point is controlled by an electromechanical shutter (Thorlabs SC05), located outside

I. Introduction

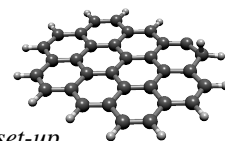
the source chamber. Finally, the fragments generated are extracted from the QIT into the TOF-MS. This is achieved by applying a pulsed voltage from ground to +800 V onto one end cap electrode and from ground to -800 V onto the other, thus emptying the QIT and leading the ions into the detection chamber through a 2 mm skimmer.

1.6.2. MASS ISOLATION

As a side effect of the electron impact ionization from the e-gun, partial fragmentation of the precursor PAH may occur. This is mostly limited to a few hydrogen losses, but it can introduce difficulties when trying to separate the effect of photodissociation and electron induced fragmentation. Furthermore, even a relatively small PAH will inevitably show significant peaks corresponding to naturally occurring isotopomers. Throughout this thesis we only deal with pure hydrogen-carbon containing PAHs, which simplifies the number of possible isotopes that need to be dealt with. While deuterium is a stable hydrogen isotope, its natural abundance is too low to pose any significant contribution to the high mass peaks observed. On the other hand, ^{13}C has a natural abundance of $\sim 1.1\%$, making its contribution significant for the analysis of medium to large sized PAHs. For instance, coronene has a first isotopic peak with an intensity $\sim 25\%$ of the pure $^{12}\text{C}_{24}\text{H}_{12}$. Even the second isotopic peak (corresponding to $^{13}\text{C}_2\text{C}_{22}\text{H}_{12}$) has an intensity of $\sim 6\%$ and the isotopic fractions only increase with the number of carbons in the molecule.

The presence of secondary peaks at the beginning of the experiment complicate the analysis. In order to ameliorate this issue, a stored waveform inverse Fourier transform (SWIFT) pulse is used to refine the mass selection (Doroshenko & Cotter 1996). It consists on a time-domain waveform, created by calculating the inverse Fourier transform of the excitation spectrum. This includes the range of resonant frequencies which corresponds to the ions to be expelled from the QIT prior to irradiation. The SWIFT pulse is fed into one of the end-cap electrodes, thus exciting the molecules whose secular frequencies inside the trap correspond to those included in the excitation spectrum.

The capacity for single peak isolation is dependent on the mass of interest and the closeness of the peaks to be eliminated. As the molecular mass increases, the secular frequencies of successive masses are found closer together, thus making it harder to properly isolate a single mass. This is indeed limited by the resolution in the frequency-domain function, which in the present case limits the single peak isolation to molecules with $N_{\text{C}} \lesssim 30$. However, broad isolation can be performed even for high mass species, which results in about three different masses to be retained in the trap (e.g., the parent molecule, the first isotopomer and the monodehydrogenated parent molecule). If these are mostly limited to isotopic peaks, as shown in Fig. 1.12, then their contribution to the mass spectrum can be dealt with separately during the analysis. Since all isotopic peaks for PAHs have masses higher than that of the pure ^{12}C molecule, the lower mass peak in the spectrum can be considered isotopically pure. By knowing as well the number of carbon atoms within the molecule and the natural abundance of ^{13}C , the contribution of isotopically substituted forms of this peak can be removed from the following ones.



1.6. Experimental set-up

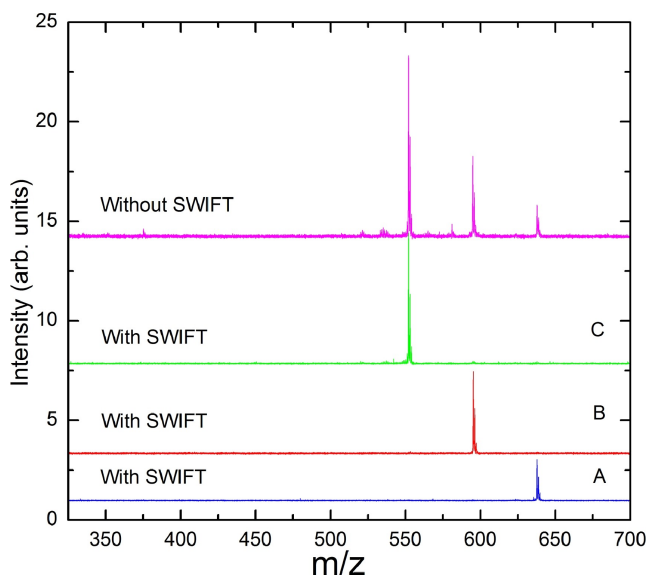


Figure 1.12.: Different SWIFT settings in the isolation of the main peaks of methyl- and methoxy-substituted hexabenzocoronene, recorded with i-PoP. Curve A corresponds to isolation of the parent molecule $(\text{CH}_3)_4(\text{OCH}_3)_2\text{C}_{42}\text{H}_{12}^+$, while curves B and C isolate the electron impact products after the loss of one and two OCH_3 units, respectively. Note that the mass spectrum without SWIFT shows only fragmentation induced by the e-gun (Figure taken from Zhen et al. 2016).

This is achieved using,

$$I'_j(I_i) = \binom{N_C}{j-i} p^{j-i} I_i, \quad (1.2)$$

where the term in brackets correspond to the binomial coefficient with j corresponding to the mass whose contribution of isotopomers from the peak with mass i is going to be removed from. I'_j is the intensity to be subtracted from peak j as a result of contributions from peak i (with $j > i$), p is the natural abundance of ^{13}C and I_i is the intensity of the isotopically pure peak i . Equation 1.2 assumes that the number of carbon atoms is the same between peak i and j , which is normally the case. After contributions from mass i are removed from higher mass peaks (up to four, depending on the size of the molecule), the process is repeated from the now isotopically pure intensity with mass $i + 1$.

1.6.3. TIME-OF-FLIGHT MASS SPECTROMETRY

Once the ion of interest has been isolated and irradiated, the fragmentation products are transported into the detection chamber for their analysis. Before entering the TOF-MS, the ions are exposed to an electric field $\Phi(r)$, where r is the position within the ion trap, and then are left to evolve in the field-free tube. As individual ions are accelerated

I. Introduction

into the TOF-MS, the initial energy can be considered to be only potential in the form $e\Phi(r)$, where e is the charge of the ion in question. Since the flight tube is field-free, the energy will be all converted into kinetic by the time it reaches the detector, leading to

$$e\Phi(r) = \frac{mv^2}{2}. \quad (1.3)$$

By taking the flight length d , we have $v = d/t$, where t is the time of flight of the particular ion. This gives us a relationship between the mass-to-charge ratio and the time of flight, namely,

$$\frac{m}{e} = \frac{2\Phi(r)t^2}{d^2}. \quad (1.4)$$

Typically the mass-to-charge ratio is given in terms of m/z in atomic units and the conversion between time and mass is given by a simple quadratic relationship.

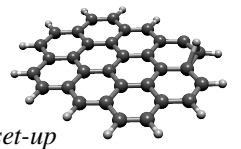
The previous treatment is strictly valid for the case of a linear TOF-MS. In i-PoP, the detection chamber consists of a reflectron mass spectrometer. While the principle of operation is the same as before, an intermediate step where the ions are reflected into the detector is added. This results in an increased mass resolution, as more energetic ions will penetrate deeper into the reflectron potential, thus allowing for less energetic ions of the same mass to “catch up” with them. In this way, the effect of variations in the initial kinetic energy can be accounted for. For more information on the functioning of a reflectron, and TOF-MS in general, see Mamyryn (2001).

The detector itself is made of a multi-channel plate (MCP; Jordan C-701), which functions as an amplifier for ion signal. Under normal circumstances, the effect of a single particle is undetectable, but the high electric field of the MCP allows for individual particles hitting the channels to produce an electron cascade. The total signal gain has been estimated to be 2×10^8 (Zhen et al. 2014).

The recorded spectrum can then be analyzed in terms of the intensity of the detected peaks. Individual peaks have been fitted to a model function rather than integrated numerically, given that the former method allows for estimating the error in individual measurements. While fitting a Gaussian function to each mass peak provides a good zero-th order approximation, it does not take into account the asymmetry and non-standard kurtosis (“spikiness”) of the actual data. To obtain a more proper fit and reduce the residuals, a Pearson IV distribution has been used for all the experimental data analysis (Pearson 1895). This function can be expressed as,

$$f(x) = Ak \left(1 + \left(\frac{x - \lambda}{\alpha} \right)^2 \right)^{-m} \exp \left(-\nu \arctan \left(\frac{x - \lambda}{\alpha} \right) \right), \quad (1.5)$$

where the parameter A is related to the peak intensity and parameters λ , α , ν and m relate to the mean ($\mu \doteq \langle x \rangle$) and the moments ($\mu_i \doteq \langle (x - \mu)^i \rangle$, with i referring to the i th moment) of the distribution. In terms of the variance ($\sigma \doteq \sqrt{\mu_2}$), skewness



1.6. Experimental set-up

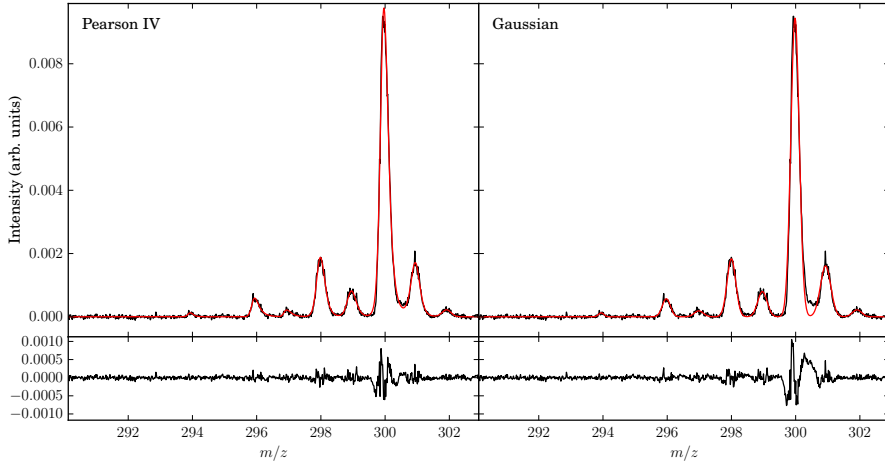


Figure 1.13.: Comparison of Pearson IV (left) and Gaussian (right) fits to a mass spectrum of the coronene cation ($C_{24}H_{12}^+$). The fragmentation corresponds to electron impact effects and the lower panels show the residual to the corresponding fit. Low intensity peaks are generally fit equally well, but a significant improvement can be observed for the fit of high intensity peaks, for which the wings are better accounted for.

($\gamma_1 \doteq \mu_3/\sigma^3$) and kurtosis ($\gamma_2 \doteq \mu_4/\sigma^4$), the relationships are given by,

$$\mu = \lambda - \frac{\alpha v}{r}, \quad (1.6)$$

$$\sigma = \sqrt{\frac{\alpha^2}{r^2(r-1)}} \sqrt{(r^2 + v^2)}, \quad (1.7)$$

$$\gamma_1 = \frac{-4v}{r-2} \sqrt{\frac{r-1}{r^2 + v^2}}, \quad (1.8)$$

$$\gamma_2 = \frac{3(r-1) [(r+6)(r^2 + v^2) - 8r^2]}{(r-2)(r-3)(r^2 + v^2)}, \quad (1.9)$$

where $r = 2(m-1)$. In order for σ to be well defined, a constrain in the form $m > 1.5$ is placed on the fit. The parameter k in eqn. 1.5 is the normalization factor of the Pearson IV distribution, given by,

$$k = \frac{\left| \frac{\Gamma(m+iv/2)}{\Gamma(m)} \right|}{\alpha B(m-0.5, 0.5)}, \quad (1.10)$$

with Γ and B being the Gamma and Beta functions, which are defined as follows,

$$\Gamma(z) = \int_0^{\infty} x^{z-1} e^{-x} dx, \quad (1.11)$$

$$B(x, y) = \frac{\Gamma(x)\Gamma(y)}{\Gamma(x+y)}. \quad (1.12)$$

1. Introduction

Given that the integral for $\Gamma(z)$ only converges if the real part of z is positive, it is required that $m > 0.5$, but this is less restrictive than the constrain on m set for the width to be well defined. A sample fit and comparison to an equivalent Gaussian fit is shown in Fig. 1.13.

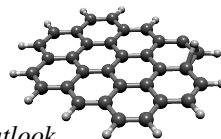
1.7. THESIS CONTENTS

One key question in astronomy is to understand the organic inventory of space, particularly in regions of star and planet formation. Observations reveal that PAHs are an important component of the ISM and are key to the molecular universe. In particular, they may contribute to the formation of fullerenes as well as H_2 formation. This thesis focuses on the most stable products of PAH top-down chemistry and their relevance for astronomy in particular.

Chapter II is an exploration on the abundance and formation of C_{60} in PDRs. It includes a small scale survey searching for evidence on the universality of the anticorrelation between the intensity of the C_{60} and PAH bands. This is focused on a series of well studied PDRs encompassing a wide range of G_0 and density. The analysis is not limited to the mid-IR band intensity, but also compares the physical conditions of the PDRs to the PAH dehydrogenation model of Montillaud et al. (2013). This allowed to establish that, in the PDRs studied, both the level of PAH fragmentation and the observed band strengths are consistent with C_{60} formation through the fragmentation of PAHs.

In chapter III laboratory evidence is presented for the formation of fullerenes via photodissociation of large PAHs. The dissociation pattern of both fullerenes and PAHs shows the same enhanced peaks of pure carbon clusters, coinciding with the so called “magic numbers” of the fullerene family, which represent particularly stable structures. The decrease in C_{60} cross-section at 532 nm provides additional support for this formation pathway, as large PAHs irradiated at this wavelength only show little dissociation after the peak corresponding to C_{60} has been formed. Additional experiments are included, which suggest that the same conclusions could be drawn for the formation of C_{70} , thus connecting PAHs with the whole fullerene family and not exclusively C_{60} .

Chapter IV is an extensive experimental and theoretical study on the dehydrogenation of nine medium and large sized PAHs. The competition between sequential hydrogen loss and the formation of H_2 is explored in detail. Results from DFT calculations are put together into a detailed Monte-Carlo model that accounts for the effects of hydrogen roaming along the edge of the molecule, using experiments to guide the Monte-Carlo model. In concordance with other works, small PAHs are found to dehydrogenate sequentially, with exceptions for those that have a high proportion of trio hydrogens and bay regions. However, large PAHs show evidence for molecular hydrogen formation dominating the dehydrogenation process, at the very least in the first few steps. A divergence between DFT calculations with isomerization involving solo hydrogens and the experimental results is found, although the exact origin of this remains unclear. Most importantly, this work points toward H_2 formation from PAHs as a possibly efficient formation mechanism in PDRs.



1.8. Outlook

Finally, in chapter V, the previous results are applied to physical conditions typical of dense PDRs. As mentioned in Sect. 1.3.1, there is a known mismatch between the observed rate coefficient of H_2 production and the rates of established formation mechanisms. Here, molecular hydrogen formation as an outcome of PAH dissociation is investigated as a possible pathway to bridge this gap. Under ideal conditions, H_2 formation is found to be nearly two orders of magnitude larger than previously established, although it cannot account for the full mismatch. This work also reaffirms that H_2 formation through PAHs photodissociation dominates over abstraction from super-hydrogenated PAHs. The latter process would only be effective deep inside molecular clouds and not at PDR photodissociation fronts.

1.8. OUTLOOK

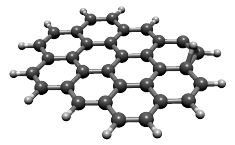
Within a few years, the launch of *JWST* promises to revolutionize the study of the AIBs. On the one hand, the increased sensitivity with respect to previous IR telescopes could allow for the detection of weak bands associated with PAHs, revealing more details of their general structure and hydrogenation state. While it is highly unlikely that a specific identification will take place, questions associated with heteroatom substitutions, the presence of aliphatic side groups and other “decorated” forms seems to be within reach. On the other hand, the increased angular resolution ($\sim 0''.2$) in spectral mapping will show the evolution of the mid-IR bands as the environmental physical conditions change, both in terms of the density and the UV field strength. For the first time, band shape and intensity shifts within single sources will be able to include the full range of the AIBs. Not only this, but the ability to map intensity variations at such resolutions will allow for comparisons with ALMA observations in order to search for small molecules thought to be by-products of PAH photodissociation and find correlations with AIB emission.

This thesis, together with other recent studies (e.g., Alvaro Galu e 2014; Bouwman et al. 2016; Trinquier et al. 2017a,b), point to the importance of isomerization reactions for interstellar PAHs. Not only does this affect the photodissociation process, as demonstrated in this work, but also their IR signatures. Isomerized and partially fragmented PAHs are generally unavailable commercially, making it hard for their mid-IR spectra to be measured experimentally. Furthermore, the sheer number of possible isomers each PAH can have at varying degrees of fragmentation, would make even a purely theoretical treatment a titanic undertaking. However, the combination of QIT/TOF-MS techniques with infrared multiphoton dissociation (IRMPD; e.g., Oomens et al. 2001, 2006) spectroscopy can help in elucidating these questions. While IRMPD has drawbacks, particularly relating to relative band intensities, it can guide DFT calculations in identifying the structure of fragmentation products. The QIT/TOF-MS, coupled with isolation techniques such as SWIFT, allow for the selection of individual products, which can be probed using IRMPD.

The enhanced capacity of *JWST* with respect to its predecessors, poses a challenge to experimental and theoretical astrochemistry. Even considering the current understanding of the AIBs, a plethora of issues remain open on the molecular characteris-

I. Introduction

tics of the emitters (the extent of nitrogen substitution, the degree of processing, etc.) and even on their emission process, particularly on the topic of anharmonic effects. The availability of *JWST* could certainly hold the key to answering these questions, it could also magnify the known problems with the PAH hypothesis. While the latter option seems problematic, it is also exciting, as it would open up the research scope on astronomically relevant, polyaromatic molecules. Continued experimental and theoretical studies, not only on classic PAHs, but on more exotic forms, still based on their basic structure, are absolutely critical in understanding the characteristics of these complex organic molecules. Both approaches have their own inherent strengths and pitfalls, but in tandem — and guided by astronomical observations —, they can lead to accurate models of the interstellar PAH population, their evolution and the products of their photodissociation that could lead to further chemical complexity by merging top-down and bottom-up chemistry.



II

FULLERENES IN PHOTODISSOCIATION REGIONS

Recent studies have confirmed the presence of buckminsterfullerene (C_{60}) in different interstellar and circumstellar environments. However, several aspects regarding C_{60} in space are not well understood yet, such as the formation and excitation processes, and the connection between C_{60} and other carbonaceous compounds in the interstellar medium (ISM), in particular polycyclic aromatic hydrocarbons (PAHs). In this paper we study several photodissociation regions (PDRs) where C_{60} and PAHs are detected and the local physical conditions are reasonably well constrained, to provide observational insights into these questions. C_{60} is found to emit in PDRs where the dust is cool ($T_d = 20\text{--}40$ K) and even in PDRs with cool stars. These results exclude the possibility for C_{60} to be locked in grains at thermal equilibrium in these environments. We observe that PAH and C_{60} emission are spatially uncorrelated and that C_{60} is present in PDRs where the physical conditions (in terms of radiation field and hydrogen density) allow for full dehydrogenation of PAHs, with the exception of Ced 201. We also find trends indicative of an increase in C_{60} abundance within individual PDRs, but these trends are not universal. This results support models where the dehydrogenation of carbonaceous species is the first step towards C_{60} formation. However, this is not the only parameter involved and C_{60} formation is likely affected by shocks and PDR age.

2.1. INTRODUCTION

Buckminsterfullerene or C_{60} was first discovered in laboratory experiments aimed to understand the spectroscopy of carbon chain molecules in the interstellar medium (ISM) and circumstellar envelopes (Kroto et al. 1985). Based on their study, the discoverers of C_{60} concluded that the molecule corresponded to a new form of carbon organized as a truncated icosahedron, usually compared with the old style black and white “soccer” ball.

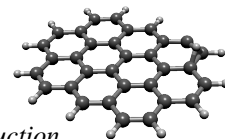
C_{60} is a super-stable molecule and is considered the prototypical fullerene, cage-like molecules of pure carbon. Krätschmer et al. (1990) developed a method to produce bulk quantities of C_{60} by evaporating graphite electrodes in a helium atmosphere. They also confirmed the structure of the molecule through X-ray diffraction and its infrared (IR) spectrum. The discovery of fullerenes has also opened up the research of carbon nanotubes, another different form of carbon which combines the properties of graphite and fullerenes (Iijima 1991).

The values for the IR active modes of C_{60} are 526, 575, 1182 and 1429 cm^{-1} , which correspond to 18.9, 17.4, 8.5 and 7.0 μm (Menéndez & Page 2000). Several theoretical and experimental studies have been carried out on the IR bands of (Chase et al. 1992; Fabian 1996; Choi et al. 2000; Iglesias-Groth et al. 2011) but, while the values for the frequencies show a good agreement, reported intrinsic band strengths vary widely.

From its very discovery, C_{60} was considered a potential component of interstellar dust and was speculated to be the carrier of some of the diffuse interstellar bands (DIBs). Its survival in ISM conditions is supported by its high stability. However, until recently, unequivocal detection has not been possible. A first tentative detection was the association of two, weak, far-red absorption bands with C_{60}^+ (Foing & Ehrenfreund 1994). This identification has been contested and the issues were never fully resolved (Maier 1994). The main obstacle for the detection of fullerenes in emission stems from the fact that the mid-IR spectra of almost all interstellar sources are dominated by the vibrational spectrum of polycyclic aromatic hydrocarbons (PAHs). Because of this, in sources with strong PAH emission, small amounts of fullerenes are difficult to detect, with their emission hidden by the PAH bands and the continuum.

Cami et al. (2010) recognized C_{60} and C_{70} bands in the spectrum of the planetary nebula (PN) Tc 1, which has no strong PAH bands. After the detection of these transitions and their association with C_{60} several more objects have been investigated, showing that C_{60} exists in a variety of sources in different stages of stellar evolutions and with varying physical conditions. Most of these observations have dealt with PNe, including galactic and extragalactic sources in the Magellanic Clouds (García-Hernández et al. 2011; Otsuka et al. 2012), proto-PN (Zhang & Kwok 2011) and in circumstellar envelopes of binary post-AGB stars (Gielen et al. 2011). There has also been a detection towards a young stellar object (YSO) and a Herbig Ae/Be (Roberts et al. 2012), which represent isolated prestellar objects. C_{60} was also detected in photodissociation regions (PDRs), associated with both reflection nebula (RN) (Sellgren et al. 2010) and HII regions (Rubin et al. 2011).

The excitation mechanism of C_{60} is not yet clear. This is an important question to address since it determines which physical conditions of its environment are traced by



2.1. Introduction

the bands. Two different mechanisms have been suggested: Cami et al. (2010) consider the band ratios from Tc 1 to be consistent with a thermal distribution of the excited states, and thus derive an excitation temperature of ~ 330 K. This mechanism requires C_{60} not to be in the gas phase, but in solid state or deposited on the surface of dust grains.

Another excitation mechanism, proposed by Sellgren et al. (2010), assumes that C_{60} remains in the gas phase and the bands originate from IR fluorescence. This is widely accepted as the excitation mechanism for PAHs and consists in the absorption of a single UV photon, which leaves the molecule highly excited and leads to a redistribution of the energy between the vibrational modes. While the reported $7.0/18.9 \mu\text{m}$ ratio found in NGC 7023 is in good agreement with fluorescence models, a much lower value was reported in the reflection nebula NGC 2023 (Sellgren et al. 2010). We note though that this ratio is very difficult to determine in spectra dominated by the PAH features as the underlying plateau emission is both intense and broad. This holds for NGC 7023 and NGC 2023 and the problem is compounded when the program `pahfit` is used to extract the intensity for highly blended and weak features, as the adopted intrinsic Lorentzian profile (which is inappropriate for fluorescence from highly excited species, cf. Tielens 2008) locates much of the emission in ill-fitted wings. Moreover, the analysis of observed C_{60} band ratios to discriminate between the thermal and fluorescence emission mechanism in space are hampered by the unknown intrinsic strength of these modes. Recently, Berné et al. (2013) reported a detection of C_{60}^+ in NGC 7023 through four bands at 6.4 , 7.1 , 8.2 and $10.5 \mu\text{m}$. This would support the idea that C_{60} is in the gas-phase, at least in environmental conditions similar to those found in NGC 7023.

The formation of C_{60} is also the subject of debate. It seems self-evident to consider that C_{60} could be build-up from small (hydro)carbon chains in the C-rich ejecta of Tc 1 and other PNe whose spectra are dominated by C_{60} . In H-poor environments (not the case of these PNe), simple formation paths analogous to the chemical routes described by Kroto et al. (1985) might lead to C_{60} formation (Cherchneff et al. 2000). However, neither mechanism is efficient enough to account for the widespread detection of C_{60} in the ISM.

Another hypothetical formation route in PNe is through photochemical processing of hydrogenated amorphous carbon (HAC; Bernard-Salas et al. 2012; Micelotta et al. 2012). The details of this mechanism require the presence of large HAC clusters ($N_C > 100$), with a high atomic hydrogen fraction (i.e. not exposed to strong or continued UV radiation). The sudden exposure of these small compounds to UV photons is speculated to lead to dehydrogenation and aromatization. This would result in giant fullerene cages which will shrink to C_{60} and C_{70} through C_2 -loss.

Finally, Berné & Tielens (2012) recognized that the abundance of C_{60} increases rapidly when approaching the illuminating star of the reflection nebula NGC 7023, while the abundance of PAHs decreases. They propose that UV processing of PAHs leads to fullerene formation. Under the influence of radiation, PAHs will first become dehydrogenated, leading to the formation of graphene-like sheets. A continued exposure to high energy photons is expected to remove carbon from within the structure, which would force the formation of pentagonal rings and the bending of the sheet. This process of destruction leads to multiple different intermediate species. Because of its

II. Fullerenes in photodissociation regions

high stability, C_{60} is expected to be the photoproduct with the longest lifetime, and therefore it can be present at $\sim 0.01\%$ of the elemental C near the star.

In this study, our goal is to contribute to the understanding of the origin and evolution of C_{60} in environments where high PAH abundance is also found. We test the formation mechanism proposed by Berné & Tielens (2012) by comparing the variations of the fractional abundance of C_{60} and PAHs as a function of physical conditions, in terms of the UV field (G_0) and the hydrogen density ($n(H)$). We also consider spatial variations of these abundances within the sources, in particular with respect to the position of strong sources of radiation. We used data from IRS (Houck et al. 2004) on-board of the *Spitzer Space Telescope* (Werner et al. 2004) and the PACS instrument (Poglitsch et al. 2010) on the *Herschel Space Observatory* (Pilbratt et al. 2010), for three PDRs: NGC 2023 North, Ced 201 and RCW 49. We complement this analysis by including previous observations of the Horsehead nebula, IC 63 and Orion’s Veil. For these latter sources we do not perform such a detailed analysis since the C_{60} bands are not detected, except in Orion’s Veil, which was studied by Boersma et al. (2012).

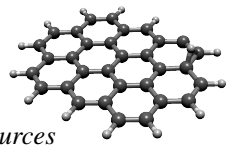
This chapter is organized as follows: in Sect. 2.2 we give a description of the physical and chemical conditions of the sources, taken from the literature. Sect. 2.3 describes the data from IRS and PACS that were used and explain the data reduction process. In Sect. 2.4, the reduced spectra and feature maps obtained from IRS are presented, together with the derivation of the UV field intensity from the PACS for each source. We also describe the observed variations of C_{60} and PAH abundances within each source. In Sect. 2.5 we discuss our results and compare them with the C_{60} formation model of (Berné & Tielens 2012). Finally, Sect. 2.6 summarizes the main results and conclusions of this work.

2.2. SOURCES

2.2.1. NGC 2023

NGC 2023 is at a distance of 330–385 pc and is illuminated by HD 37903. This star is usually classified as a B1.5 V star (Brown et al. 1994), although more recent studies have concluded that it is a Herbig Ae/Be star of spectral class B2 Ve (Mookerjee et al. 2009), based on its UV spectra and IR excess. This RN is part of the dark cloud L 1630 in Orion, which also hosts the famous Horsehead nebula (B 33). Surrounding HD 37903 there is a small HII region, with a size of 0.015 pc (Knapp et al. 1975; Pankonin & Walmsley 1976). A far-IR study by Harvey et al. (1980), showed that the molecular cloud L 1630 lies behind HD 37903. The age of the stars within NGC 2023 has been calculated to be 1–7 Myr, with the most massive stars falling towards the lower end of the range (López-García et al. 2013).

Figure 2.1 gives a general overview of NGC 2023. The shape of the reflection nebula is roughly circular, with HD 37903 located to the South-East of the center. The radiation from HD 37903 is the main source of UV photons and creates a bubble-shaped cavity, particularly clear in the IRAC 8 μm image (Fig. 2.1), which traces mostly PAH emission. Outside the cavity, PAH emission become faint, as expected due to UV ex-



2.2. Sources

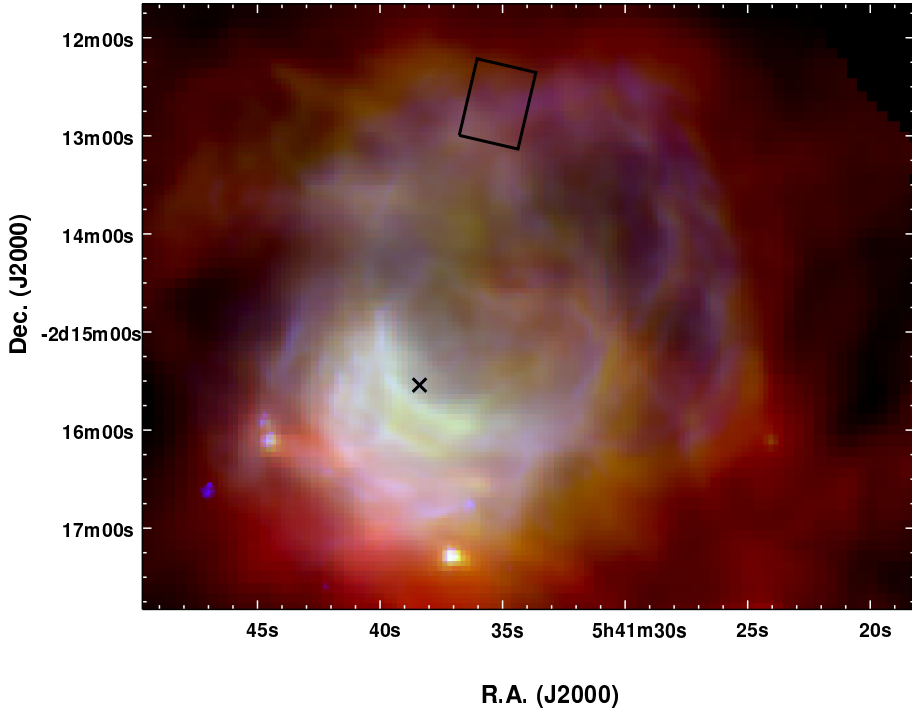


Figure 2.1: Composite image of NGC 2023. In blue is the IRAC 8 μm image, showing the distribution of PAHs. In green is the PACS 70 μm map, which traces warm dust grains. In red is PACS 160 μm , tracing colder dust. The cross indicates the position of HD 37903 and the black box shows the IRS field that we will use for this work.

tion. Surrounding the cavity, several filaments or ridges are observed, most clearly in PAH and warm dust emission. In particular, close to HD 37903, the southern ridge is the most luminous part of the nebula, hosting a high concentration of YSOs (Lada et al. 1991; Mookerjea et al. 2009). Other, less luminous ridges can be seen to the North and the West of HD 37903. The black box in Fig. 2.1 shows the IRS field that will be the focus of our analysis, which lies on top of the northern ridge of NGC 2023.

From observations of far-IR fine structure lines of [CII], [OI] and [SII], Steiman-Cameron et al. (1997) established that the environment in NGC 2023 is clumpy. Their observation of the northern PDR is not spatially coincident with the position of the IRS field, but corresponds to a position closer to the HD 37903. For this location they find conditions consistent with $G_0 = 2 \times 10^4$ and $n_0 = 3 \times 10^3 \text{ cm}^{-3}$. Pilleri et al. (2012) model the same IRS field we use in this study. They derive n_0 as a function of the distance to HD 37903 fitting a power law for the density profile, from the density in the diffuse region (a free parameter in their fit) up to a maximum density, which they take from Fuente et al. (1995), based on CN observations. The density ranges from $2.4 \times 10^3 \text{ cm}^{-3}$ to $2 \times 10^4 \text{ cm}^{-3}$ throughout the field.

II. Fullerenes in photodissociation regions

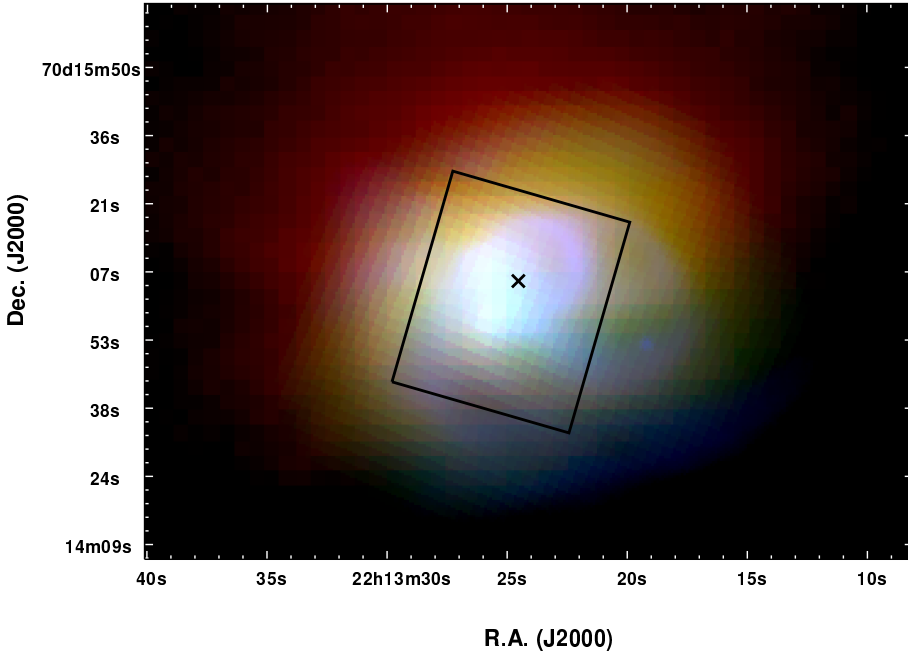
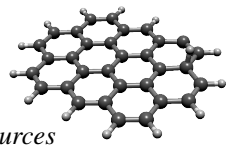


Figure 2.2.: Composite image of Ced 201. Blue corresponds to the IRAC 8 μm image, green to MIPS 24 μm and red to PACS 70 μm . The box is the IRS field that will be used in this work. The cross marks the position of the illuminating star BD +69 1231.

Sellgren et al. (2010) reported the detection of three features of C_{60} at 7.0, 17.4 and 18.9 μm in NGC 2023. A recent work by Peeters et al. (2012) also detected extended C_{60} emission — based on the 18.9 μm band — in two areas within NGC 2023, using the IRS instrument on-board of *Spitzer*. In the southern field they observed that spatial variations of C_{60} and PAHs are consistent with the findings of Berné & Tielens (2012) in NGC 7023 — i.e., C_{60} bands peak closer to the position of HD 37903 than the PAH features. However, in their northern position they find the opposite, with C_{60} peaking further away from the illuminating star than the PAHs, which they suggest may be due to geometrical effects.

2.2.2. CED 201

Ced 201 is an unusual RN, since it is the result of a chance encounter between a molecular cloud and a runaway B9.5 V star (BD +69 1231), while in most RNe the illuminating star is formed within the cloud. This was realized due to a difference of $\sim 12 \text{ km s}^{-1}$ in the radial velocity of the star and the molecular cloud (Witt et al. 1987). Due to its relative velocity with respect to the molecular cloud, the star in Ced 201 affects the gas and dust not only through its radiation field, but also induces shocks and turbulence. An arc-like structure can be observed to the East of the star, clear at all



2.2. Sources

wavelengths shown in Fig. 2.2. This structure has been interpreted as a shock due to the star penetrating into the molecular cloud. However, no signature of a shock has been observed in the line profiles of CO (2–1) (Cesarsky et al. 2000). The cloud itself is part of the Bok Globule B 175 (L 1219), which lies at a distance of ~ 400 pc (Casey 1991). Given that the PDR is the product of a chance encounter, its age can be estimated using the velocity of the star with respect to the cloud. We have used the proper motion of the star (as measured by Høg et al. 2000) and calculated the angular distance from the star to the edge of the cloud in the direction of the proper motion. This gives a rough estimate of ~ 1500 yr.

Figure 2.2 shows the region of Ced 201. The star is entering the molecular cloud from West, generating the aforementioned arc-like structure. The cold dust (in red) — and with it the molecular cloud itself — is mostly located towards the North. Hotter dust grains, as traced by MIPS $24 \mu\text{m}$, are found closer to BD +69 1231. PAH emission (in blue) is located much nearer to the illuminating star and to the South — the edge of the molecular cloud. PAHs and hot dust coexist in the proximity of BD +69 1231.

Young Owl et al. (2002) used far-IR fine structure line intensities of [CII] and [OI] (for the latter only upper limits were derived) and determined the physical conditions of the gas to be $n_0 = 4 \times 10^2 \text{ cm}^{-3}$ and $T_{\text{gas}} = 200$ K, while for the radiation field they find $G_0 \simeq 300$. However, a previous study by Kemper et al. (1999) found higher values for both parameters, with $n_0 = 1.2 \times 10^4 \text{ cm}^{-3}$ and $T_{\text{gas}} \simeq 330$ K. They also find $n(\text{H}_2) = (5 \pm 1) \times 10^3 \text{ cm}^{-3}$. The latter values were derived from a PDR model which fits observed fine structure atomic lines (using again [CII] and upper limits of [OI]) and molecular sub-mm lines. They detected CO, ^{13}CO and HCO^+ and in addition put upper limits for CS and C^{18}O . The discrepancy in the values derived for the density stems from the fact that Kemper et al. (1999) based their model not only on the fine-structure lines but also on molecular data. We expect their values to provide a better constraint on the density values. This is also supported by Casey (1991), who finds $n > 2000 \text{ cm}^{-3}$ based on dust emission from the far-IR.

2.2.3. RCW 49

RCW 49 is one of the most luminous and massive HII regions in the galaxy. The region is powered by the compact cluster Westerlund 2 (Westerlund 1961) where several OB stars have been detected, including at least twelve O-stars earlier than O7, with the earliest being of type O3 V((f)) (Rauw et al. 2007). It also hosts two Wolf-Rayet stars, WR20a and WR20b. WR20a was found to be a binary system of two WN6ha stars with individual masses of $\sim 70 M_{\odot}$ (Rauw et al. 2004). WR20b appears to be a single star, also with spectral type WN6ha. The presence of Wolf-Rayet stars imply a cluster age of 2–3 Myr (Piatti et al. 1998). The molecular density and kinetic temperature have been determined through CO, and ^{13}CO observations by Ohama et al. (2010), with the temperature ranging from 30 to 150 K and a typical density of $n_{\text{H}_2} \simeq 3000 \text{ cm}^{-3}$.

Figure 2.3 shows the environment of RCW 49. PAHs and dust are seen all over the nebula, with the brightest ridges near the Wolf-Rayet stars. The overall shape is somewhat elongated in the North-South direction, resembling a kidney. Two prominent bubbles are observed in radio continuum images, one surrounding Westerlund 2

II. Fullerenes in photodissociation regions

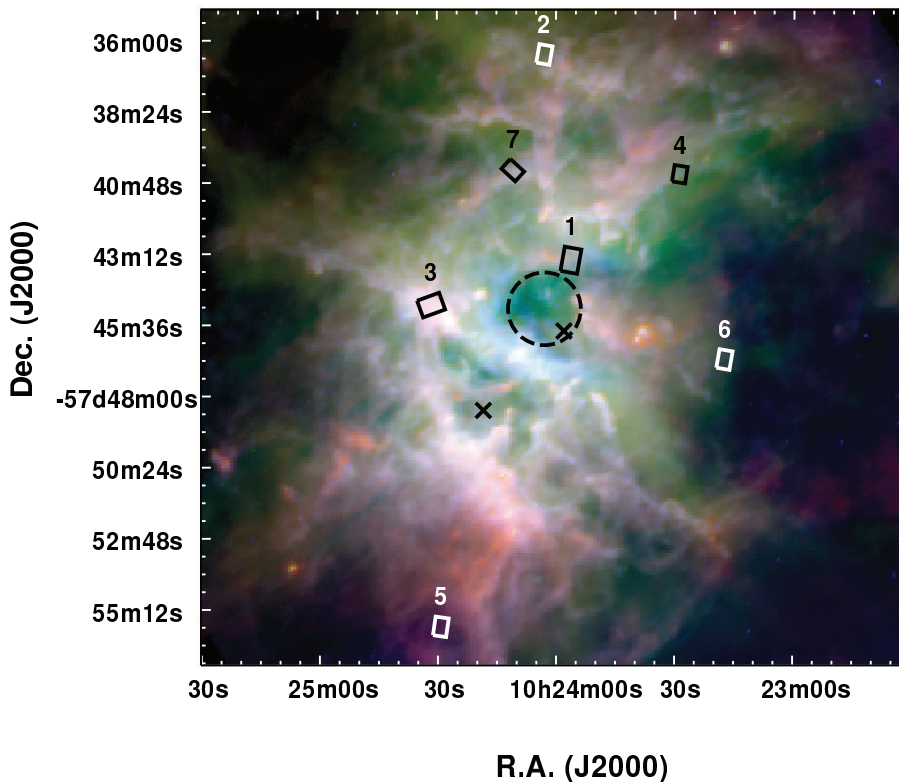
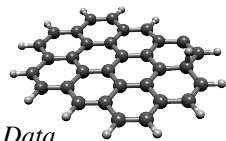


Figure 2.3.: Composite image of RCW 49. Blue corresponds to the IRAC 8 μm image, while green and red correspond the PACS images at 70 μm and 160 μm respectively. The boxes show the seven IRS fields which are used in this work. The numbers on top of each box correspond to the nomenclature used from hereon to refer to the individual regions. The crosses indicate the position of both Wolf-Rayet stars, with WR20a to the North and WR20b to the South. Finally, the dashed circle indicates the position of the cluster Westerlund 2, which hosts most of the OB stars in the region.

and the other around WR20b. The bubble around Westerlund 2 is open to the West (Whiteoak & Uchida 1997). In this region, dust and PAHs coexist with the ionized gas or are at least embedded in neutral gas mixed with the ionized region (Churchwell et al. 2004). PAH emission, traced by IRAC 8 μm (blue in Fig. 2.3), is more intense in the surroundings of Westerlund 2. The ridges, bubbles and pillars that can be seen in Fig. 2.3 are evidence of the strong interaction of the parent molecular cloud with the stellar radiation and winds from Westerlund 2 and recently formed stars. The seven IRS fields considered in this work cover regions with very different conditions, allowing us to probe a large range of UV field intensities. In the following, when we refer to individual positions we will use the numbers shown above the respective box in Fig. 2.3.



2.3. Data

The distance to RCW 49 has been the subject of debate, with derived values ranging from 2.3 to 7.9 kpc (Brand & Blitz 1993; Whiteoak & Uchida 1997; Moffat et al. 1991), where the lower limit comes from radio continuum observations and kinematic studies and the upper limit is derived from the luminosity distance. A recent photometric analysis by Carraro et al. (2013) derives the reddening and extinction curves towards several members of Westerlund 2. With this, they correct the apparent distance modulus in order to obtain the distance to the cluster, $d = 2.85 \pm 0.43$ kpc.

2.2.4. ADDITIONAL SOURCES

In this study we also consider results involving Orion’s Veil, NGC 7023, IC 63 and the Horsehead nebula. The first two sources have been previously studied and show the presence of C_{60} bands (Boersma et al. 2012; Berné & Tielens 2012). In the case of Orion’s Veil eleven positions were observed (Boersma et al. 2014), which are labeled with increasing distance to Orion’s Bar as I4–I1, M1–M4 and V1–V3, respectively. From these, we do not include in our analysis the two regions closest to the Bar (I4 and I3) given that their counterparts in PACS observations suffer strong contamination with emission from the Bar. We also discard the farthest region (V3), as it looks edge-on to the back of the PDR, and thus does not probe the same environment as the remaining regions (Boersma et al. 2012). The Horsehead nebula and IC 63 do not show C_{60} emission bands. In the case of the Horsehead, we have used data corresponding to the “mane”, where no excess emission over the continuum is detected at $\sim 19 \mu\text{m}$ (the strongest C_{60} feature). We consider as upper limits the highest value that could be fitted using `pahfit`, although it was always fitted as a detection below 3σ . For IC 63, there are areas where there is emission over the continuum that cannot be fitted by the [SIII] line alone (which partly overlaps with the $18.9 \mu\text{m}$ band of C_{60}). These pixels are fitted by `pahfit` with confidence over 3σ but, upon visual inspection, we find that the fit is of poor quality and we consider the C_{60} band intensity to be an upper limit. Physical conditions for these additional sources will be discussed in Sects. 2.4.3 and 2.4.4.

2.3. DATA

2.3.1. IRS DATA

We used data from the Infrared Spectrograph (IRS; Houck et al. 2004) on-board of the *Spitzer Space Telescope* (Werner et al. 2004). The spectrograph consists of four modules, divided according to the wavelength coverage and resolution: short wavelengths with low resolution (SL), long wavelengths with low resolution (LL), short wavelengths with high resolution (SH) and long wavelengths with high resolution (LH).

For the low resolution modules the wavelength coverage goes from $5.2 \mu\text{m}$ to $38.0 \mu\text{m}$ for the combination of SL and LL and have a spectral resolution ($R = \lambda/\Delta\lambda$) between 60 and 130. In the case of the high resolution modules, the combined coverage of SH and LH ranges from $9.9 \mu\text{m}$ up to $37.2 \mu\text{m}$, with a spectral resolution $R \simeq 600$.

II. Fullerenes in photodissociation regions

We gathered the spectral cubes from the Spitzer Heritage Archive¹. For NGC 2023 and Ced 201 we used observations from the program with PID 3512 (PI C. Joblin). In the case of NGC 2023, we considered observations performed with SL and LL modules with AOR keys 12014848 and 12011264, respectively. For Ced 201 we selected again SL and LL modules, in this case with AOR keys 11047936 and 11047680 respectively.

For RCW 49 we have 7 fields, all of them in SH module, from the program with PID 20012 (PI M. Wolfire). Their respective AOR keys are 13812992, 13813248, 13813504, 13813760, 13814016, 13814272 and 13814528. These regions are not contiguous and will be referred to according to the numbers shown in Fig. 2.3.

The data reduction and cube generation was performed using the `cubism` software (Smith et al. 2007a). The recommended data reduction begins by taking a background when available. None of the observations has a dedicated background observation. The low resolution modes have “outrigger” slits, that fall outside the area of interest. In the case of Ced 201 this slit falls on an empty patch of sky so we used this to do the background subtraction. In the observations of NGC 2023 the slit falls in regions with important emission from the same source, leading us not to consider it a background for this source. For of NGC 2023 and RCW 49 the lack of background is not detrimental, given that both sources are bright.

2.3.2. PACS DATA

In order to have a measure of the far-IR (FIR) intensities we used photometric data from the Photodetector Array Camera and Spectrometer (PACS; Poglitsch et al. 2010) on-board of the ESA *Herschel Space Observatory* (Pilbratt et al. 2010). In all three sources we retrieved the available data at 70 and 160 μm from the Herschel Science Archive². The observations of NGC 2023, Ced 201 and RCW 49 have respective OB-SIDs of 1342227049/50, 1342196809/10 and 1342255009/10.

2.4. ANALYSIS

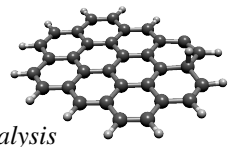
2.4.1. SPECTRAL FIT

In order to fit the different features of the IRS spectra we used the tool `pahfit` (Smith et al. 2007b). This tool fits a stellar continuum and multiple modified black-body emission curves with different temperatures. These emission curves are used to fit the mid-IR continuum, but their temperatures do not accurately represent the temperature of the dust, since grains emitting at these wavelengths are not in equilibrium with the radiation field, but are rather transiently heated to high temperatures (Draine 2003). It also considers several unresolved atomic lines as well as H_2 rotational lines. Finally it fits different PAH features and the 18.9 μm feature of C_{60} .

In Fig. 2.4 we present an example of a low resolution spectrum from NGC 2023 from the area where the 18.9 μm feature peaks. The fit matches reasonably well the

¹<http://sha.ipac.caltech.edu>

²http://herschel.esac.esa.int/Science_Archive.shtml



2.4. Analysis

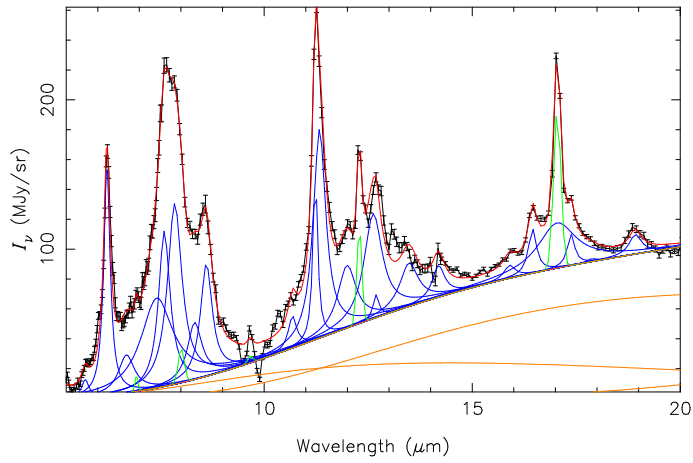


Figure 2.4.: Examples of a fitted low resolution spectrum of NGC 2023. The black line with error bars is the observed spectrum while the red line is the total fitted spectrum. The individual components are shown in blue (PAH and C_{60} features), green (unresolved H_2 lines) and orange (modified black body continua).

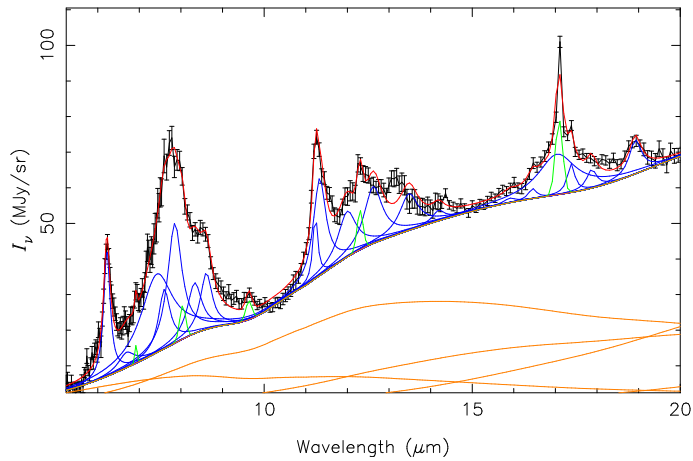


Figure 2.5.: Example of a fitted low resolution spectrum from Ced 201. The black line with error bars is the observed spectrum while the red line is the total fitted spectrum. The individual components are shown in blue (PAH and C_{60} features), green (unresolved H_2 lines) and orange (modified black body continua).

II. Fullerenes in photodissociation regions

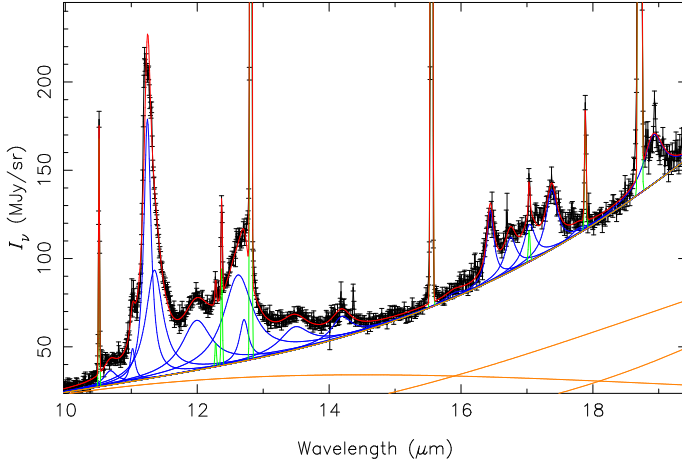


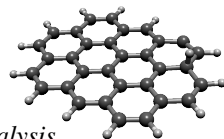
Figure 2.6.: Example of fitted a high resolution spectrum from RCW 49, Region 2. The black line with error bars is the observed spectrum while the red line is the total fitted spectrum. The individual components are shown in blue (PAH and C_{60} features), green (unresolved H_2 and atomic lines) and orange (modified black body continua).

observed spectrum with the exception of the PAH bands between 13 and 14 μm , for which the peak positions seem to be somewhat different from the values considered by `pahfit`. However, these bands are rather weak and when considering the integrated PAH band intensities their contribution will be small. The same is observed in the sample spectrum of Ced 201 (Fig. 2.5). In both sources the 18.9 μm feature associated with C_{60} is clearly present. The only unresolved lines fitted in these spectra are from H_2 pure rotational lines.

The main PAH bands at 6.2, 7.7, 8.6, 11.2, 12.7 μm and the plateau at 17.0 μm are also prominent. This allows us to consider in our analysis a pixel by pixel comparison of the variations of C_{60} and PAHs. There are however some residual problems for the PAH bands: for instance, in NGC 2023 there is a dip around 10 μm which may due to saturation of the peak-up array as described in the IRS handbook³ (their Sect. 7.3.5). In both sources the issues are not relevant for the analysis since we focus on individual bands as fitted by `pahfit` and no such feature falls within the problematic wavelength range.

The total intensity of the 18.9 μm band is underestimated by the fit in some pixels. This issue is observed in NGC 2023 in pixels that lie to the South of the field. The origin of this problem comes from the continuum in these pixels, which drops above 20 μm and is not properly fitted, thus affecting the fit of the 18.9 μm band. In order to circumvent this issue and check the accuracy of the fit in other pixels, we consider a local linear continuum around 18.9 μm and later fit a Drude profile for the band itself. This procedure confirms that the difference between the result of `pahfit` and our fit of the 18.9 μm band is only significant in the aforementioned region. For these pixels,

³<http://irsa.ipac.caltech.edu/data/SPITZER/docs/irs>



2.4. Analysis

we use the result from our local fit rather than that of `pahfit`. Other bands in this area are not significantly affected by the misplaced continuum.

One difference between the NGC 2023 and Ced 201 is the band-to-continuum ratio. The PAH bands in Ced 201 have significantly lower intensity with respect to the continuum than those in NGC 2023. This is not the case for the $18.9\ \mu\text{m}$ C_{60} band, which has a similar band-to-continuum ratio in both sources. While hard to disentangle from the $\text{H}_2\ S(1)$ line and the $17.0\ \mu\text{m}$ plateau, the $17.4\ \mu\text{m}$ band also seems to have rather similar band-to-continuum ratios in both sources. This is indicative of a large contribution of C_{60} to this interstellar band (Sellgren et al. 2010; Berné & Tielens 2012; Peeters et al. 2012).

The high resolution spectra were also analyzed using `pahfit`. However, we must note that `pahfit` was created and optimized for fitting low resolution spectra, such as the ones considered here for Ced 201 and NGC 2023. In the case of RCW 49, the spectra were taken in SH mode for all regions considered here. This forced us to change the input parameters in `pahfit`: for the unresolved atomic and molecular lines we have changed the width of the Gaussian functions used, in order to match the improved resolution of the SH mode and we have modified some of the PAH band parameters to improve the fit.

The fitting procedure follows the same principle as in the low resolution mode. Besides the aforementioned modifications of some of the parameters, we also removed all features that fall outside the range covered by the SH mode since this causes problems with the fitting routine. If this last modification is not implemented then the wings of the adopted Drude profiles of the out-of-range PAH bands are sometimes fitted as part of the continuum.

The modified fitting routine runs into problems when the band-to-continuum ratio decreases. This is the case for region 1 in RCW 49. Specially at longer wavelengths, the fit either over- or underestimates the continuum, resulting in poor fits for the $18.9\ \mu\text{m}$ band. Furthermore, the $18.9\ \mu\text{m}$ band is not recognizable in the spectra of this region. The continuum at this wavelength is very strong and, as such, an $18.9\ \mu\text{m}$ band with intensity comparable with the highest value detected within other regions would not be noticeable. For this reason, we have decided to exclude region 1 from the rest of this study.

We looked for other potential errors in the continuum fits but, outside region 1, all fits are consistent with the data. In Fig. 2.6 we present an example of region 2 in RCW 49, which shows the strongest $18.9\ \mu\text{m}$ band. The $18.9\ \mu\text{m}$ band varies in intensity among the different regions, but can be recognized in the spectrum of most pixels. In some instances the detection is only marginal, but in our final analysis we exclude all points with detection below 3σ with respect to the error bars given by `pahfit`.

2.4.2. SPECTRAL MAPS

Once the spectrum for each pixel have been fitted, we build intensity maps of each of the PAH bands, the spectral lines and the $18.9\ \mu\text{m}$ band. We also create maps of the error bars, as derived by `pahfit`. These maps give the integrated intensity of each spectral feature and constitute the basis of our study. We restrict our analysis to areas

II. Fullerenes in photodissociation regions

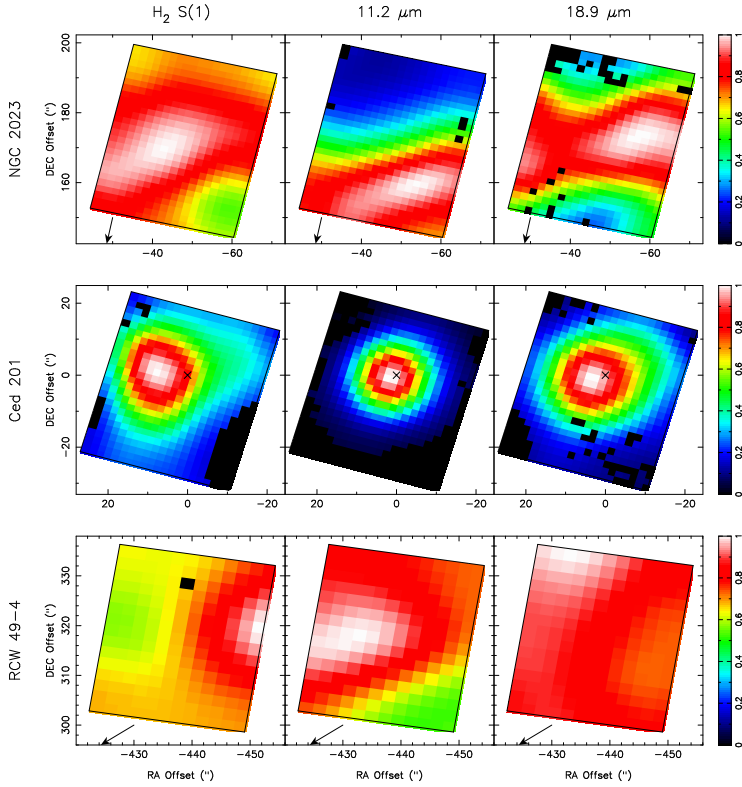
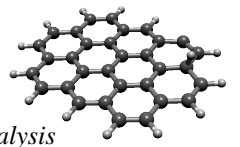


Figure 2.7.: Intensity maps of the selected spectral features: H₂ 0–0 $S(1)$ line, 11.2 μm PAH band and 18.9 μm C₆₀ band, all convolved to the PACS 70 μm beam. The top panels correspond to NGC 2023, the middle ones to Ced 201 and the bottom panels to Reg. 4 in RCW 49. The color scale is normalized with respect to the maximum intensity in the corresponding frame. The offsets are with respect to the position of the illuminating star, shown with a cross or pointed towards using arrows (for RCW 49 we chose the position of WR20a).

with confident detections, and thus we have flagged pixels in which the fitted intensity falls below a 3σ noise level. Finally, in order to get smoother images and correct for cases in which particular pixels have large differences in flux with respect to its neighbors, we performed a median filter with a 2×2 kernel.

In Fig. 2.7 we show maps of the 11.2 μm PAH band, the 18.9 μm band corresponding to C₆₀ and the H₂ 0–0 $S(1)$ line at 17.0 μm in NGC 2023, Ced 201 and region 4 of RCW 49. In all cases the PAH band peaks closer to the illuminating star than the C₆₀ or H₂ lines. This contrasts with the observations on NGC 7023, where C₆₀ peaks closer to the illuminating star than the PAHs.

In NGC 2023 we identify a bar-like structure in all the maps, running from the South-East to the North-West. However, the exact position of the bar varies: on the 11.2 μm map it is displaced to the South when compared to the 18.9 μm or H₂ $S(1)$ maps. Other



2.4. Analysis

variations observed in the bar concern the position of the peak intensity, with $18.9 \mu\text{m}$ displaying two peaks located towards the North-West and South-East of the bar, while $\text{H}_2 S(1)$ shows one peak located roughly in the middle of the bar and $11.2 \mu\text{m}$ showing also one peak, but displaced to the North-West.

The maps of Ced 201 show a clear asymmetry in the cases of the H_2 and C_{60} maps. This asymmetry is also present but in a less prominently in the PAH maps. In both the H_2 and C_{60} maps, the arc at the North-West appears much more clearly than in the PAH maps. Additionally, the peak intensity appears to the North-East of the star, in the position of the molecular cloud as shown in Fig. 2.2. In contrast, the PAH features are centered near the star and, for the 8.6 and $7.4 \mu\text{m}$ features, the spatial coincidence with IRAC $8 \mu\text{m}$ is very clear.

In RCW 49, the H_2 peak does not coincide the peak of the PAH bands, and is typically found further with respect to the illuminating star. The $18.9 \mu\text{m}$ maps shows only minor variations in intensity in most regions. As is the case for NGC 2023 and Ced 201, the $18.9 \mu\text{m}$ maps show a spatial distribution clearly different to that of the PAH maps in all the regions. In RCW 49, all PAH maps follow a similar pattern within each region, with only small changes in peak position and relative strengths. The PAH and C_{60} morphology show a superficial resemblance in a few regions, but the relative strength of the different components is very different.

In summary, in all sources where we detect the $18.9 \mu\text{m}$ band, its spatial distribution is noticeably different with respect to that of the PAH bands. Although the different PAH bands show spatial variations with respect to each other, they resemble each other much more closely than the $18.9 \mu\text{m}$ band. In most cases, the peak intensity of the C_{60} band is seen farther from the central star than the PAH bands. This behavior is the opposite of what is observed in NGC 7023 (Berné & Tielens 2012) and, in principle, does not seem to support the formation of C_{60} by UV processed PAHs. However, this divergence is seen purely from the point of view of projected distance and may not speak of the actual differences in physical conditions. As it has been suggested that the formation of C_{60} in the ISM starts with the dehydrogenation of PAHs — which is a balance between UV photolysis and reactions with H — we will consider in the next two subsections the intensity of the local radiation field and the hydrogen density.

2.4.3. UV FIELD CALCULATION

Considering that PAH and C_{60} are stochastically heated by UV-photons a measure of the UV field intensity is needed in order to derive proper abundances. The intensity of their respective mid-IR bands is proportional to the product of the column density of PAHs and C_{60} with the UV field intensity.

We determine the UV field intensity in terms of G_0 ($1.6 \times 10^{-3} \text{ erg cm}^{-2} \text{ s}^{-1}$; Habing 1968) from the FIR spectrum of dust. Considering that, in a PDR, nearly all the UV radiation is absorbed by dust and then re-emitted in the FIR and assuming that grains act like a modified black body (Tielens 2005, Sec. 9.7) we have,

$$G_0 = 8.3 \times 10^3 \frac{V}{\ell S} \tau_{v_0} v_0^{-\beta} \int v^\beta B(v, T_d) dv, \quad (2.1)$$

II. Fullerenes in photodissociation regions

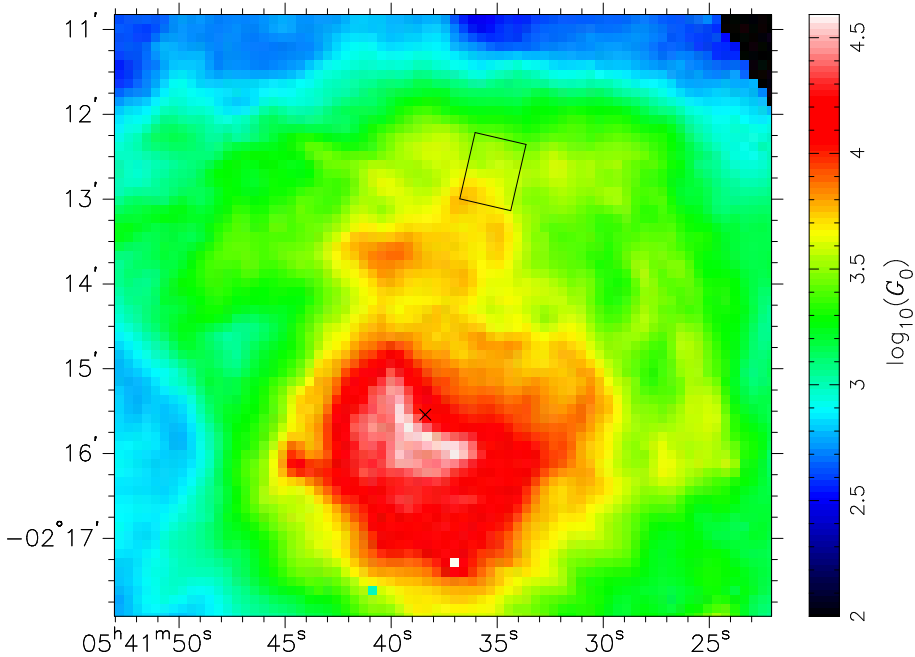
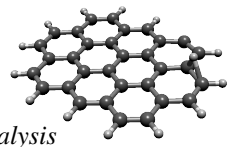


Figure 2.8.: Map of G_0 calculated from the FIR intensity for NGC 2023 with an assumed a spherical geometry, thus setting $V/\ell S = 1$. The cross shows the position of the illuminating star and the square the position of the IRS field.

where ν_0 is a reference frequency where the optical depth is τ_{ν_0} , β is the spectral index and T_d is the dust temperature. The factor $V/\ell S$ accounts for the geometry of the cloud, with S being the surface area facing the illuminating star, V the volume of the cloud and ℓ corresponding to the length along the line of sight. One issue with this calculation is that the three-dimensional geometry is generally not well known, introducing uncertainties. For example, for an edge-on disk the geometric factor would be equal to the ratio of the disk thickness over ℓ , while for a sphere this factor is equal to one. Since this method relies on the emission from dust, it will underestimate the value of G_0 in regions devoid of dust. In the three PDRs considered here the environment is dusty and the IRS fields are away from hard sources of radiation, so we expect our G_0 estimate to provide a reasonable approximation.

To calculate the total FIR intensity we use the PACS images at 70 and 160 μm from each source. For this, we first matched the 70 μm images to the 160 μm resolution and use the intensity of each pixel to fit a modified black-body to these two wavelengths. The free parameters are the dust temperature, T_d , and the optical depth τ_{ν_0} . We fixed ν_0 at 1000 GHz and considered $\beta = 1.7$. The value of β in the ISM is usually found to be somewhere between one and two, with a slight dependence on the dust temperature (Dupac et al. 2003). It has been observed that for $T_d \lesssim 20$ K, $\beta \simeq 2$, while for $T_d \gtrsim 30$ K a value of $\beta \simeq 1.5$ is found (Shetty et al. 2009). We chose an intermediate value since



2.4. Analysis

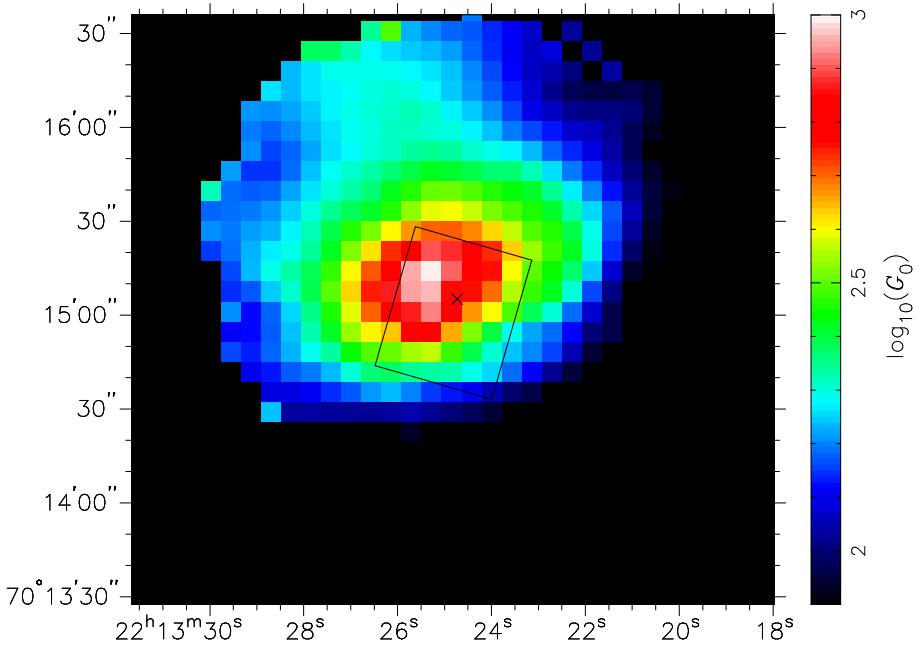


Figure 2.9.: Map of G_0 calculated from the FIR intensity for Ced 201 assuming spherical geometry ($V/\ell S = 1$). The cross shows the position of the illuminating star and the square corresponds to the IRS field.

in all sources we expect dust with temperatures in both regimes. We are not fitting β directly since we only have two points for our fit which is not enough to realistically fit three parameters. To make the fit we used a Levenberg-Marquardt fitting routine. With this fit, we derive the value of T_d and τ_{v_0} , which we use to determine G_0 .

We assumed spherical geometry in the three cases. For NGC 2023 (Fig. 2.8) this is likely a good assumption since the RN is almost circular, even though it is not exactly centered on the illuminating star. An additional correction factor must be added in eqn. 2.1 to account for the fact that, particularly for B-type stars, a significant part of the photons radiated have energies lower than 6 eV, that can heat the dust but do not correspond to the UV field as defined by G_0 . Based on the spectral type we use a factor of 0.7 for the fraction of the stellar luminosity falling in the range between 6 and 13.6 eV (Steiman-Cameron et al. 1997). We check our calculation against the result of Sheffer et al. (2011). They found $G_0 = 1.7 \times 10^4$ in NGC 2023 S, while the region we are focusing on is about 2.3 times farther out. This is equivalent to a geometric dilution factor of 5.3, leading to $G_0 = 3200$, which is in agreement with the values seen in Fig. 2.8.

In the case of Ced 201 (Fig. 2.9) the spherical cloud assumption is not entirely realistic since the PDR is due to a chance encounter with the molecular cloud and thus the star is situated at the edge of the cloud. In this case the peak of G_0 is displaced from

II. Fullerenes in photodissociation regions

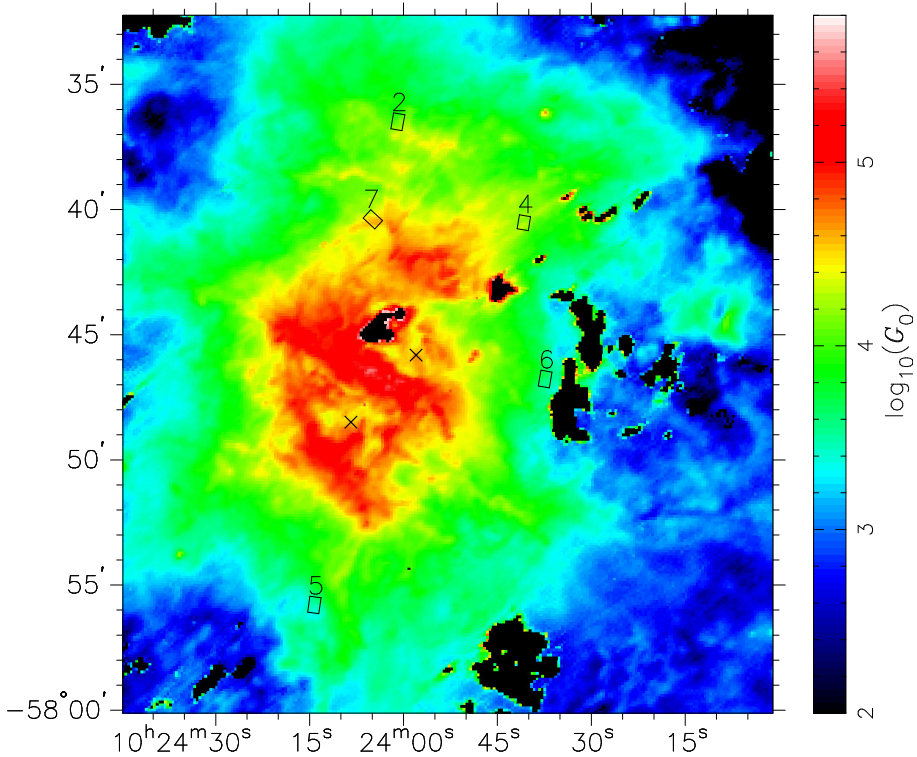
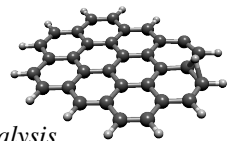


Figure 2.10.: Map of G_0 calculated from the FIR intensity for RCW 49 assuming spherical geometry ($V/\ell S = 1$). The crosses show the position of the illuminating stars and the squares the position of the five IRS fields for which we have density estimates.

the illuminating star and, furthermore, the region with highest G_0 corresponds to the arc structure seen North-East from BD +69 1231 in the molecular cloud, with much less intensity to the South-West. Due to its type, the fraction of the stellar luminosity emitted between 6 and 13.6 eV corresponds to 0.3 (Young Owl et al. 2002).

In RCW 49 (Fig. 2.10), the exact three-dimensional geometry is not well known, but it looks approximately circular and we expect that the spherical approximation will not introduce large errors. We will take into account in our discussion the possible effects that arise from changing the geometrical factor. Since the illuminating source of RCW 49 is dominated by the O-type stars we consider a factor of one for the fraction of the luminosity emitted in the far-UV. In reality, a significant fraction will be emitted at wavelengths shorter than 13.6 eV in this case, but these photons are absorbed and downgraded in the HII region.

For the additional PDRs included in this work we only used the the far-IR calculation of G_0 for Orion’s Veil, resulting in G_0 ranging from $\simeq 30000$ for the I2 field (the closest to the Bar) to ~ 3000 – 5000 for the fields that lie farther from the Bar. For NGC 7023 we used the values derived by Berné & Tielens (2012), which result in $G_0 = 10000 \pm 7000$



2.4. Analysis

at the peak of the $18.9 \mu\text{m}$ band. The Horsehead nebula was studied by Abergel et al. (2003), who find $G_0 \sim 100$. For IC 63 we use the estimate of Jansen et al. (1994), which gives $G_0 \sim 650$.

Finally, comparing Figs. 2.1–2.3 against Figs. 2.8–2.10, the general structure seen in the composite images is clearly apparent in the G_0 distribution. The G_0 maps show the most characteristic features in the case of each PDR, such as the southern and northern ridges in NGC 2023, the bright bar observed in RCW 49 between the positions of WR20a and WR20b and the arc-like structure seen in Ced 201 to the North-East of BD +69 1231. The derived dust temperatures inside the IRS fields of the three PDRs range between 20 and 40 K, which is much too low for emission to be due to C_{60} embedded in grains.

2.4.4. THE ATOMIC HYDROGEN DENSITY

In order to estimate the variations in abundance of PAHs and C_{60} with respect to the physical conditions of each source we need to derive the atomic hydrogen densities, $n(\text{H})$, for each region. We estimate these based on previous studies and we derive a single value as representative for each of the regions we consider. A summary of the results for each field is presented in Table 2.1.

For NGC 2023 we base our estimate on the densities calculated by Pilleri et al. (2012). Their model uses a varying density inside the IRS field, which ranges from $2.4 \times 10^3 \text{ cm}^{-3}$ to $2 \times 10^4 \text{ cm}^{-3}$. We consider their value for the density of the inner part of the field, since it dominates the emission.

In the case of Ced 201 we base our estimate of $n(\text{H})$ on the values for total hydrogen density and molecular densities from Kemper et al. (1999) and Young Owl et al. (2002). The G_0 value derived from the IR measurement is in good agreement with the value derived from the PDR/molecular cloud analysis of Kemper et al. (1999). As they included more reliable density tracers, we have adopted their value for $n(\text{H})$ and the IR derived value for G_0 .

In RCW 49 we calculate the density based on an analysis of rotational lines of molecular hydrogen. The H_2 rotational line emission is modeled following the procedure outlined in Sheffer et al. (2011). The IRS SH observations mentioned in Sect. 2.3.1 are used to derive the H_2 0–0 $S(1)$ to $S(4)$. We additionally use LL observations to cover the H_2 0–0 $S(0)$ line. PDR models are used to fit each field individually, giving H_2 column densities and reference values of n_0 . For a typical PDR, hydrogen in the surface layer is predominantly atomic and we have $n(\text{H}) = n_0$. In dense PDRs, however, the H/H_2 transition is pulled to the surface and the atomic fraction varies from 1 to 10^{-3} . For our sources, this seems to apply in RCW 49 regions 2 and 4. For these two positions, we hence adopted the atomic H fraction at $A_V = 0.5$; $f_{\text{H}} = 10^{-3}$ and 10^{-1} for regions 2 and 4 respectively. It must be noted that these values are highly uncertain.

The value derived for NGC 7023 by Berné & Tielens (2012) is of $n(\text{H}) = 150 \pm 100 \text{ cm}^{-3}$. For Orion’s Veil, we estimate $n(\text{H})$ by using the electron densities derived from $[\text{SII}]$ optical lines by Rubin et al. (2011). From their values we use a factor 20 to derive the neutral density (Tielens 2005). In the Horsehead nebula, Abergel et al. (2003) estimate the density just behind the ionization front to be $8 \times 10^3 \text{ cm}^{-3}$. Finally,

II. Fullerenes in photodissociation regions

Table 2.1.: Average physical conditions and C_{60} fractions.

Region	$n(H)$ (cm^{-3})	G_0	$G_0/n(H)$	$f_{C,C_{60}}$ ($\times 10^{-5}$)	Ref.
NGC 2023	2.4×10^3	5200 ± 200	2.1	4.2	1
Ced 201	1.2×10^4	600 ± 60	0.050	44	2
RCW 49-2	4.0×10^3	11000 ± 1300	2.7	13	3
RCW 49-4	1.0×10^4	20000 ± 3000	2.0	7.2	3
RCW 49-5	2.5×10^4	3000 ± 400	0.12	11	3
RCW 49-6	2.5×10^4	5100 ± 300	0.21	12	3
RCW 49-7	2.5×10^4	34000 ± 2500	1.4	5.5	3
NGC 7023	1.5×10^2	10000 ± 7000	60	9.9	4
Veil-I2	8.7×10^3	31000 ± 1900	3.6	56	5,6
Veil-I1	8.1×10^3	22000 ± 500	2.7	41	5,6
Veil-M1	5.1×10^3	15000 ± 600	2.9	36	5,6
Veil-M2	5.1×10^3	13000 ± 600	2.5	32	5,6
Veil-M3	5.1×10^3	8700 ± 400	1.7	29	5,6
Veil-M4	3.4×10^3	5400 ± 200	1.6	30	5,6
Veil-V1	1.7×10^3	3500 ± 100	2.0	35	5,6
Veil-V2	2.6×10^3	5200 ± 100	2.0	31	5,6
Horsehead	8.0×10^3	~ 100	0.013	< 4.3	7
IC 63	3.0×10^3	~ 650	0.22	< 6.0	8,9

For NGC 2023, Ced 201, RCW 49 and the Veil, the values of G_0 were calculated following the procedure described in Sec. 2.4.3. Other values of G_0 and $n(H)$ are taken from the given references. For NGC 7023 we use lower limits for G_0 and present the values at the peak of C_{60} abundance.

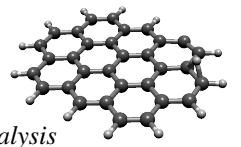
(1) Pilleri et al. (2012); (2) Kemper et al. (1999); (3) This work; (4) Berné & Tielens (2012); (5) Boersma et al. (2012); (6) Rubin et al. (2011); (7) Abergel et al. (2003); (8) Jansen et al. (1994); (9) Thi et al. (2009).

in the case of IC 63, we consider the results from Thi et al. (2009), who give a range from 1000–5000 cm^{-3} for the PDR density.

For all the PDRs considered here, the values of $n(H)$ carry uncertainties that are difficult to estimate. Since we are using a single value as representative for each region, we have that the variations of $G_0/n(H)$ within each field will be representative of variations of G_0 only.

2.4.5. CARBON FRACTION VARIATIONS

In this section we present results of the variations in abundance of both PAHs and C_{60} . We calculate the abundances from the ratio of intensity of PAHs and C_{60} with respect to G_0 , which in turn is related to the FIR intensity of large dust grains. Assuming that PAHs, C_{60} and dust compete for the same photons, we follow Tielens (2005,



2.4. Analysis

Sec. 6.7), and use,

$$f_C = 0.23 \left(\frac{7 \times 10^{-18} \text{ cm}^2}{\sigma_{\text{FUV}}} \right) \frac{f_{\text{IR}}}{1 - f_{\text{IR}}}, \quad (2.2)$$

where f_{IR} is the ratio of the PAHs or C_{60} total intensities to the total IR intensity (Berné & Tielens 2012, given by eqn. 2.1 for the FIR and adding the contributions from PAHs and C_{60} , following), σ_{FUV} is the far-UV absorption cross section per carbon atom of the species under consideration. Finally, f_C is the fraction of elemental carbon locked in the species considered, which is in turn related to the total abundance.

In this calculation, we consider the total PAH intensity as the addition of all the PAH bands below $15 \mu\text{m}$. For NGC 2023 and Ced 201 this includes features starting from $\lambda = 5 \mu\text{m}$. In the case of RCW 49, NGC 7023 and Orion's Veil our coverage is limited to the range between $10\text{--}15 \mu\text{m}$ since the data in these cases have been recorded using the SH mode. Considering the contribution that this range has to the total PAH intensity in NGC 2023 and Ced 201 we find that it is fairly constant fraction at ~ 0.2 . We use this value as a correction factor in order to estimate the total PAH abundance in RCW 49, NGC 7023 and Orion's Veil. A final correction is needed also for the SH data arising from the difference in flux measurements with respect of the LL data. Using the flux of the $11.2 \mu\text{m}$ feature from NGC 7023 in both LL and SH modes we find this additional factor to be ~ 3 . Given that the mismatch between the resolution of our G_0 maps and the C_{60} and PAH intensity maps, we re-project and convolve the intensity maps to the PACS $160 \mu\text{m}$ resolution, which is the same as the resolution of our G_0 maps.

In order to calculate the total intensity of C_{60} and PAHs at the position of the corresponding PDRs, we measure $I_{18.9}$, I_{PAH} and I_{FIR} at the position were the combined emission from the available PAH bands peaks. We need to include the contributions to $I_{\text{C}_{60}}$ from the bands at 8.5 and $7.0 \mu\text{m}$ which are hidden under PAH emission and the $17.4 \mu\text{m}$, which has some contribution from PAH emission. Considering a first order approximation, we use a value of 0.6 for the ratio of the 17.4 and $18.9 \mu\text{m}$ band intensities (Peeters et al. 2012), and 0.4 for the ratio of both the 7.0 and $8.5 \mu\text{m}$ with respect to $18.9 \mu\text{m}$ (Berné & Tielens 2012). The exact value of these ratios, however, is not precisely determined (Bernard-Salas et al. 2012), but even when considering other calculated values for the intrinsic rates, we find differences of at most a factor of two.

Using the carbon fractions derived in the previous section, we compare the results for our sources with other values found in the literature. In NGC 7023 the observation of growth in C_{60} ranges from 10^{-5} to 10^{-4} (Berné & Tielens 2012). A study of C-rich, H-poor PNe by García-Hernández et al. (2011) shows a range in the carbon fraction in C_{60} from 3×10^{-5} up to 3×10^{-3} , with most objects falling in the range of $\sim 10^{-4}$. All these previous estimates include the contributions to $I_{\text{C}_{60}}$ from the bands at 17.4 , 8.5 and $7.0 \mu\text{m}$. The value of f_C in all PDRs considered here fall within $3 \times 10^{-5}\text{--}6 \times 10^{-4}$, which is in good agreement with the values found in the aforementioned studies.

The results of f_C for both PAHs and C_{60} in the different PDRs with respect to $G_0/n(\text{H})$ are presented in Fig. 2.11. For PAHs, a decrease can be observed with increasing $G_0/n(\text{H})$ — in regions where $G_0/n(\text{H}) < 1$ — from $f_C \simeq 0.08$ until $f_C \simeq 0.01$.

II. Fullerenes in photodissociation regions

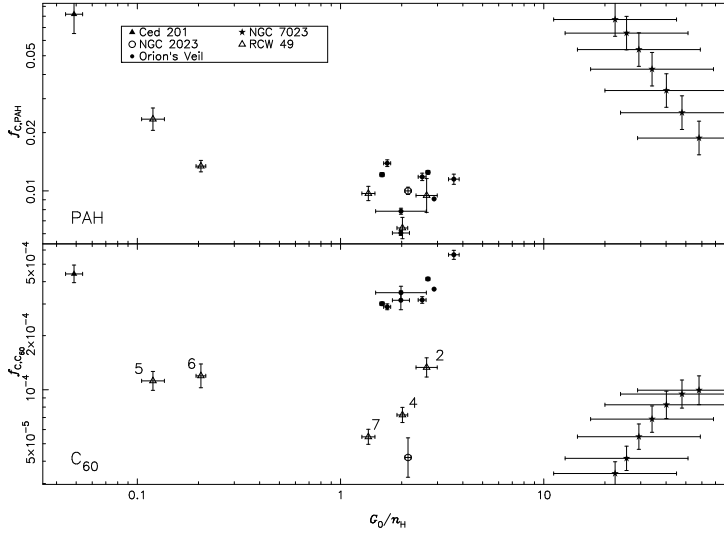


Figure 2.11.: Variations of the carbon fraction locked in PAHs (top) and C_{60} (bottom) with respect to $G_0/n(H)$. The different symbols indicate the different PDRs included in this work for which C_{60} is detected. For RCW 49, the numbers correspond to the individual regions considered.

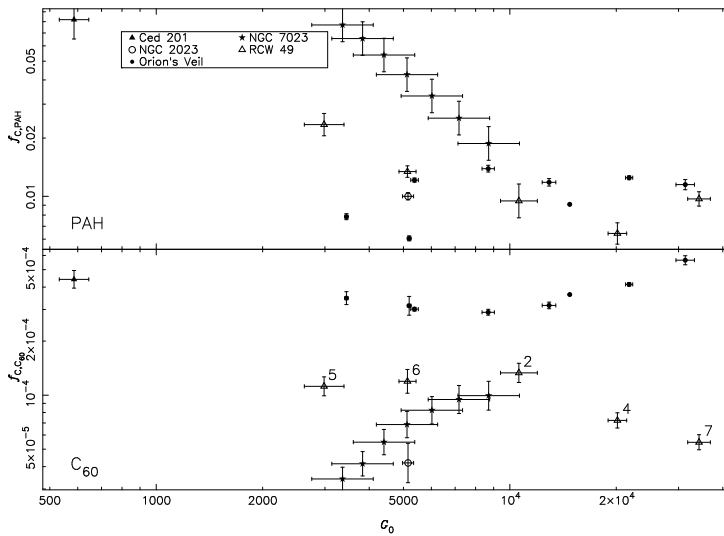
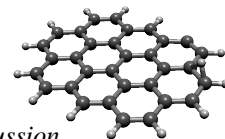


Figure 2.12.: Variations of the carbon fraction locked in PAHs (top) and C_{60} (bottom) with respect to G_0 . The different symbols indicate the different PDRs included in this work for which C_{60} is detected. For RCW 49, the numbers correspond to the individual regions considered.



2.5. Discussion

For $G_0/n(\text{H})$ within 1–4 there is substantial scatter, even within single sources. In contrast, NGC 7023 shows a clear trend, with higher abundance than in other regions for $G_0/n(\text{H})$ between 10 and 100. The behavior observed in NGC 7023 is similar that observed for the other regions in the range of $G_0/n(\text{H}) < 1$.

For C_{60} no general trend that can be applied to all the regions can be observed. However, within individual objects, there is an increase in the abundance in RCW 49, NGC 7023 and Orion’s Veil. In the case of RCW 49 the increase in abundance does not apply for the full range. For $G_0/n(\text{H}) < 1$ the abundance of C_{60} within RCW 49 appears to remain constant. Furthermore, even for $G_0/n(\text{H}) > 1$ the trend is not as clear, particularly considering that it includes regions 2 and 4, which have poorly determined hydrogen densities. In NGC 7023 and Orion’s Veil the increase holds for the full probed range, although none of these regions has $G_0/n(\text{H}) < 1$. We cannot conclude if this behavior applies as well for NGC 2023 or Ced 201 since we have single points for these PDRs.

Figure 2.12 shows again f_{C} variations of both species, in this case with respect to G_0 alone. For the PAHs fractions, a decrease in abundance is observed in NGC 7023 and, to a lesser extent, in RCW 49. The abundance in Orion’s Veil is consistent with a fairly constant value. The case of C_{60} abundance again shows trends within individual regions. In NGC 7023 and Orion’s Veil there is an increase in C_{60} abundance along the probed range. In Orion’s Veil this increase is observed at $G_0 > 10^4$, while for NGC 7023 the increase seems to halt when G_0 approaches 10^4 . On the other hand, RCW 49 shows a decrease in C_{60} abundance, which also begins at $G_0 \sim 10^4$.

2.5. DISCUSSION

By examining Figs. 2.11 and 2.12, we conclude that within NGC 7023, there is a clear trend for a decrease in PAH abundance and an increase in C_{60} abundance with increasing $G_0/n(\text{H})$ (or with increasing G_0 as the density is constant). The other regions show a more mixed behavior. In RCW 49, for example, the PAH abundance decreases with increasing $G_0/n(\text{H})$ or G_0 , but the trend in the C_{60} abundance is less clear. In contrast, for Orion’s Veil, there is no clear trend in the PAH abundance but a hint of an increase in the C_{60} abundance with $G_0/n(\text{H})$, while the trend with G_0 is unclear for both species. We attribute the distinctiveness of the trend in NGC 7023 to the fact that the PDR is seen edge-on, while for other regions the morphological and geometrical characteristics are more uncertain and might play a role in the observed trends or lack thereof. Combining all sources together there is no obvious trend for either species with respect to $G_0/n(\text{H})$ or G_0 . From this, we conclude that besides the physical conditions — G_0 and $n(\text{H})$ — there must be other parameter(s) influencing the evolution of PAHs and fullerenes.

The clear trends in the PAH and fullerene abundances with G_0 in NGC 7023 have been interpreted in a simple model, describing the chemical evolution of PAHs under the influence of the stellar UV photons through H-loss to graphene sheets resulting ultimately, on the one hand, into small hydrocarbons due to C_2 fragmentation and, on the other hand, to fullerenes through isomerization (Berné & Tielens 2012). We

II. Fullerenes in photodissociation regions

note that time is an additional factor entering such chemical models. Specifically, H-loss is expected to be described by a balance between collisional hydrogenation and UV-driven dehydrogenation and thus regulated by G_0 and $n(\text{H})$. However, C_2 -loss is likely to be a time-dependent process controlled by G_0 . Hence the absence of a general trend in the PAH and fullerene abundances across many sources is not to be expected. Moreover, it should be realized that PAH fragmentation and fullerene formation are only connected for PAHs in excess of at least 60 C-atoms.

PAH abundance appears to be related to the age of the PDRs. We observe the highest PAH abundance in Ced 201 and NGC 7023, the youngest sources in our sample, with their ages estimated to be 1500 and 10^5 yr, respectively (Alecian et al. 2008). For the remaining PDRs we find similar, overlapping age estimates: 1–7 Myr for NGC 2023 (López-García et al. 2013), 2–3 Myr for RCW 49 (Piatti et al. 1998) and 1–3 Myr for Orion’s Veil (Flaccomio et al. 2003). For these PDRs we find a lower abundance of PAHs than in Ced 201 or NGC 7023, which is consistent with a time-dependent destruction of PAHs.

Recently, the first step in the processing from PAHs to fullerenes has been modeled in detail by Montillaud et al. (2013). The results of this model are shown in Fig. 2.13. To the left of this figure, PAHs are fully hydrogenated while to the right they are expected to fully dehydrogenated — i.e. graphene flakes. More specifically, the lines in this figure represent the loci at which the hydrogenation balance leads to a constant H-fraction on a PAH of a given size. So, the further to the right, the more of the initial PAH size distribution will be destroyed but as long as the PAH size distribution extends to ~ 100 C-atoms, some fraction of the PAHs will remain hydrogenated. The different sources in our sample are indicated by symbols in this figure. We note that the sources without detectable C_{60} are to the left of the “stability-line” for PAHs in excess of 60 C-atoms, leading some credence to a photochemical transformation model of PAHs into fullerene in the ISM. However, the C_{60} /PAH abundance ratio does not correlate well with the “depth” into the fully dehydrogenated zone. This may merely indicate that time is of the essence or that there are fluctuations in the size distribution of the PAH family from region to region. Ced 201 forms an interesting exception to this as it has C_{60} despite being in the “stable-zone” for PAHs with more than 60 C-atoms. This is a very peculiar source as it is a chance encounter of the illuminating star with a cloud. This star-cloud interaction seems to have led to a shock wave (Cesarsky et al. 2000) located in the position where the C_{60} abundance is particularly high. Hence, it is tempting to speculate that in this particular source C_{60} is formed by shock processing of PAHs and/or dust grains. The inferred shock velocity is quite low ($\sim 10 \text{ km s}^{-1}$ Witt et al. 1987) and such low velocity shocks are not expected to lead to much PAH destruction (Micelotta et al. 2010). However, observed C_{60} /PAH abundance is only 0.005 and thus little processing is required.

Finally, small HAC grains have also been considered as photochemical starting points for C_{60} formation in the ISM. The general process involved is the same: the first step requires dehydrogenation of the HAC particles followed by a shrinking of the resulting cage (Micelotta et al. 2012). As for PAHs, the hydrogenation of HAC is set by a balance between reactions with H and photochemical H-loss (Mennella et al. 2001, 2002; Mennella 2006) and therefore controlled by $G_0/n(\text{H})$ (Chiar et al. 2013). The

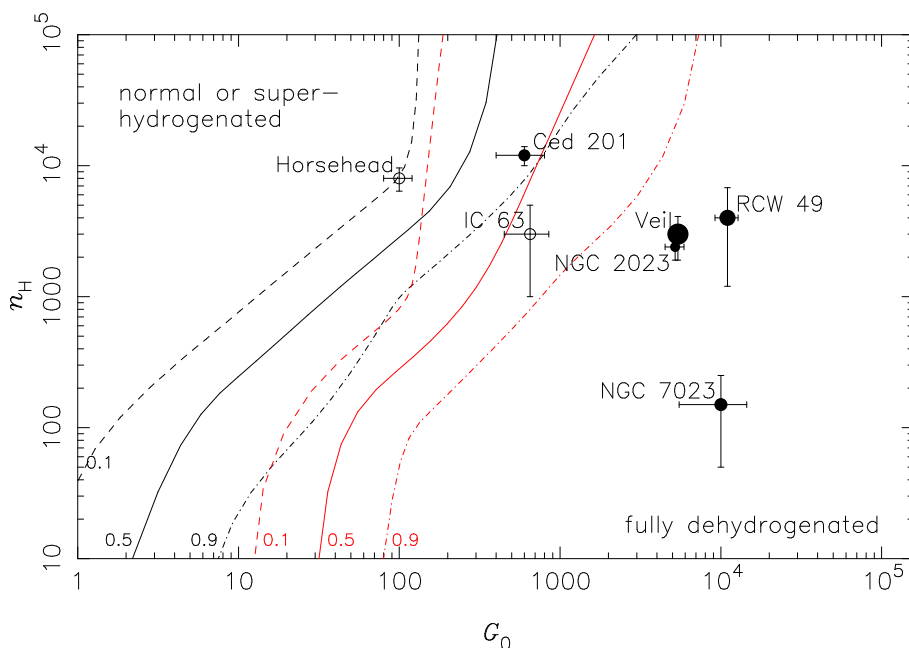
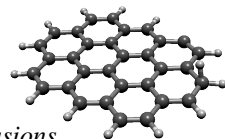


Figure 2.13.: Hydrogenation state of circumcoronene ($C_{54}H_{18}$; black) and circumvalene ($C_{66}H_{20}$; red) as function of G_0 and the atomic hydrogen density. The labels of the lines indicate the fraction of the respective molecules that is fully dehydrogenated. The full circles correspond to the PDRs where we detect C_{60} , the symbol size is proportional to the C_{60} -to-PAH ratio. The sources for which we can only derive upper limits are marked by open circles. The error bars mark the ranges for the physical conditions. The data on hydrogenation states of $C_{54}H_{18}$ and $C_{66}H_{20}$ were taken from Montillaud et al. (2013).

main difference with the PAH model resides in the timescale for C-loss. Based upon molecular dynamics calculations (Zheng et al. 2007), this C-loss timescale is calculated to equal the IR-cooling timescale at 100–200 K for HACs and such a low temperature is readily attained by HAC grains containing ~ 500 C-atoms (or less). However, the adopted C-binding energies are only 0.36 eV (Micelotta et al. 2012), which is much less than expected for carbon cages. As emphasized in the original molecular dynamics study, these results may not be statistically significant (Irlé, S., private communication, Zheng et al. 2007). Further laboratory studies will have to settle this issue.

2.6. CONCLUSIONS

We present a survey of C_{60} in PDRs. While in NGC 2023 the presence of fullerenes had already been established (Sellgren et al. 2010; Peeters et al. 2012), the detection on RCW 49 and Ced 201 represent new sources where C_{60} is confirmed to be present. We also quantified its abundance as a fraction of elemental carbon and found values

II. Fullerenes in photodissociation regions

consistent with other studies of C_{60} in PDRs, with values ranging from $\sim 3 \times 10^{-5}$ to $\sim 6 \times 10^{-4}$. Furthermore, the values we derive for T_d from FIR observations indicate that these regions have temperatures ranging from 20 to 40 K, which is too low for C_{60} to be emitting in grains, and supports the idea of a gas phase species or small sized clusters undergoing stochastic heating (Sellgren et al. 2010). The well-known strong IR bands at 6.2, 7.7, 8.6, 11.2, 12.7 and 16.4 μm , show a very similar spatial behavior, with only minor variations in all sources. In contrast, the spatial distribution of the 18.9 μm band is very different and we conclude that this band has a different carrier (i.e., C_{60} Cami et al. 2010; Sellgren et al. 2010) than the other bands (i.e., PAHs).

While some of the sources appear to show trends in C_{60} and PAH abundance, we find universal dependence with either $G_0/n(\text{H})$ or G_0 when considering all PDRs together. We consider age as a factor explaining the lack of a general trend. Comparing our observational results to the model predictions of Montillaud et al. (2013) for PAH dehydrogenation, we find that regions where C_{60} is detected have physical conditions consistent with full dehydrogenation of PAHs of at least 60 C-atoms, with the exception of Ced 201. The conditions of regions where only upper limits for C_{60} abundance could be derived, are consistent with only partial dehydrogenation of PAHs with relevant sizes. These results support models where the dehydrogenation of carbonaceous species is the first step towards C_{60} formation (Berné & Tielens 2012; Micelotta et al. 2012).

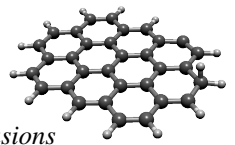
More observations aimed at measuring variations of C_{60} abundance with respect to both PAHs and HAC, as well as better determinations of $n(\text{H})$ are needed to confirm the reality of these trends and the more likely parent species. Better constraints on the age estimates and the study of additional PDRs with significant age differences are needed to test our hypothesis about the effect of age in generating the seemingly independent trends for each PDR.

ACKNOWLEDGMENTS

Studies of interstellar chemistry at Leiden Observatory are supported through the advanced-ERC grant 246976 from the European Research Council, through a grant by the Dutch Science Agency, NWO, as part of the Dutch Astrochemistry Network, and through the Spinoza premie from the Dutch Science Agency, NWO. PC acknowledges support from a Huygens fellowship at Leiden University. We would like to thank B. Ochsendorf and H. Andrews for facilitating us their reduced spectra of B 33 and IC 63 respectively. We would also like to thank J. Montillaud for the data on dehydrogenation state of PAHs. We also acknowledge the anonymous referee, whose comments helped us in improving this paper.

This work is based in part on observations made with the *Spitzer Space Telescope*, which is operated by the Jet Propulsion Laboratory, California Institute of Technology under a contract with NASA.

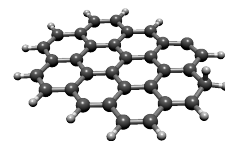
The *Herschel* spacecraft was designed, built, tested, and launched under a contract to ESA managed by the Herschel/Planck Project team by an industrial consortium under the overall responsibility of the prime contractor Thales Alenia Space (Cannes),



2.6. *Conclusions*

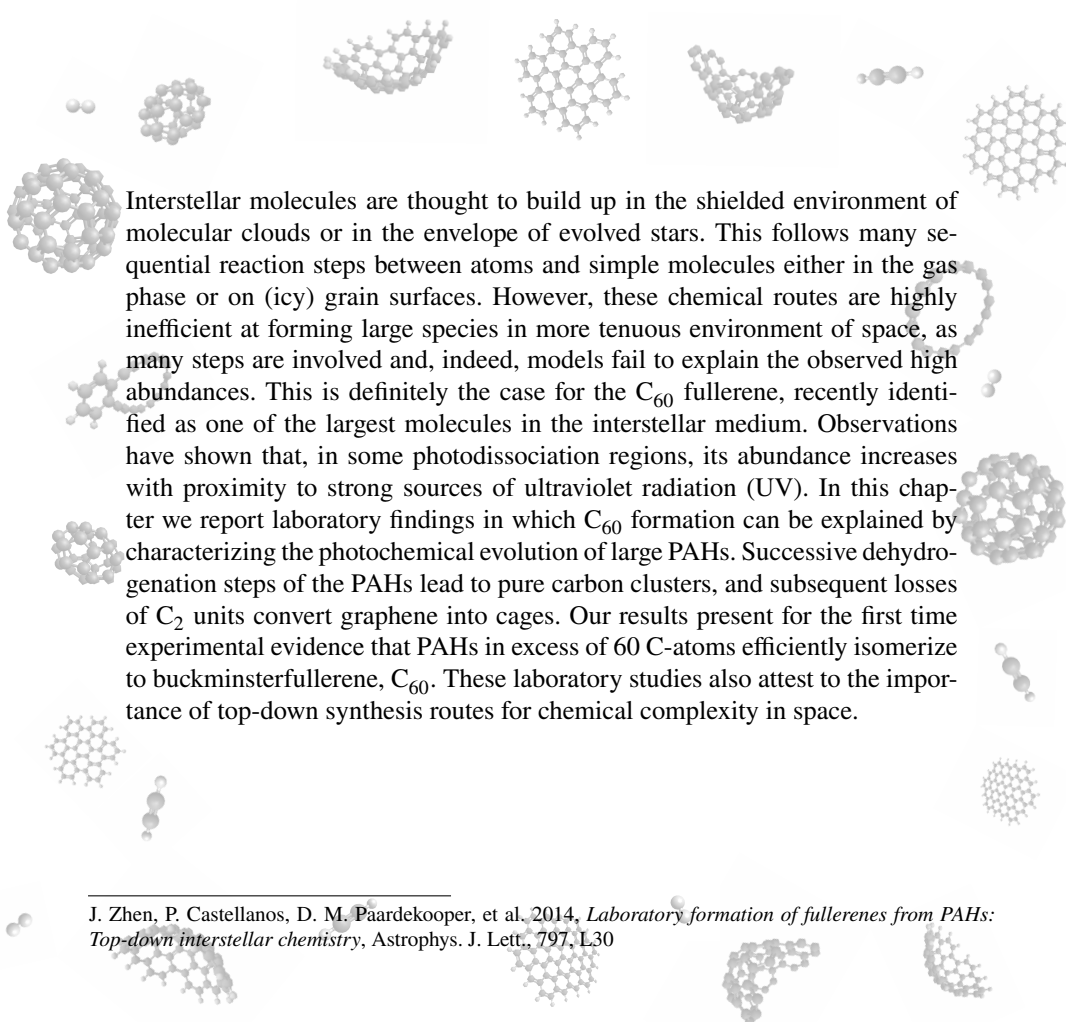
and including Astrium (Friedrichshafen) responsible for the payload module and for system testing at spacecraft level, Thales Alenia Space (Turin) responsible for the service module, and Astrium (Toulouse) responsible for the telescope, with in excess of a hundred subcontractors.

PACS has been developed by a consortium of institutes led by MPE (Germany) and including UVIE (Austria); KU Leuven, CSL, IMEC (Belgium); CEA, LAM (France); MPIA (Germany); INAF-IFSI/OAA/OAP/OAT, LENS, SISSA (Italy); IAC (Spain). This development has been supported by the funding agencies BMVIT (Austria), ESA-PRODEX (Belgium), CEA/CNES (France), DLR (Germany), ASI/INAF (Italy), and CICYT/MCYT (Spain).



III

FORMATION OF FULLERENES FROM PAHS



Interstellar molecules are thought to build up in the shielded environment of molecular clouds or in the envelope of evolved stars. This follows many sequential reaction steps between atoms and simple molecules either in the gas phase or on (icy) grain surfaces. However, these chemical routes are highly inefficient at forming large species in more tenuous environment of space, as many steps are involved and, indeed, models fail to explain the observed high abundances. This is definitely the case for the C_{60} fullerene, recently identified as one of the largest molecules in the interstellar medium. Observations have shown that, in some photodissociation regions, its abundance increases with proximity to strong sources of ultraviolet radiation (UV). In this chapter we report laboratory findings in which C_{60} formation can be explained by characterizing the photochemical evolution of large PAHs. Successive dehydrogenation steps of the PAHs lead to pure carbon clusters, and subsequent losses of C_2 units convert graphene into cages. Our results present for the first time experimental evidence that PAHs in excess of 60 C-atoms efficiently isomerize to buckminsterfullerene, C_{60} . These laboratory studies also attest to the importance of top-down synthesis routes for chemical complexity in space.

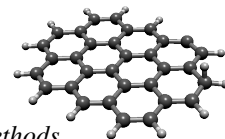
J. Zhen, P. Castellanos, D. M. Paardekooper, et al. 2014, *Laboratory formation of fullerenes from PAHs: Top-down interstellar chemistry*, *Astrophys. J. Lett.*, 797, L30

3.1. INTRODUCTION

Over the last 80 years, observational studies have revealed the presence of ~ 180 different molecules in space (Herbst & van Dishoeck 2009; Tielens 2013). Because of intrinsic limitations in observational techniques, the molecular inventory revealed by these studies is heavily biased towards small polar species, radicals, and linear carbon chains with electronegative groups (e.g., CN). Also larger stable molecules containing 6–10 atoms, like methanol and ethylene glycol have been identified (Herbst & van Dishoeck 2009). With the advent of infrared space missions, a richer and more diverse molecular universe was brought to light (Tielens 2008, and references therein). Most mid-infrared spectra are dominated by broad features at 3.3, 6.2, 7.7, 8.6 and 11.2 μm , generally attributed to infrared fluorescence of large (50–100 C-atoms) polycyclic aromatic hydrocarbon (PAHs) molecules pumped by ultraviolet (UV) photons (Tielens 2008, and references therein). These molecules contain $\sim 10\%$ of the elemental carbon and play an important role in the ionization and energy balance of the interstellar medium (ISM) of galaxies. Recently, in addition to these PAH bands, the infrared signatures of buckminsterfullerene (C_{60}) were also observed at 7.0, 8.5, 17.4 and 18.9 μm (Cami et al. 2010; Sellgren et al. 2010). PAH bands are prominent in planet-forming disks around young stars (Habart et al. 2006; Doucet et al. 2007) and PAHs as well as C_{60} are important components of solar system meteorites (Sephton & Botta 2008; Becker & Bada 1994). Hence, understanding the processes that regulate the origin and evolution of these species and their relationship to the organic inventory of space has become a focus in astrochemistry.

In the tenuous ISM, direct synthesis of PAHs and fullerenes from small hydrocarbon species is inhibited (McEwan et al. 1999) and PAHs are generally thought to form in the C-rich ejecta of asymptotic giant branch stars as molecular intermediaries or byproducts of the soot formation process (Frenklach & Feigelson 1989; Cherchneff et al. 1992). In the ISM, these species are then processed by ultraviolet photons, which leads initially to their ionization. Subsequently, UV photolysis results in dissociation, and sequential steps of double H-losses, have been identified as the dominant fragmentation channel, leading to pure carbon clusters, likely in the form of graphene sheets (Ekern et al. 1998; Joblin 2003; Berné & Tielens 2012; Zhen et al. 2014). After complete dehydrogenation, ongoing photolysis will break down the carbon skeleton leading to smaller carbon species. It has been suggested that highly excited graphene sheets may also isomerize to more stable carbon cages or fullerenes (Berné & Tielens 2012). Rapid transformation of graphene flakes into the C_{60} fullerene is observed in electron irradiation experiments of graphene on surfaces (Chuvilin et al. 2010). Fullerenes also fragment in a strong UV field through the loss of C_2 units, shrinking the size of the cage until the smallest photostable fullerene, C_{32} , is reached (Handschuh et al. 1995). From this point on, fragmentation leads to the formation of rings and chains (Lifshitz 2000).

Photodissociation Regions (PDRs) provide a natural laboratory for the study of the interaction of UV photons with carbonaceous species (Pety et al. 2005; Rapacioli et al. 2005; Hollenbach & Tielens 1999). Observations with the *Spitzer Space Telescope* and the *Herschel Space Observatory* of the prototypical PDR, NGC 7023, have revealed



3.2. Experimental methods

that the C_{60} abundance increases by an order of magnitude while the PAH abundance decreases when approaching the illuminating star (Berné & Tielens 2012). These observations point towards the important role of photochemistry in the destruction of interstellar PAHs and that C_{60} is likely a photochemical product of PAHs (Berné & Tielens 2012). So far, experimental evidence of this process has been lacking.

In this letter, we present laboratory results demonstrating the formation of fullerenes (in particular C_{60}) from large PAHs by photolysis, based on the difference in absorption properties as a function of wavelength (Kato et al. 1991). We compare and contrast the fragmentation pattern of fullerenes (C_{60} and C_{70}) to that of PAHs and their fragmentation products. As the C_{60} fullerene does not absorb at 532 nm, while PAHs and other fullerenes absorb efficiently, the absorption behavior of C_{60} fragments produced by photolysis of PAHs can be used to establish the presence of C_{60} fullerenes.

3.2. EXPERIMENTAL METHODS

We have studied the fragmentation of fully benzenoid PAH cations and fullerene cations in the laboratory using i-PoP, our instrument for photodynamics of PAHs, which is described in detail in Zhen et al. (2014). Briefly, PAHs or fullerenes are sublimated in an oven, at an appropriate temperature, ionized by an electron gun, and transported into a quadrupole ion-trap via an ion gate. Later, the cations are irradiated by many (typically ~ 18) pulses from a nanosecond pulsed Nd:YAG laser, leading to sequential steps of fragmentation. The ion-trap content is subsequently released and analyzed using a reflectron time-of-flight mass spectrometer. Each fragmentation step is initiated by absorption of multiple photons; the exact number depends on the laser wavelength. The process is heavily biased towards dissociation through the lowest energy channel (Zhen et al. 2014).

Here, we study the photofragmentation behavior of the large PAH cations $C_{60}H_{22}^+$ ($m/z = 742.172$), $C_{66}H_{26}^+$ ($m/z = 818.203$), and $C_{78}H_{26}^+$ ($m/z = 962.203$). The mass spectra are contrasted with those resulting from photofragmentation of the fullerene cations C_{60}^+ ($m/z = 720$) and C_{70}^+ ($m/z = 840$), in order to investigate the formation of C_{60} from large PAHs. These particular PAHs are selected because their armchair edges provide them with greater stability than PAHs with zigzag edges (Poater et al. 2007; Koskinen et al. 2008), which may favor their presence in space. Indeed, PAHs with armchair edges are observed to be more abundant in regions close to strong UV sources (Candian et al. 2014).

3.3. RESULTS

Studies at our laboratory and elsewhere have shown that, for small PAHs, several fragmentation channels are available (e.g., H-loss, C_2H_2 -loss; Jochims et al. 1994). However, for large PAHs, fragmentation is almost exclusively through sequential hydrogen loss (Ekern et al. 1998; Joblin 2003; Zhen et al. 2014). As an example, the dehydrogenation of $C_{66}H_{26}^+$ the hydrogenation state moves progressively towards fully

III. Formation of fullerenes from PAHs

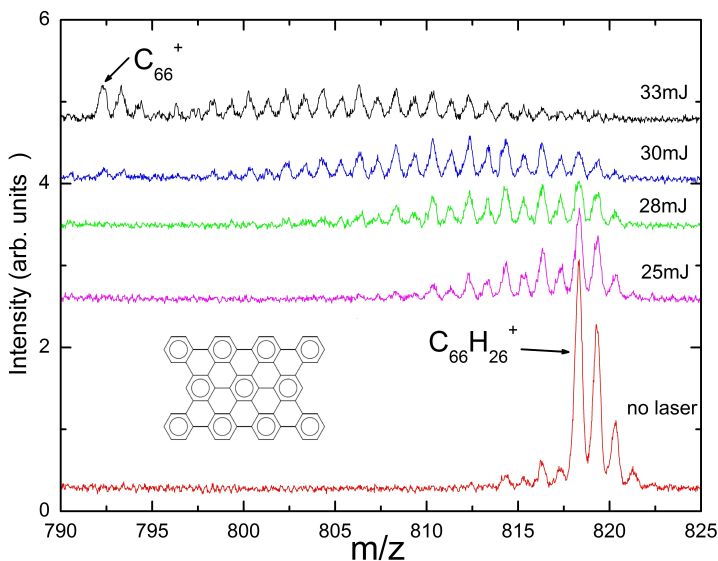
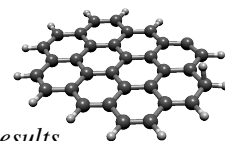


Figure 3.1.: The fragmentation pattern of the fully benzenoid cation, $C_{66}H_{26}^+$, irradiated at 355 nm as a function of laser power. Additional peaks in the no-laser trace are isotopes and fragmentation produced by the electron gun.

dehydrogenated species (Fig. 3.1). At even higher laser powers, these pure carbon molecules and the fullerenes fragment through the loss of C_2 units (Fig. 3.2), as has been observed in other studies (Lifshitz 2000).

Fullerene formation in graphite vaporization experiments routinely gives rise to “magic numbers” of C-atoms (60, 56, 50, 44) with enhanced abundances compared to neighboring peaks, reflecting their greater stability (Zimmerman et al. 1991). We can use this pattern as an indication of the formation of fullerene structures in our photofragmentation studies. Panels a and b in Fig. 3.2 show the fragmentation through C_2 losses experienced by C_{60}^+ , $C_{60}H_{22}^+$, $C_{66}H_{26}^+$ and C_{70}^+ at 266 nm and 355 nm, respectively. We observe that, in both cases, the fullerene “magic number” mass peaks show an enhanced intensity with respect to neighboring peaks irrespective of the parent molecule except for the C_{60}^+ fragment from $C_{60}H_{22}^+$, where the enhancement is minimal when compared to that of the other parent molecules. The differences observed between the two wavelengths are due to variations in laser power — at shorter wavelengths, the laser system has a limited power output —, which is particularly clear for the PAHs, where the smallest fragments are not produced at 266 nm.

Figure 3.3 shows the carbon losses for the same species at 532 nm. In this case, the dissociation behavior of the fullerenes and PAHs is markedly different. For the fullerenes, the dissociation stops when reaching clusters with 60 C-atoms (in the case of C_{60}^+ no dissociation is observed). The PAHs considered here experience fragmentation up to much smaller masses. However, there is a striking difference in the behavior of the



3.3. Results

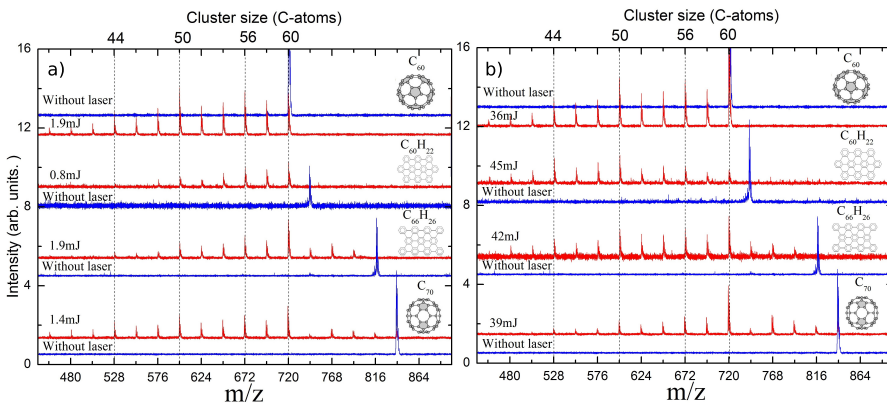


Figure 3.2.: A comparison of the fragmentation pattern of the fully benzenoid cations, $C_{60}H_{22}^+$ and $C_{66}H_{26}^+$, and the fullerene cations, C_{60}^+ and C_{70}^+ , irradiated at 266 (a) and 355 nm (b). Note that the fragmentation pattern of the PAHs resembles that of the fullerenes. The “magic numbers” are marked by the vertical dashed lines and correspond to peaks with an m/z of 720 for C_{60}^+ , 672 for C_{56}^+ , 600 for C_{50}^+ and 528 for C_{44}^+ .

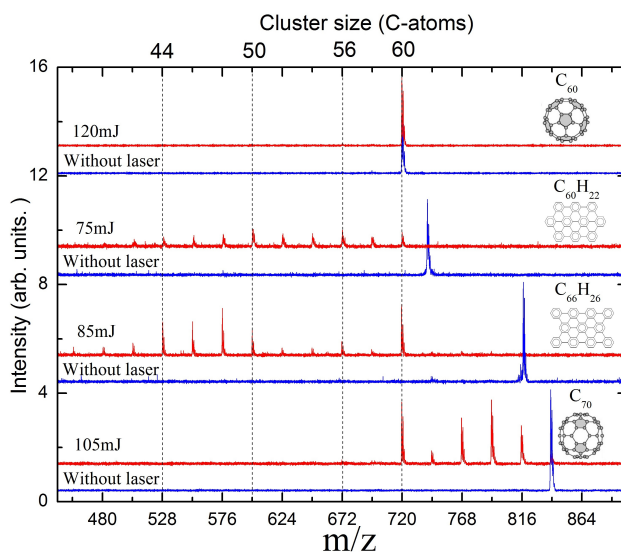


Figure 3.3.: A comparison of the fragmentation pattern of the molecules considered in Fig. 3.2, irradiated at 532 nm. At this wavelength, the fullerene C_{60}^+ cation does not absorb and no fragmentation is observed. The C_{60}^+ species produced from $C_{60}H_{22}^+$ fragment readily to smaller clusters, while those produced from $C_{66}H_{26}^+$ show a mixed fragmentation behavior. As in Fig. 3.2 the vertical dashed lines correspond to the fullerene “magic numbers”.

III. Formation of fullerenes from PAHs

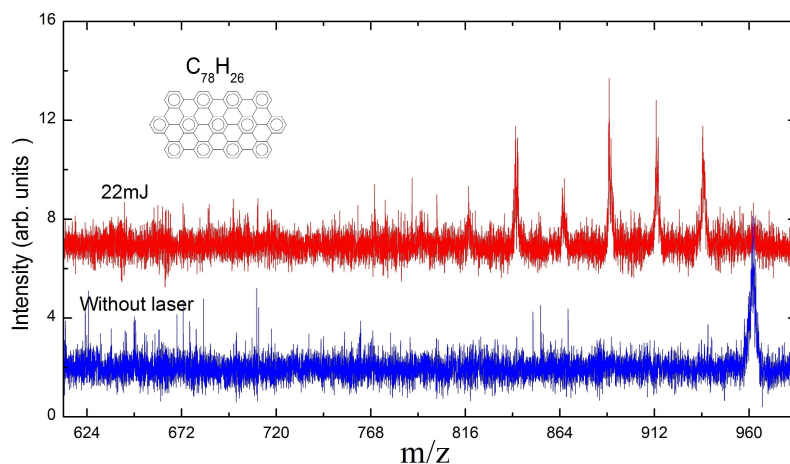
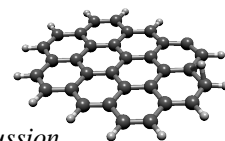


Figure 3.4.: Fragmentation pattern of the fully benzenoid cation, $C_{78}H_{26}^+$, irradiated at 355 nm. Note that carbon clusters with 70 C-atoms ($m/z = 840$) show enhanced abundances. Due to signal-to-noise limitations this spectrum was taken at energies lower than those from Fig. 3.2. For this reason fragmentation to lower masses is not achieved.

C_{60}^+ peak. For $C_{60}H_{22}^+$ this peak does not appear to be special when compared to those further down the line, while in the case of $C_{66}H_{26}^+$ it shows a clear enhancement and remains even when all neighboring peaks have practically disappeared.

The kinetics of the fragmentation process is controlled by the absorption properties of the parent species and its daughter products, and by the dissociation energy of the fragmentation channels involved. The dependence on absorption properties provides a tool with which the fragmentation products can be probed. The PAH cations and the fullerenes C_{60}^+ and C_{70}^+ as well as their products absorb well at 266 and 355 nm (Kato et al. 1991; Mallocci et al. 2007). However, C_{60}^+ does not absorb at 532 nm (Kato et al. 1991) and thus does not fragment, even at very high laser powers (Fig. 3.3). For C_{70}^+ , it is clear that C_{60}^+ is formed, thus halting the fragmentation at 532 nm. The fragmentation pattern of $C_{60}H_{22}^+$ is not indicative for a hard to dissociate 60 C-atom cluster, ruling out formation of significant amounts of buckminsterfullerene. Fragmentation of the pure carbon cluster produced from $C_{66}H_{26}^+$ can be represented by a combination of the behavior of the fullerene C_{70}^+ and that of the $C_{60}H_{22}^+$ PAH cation, indicating formation of the C_{60} fullerene.

The formation of fullerenes from large PAHs may be a more general process. The fragmentation pattern observed for $C_{78}H_{26}^+$ shows an enhanced intensity of the peak corresponding to the C_{70}^+ carbon cluster, as illustrated in Fig. 3.4.



3.4. Discussion

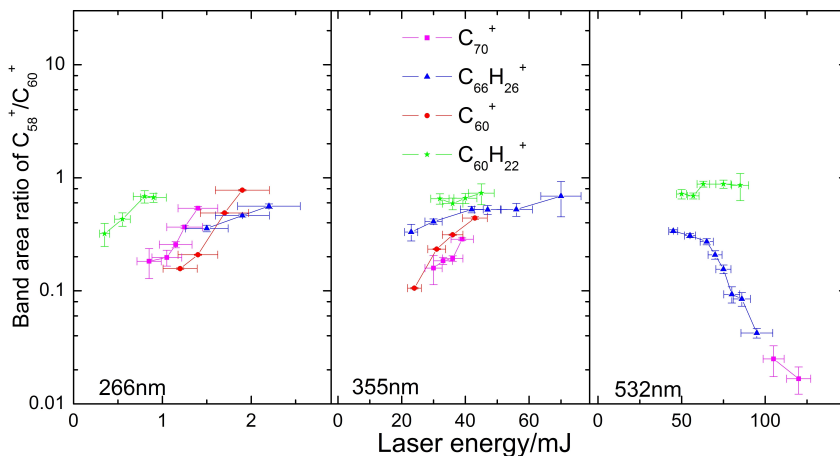


Figure 3.5.: The ratio of the integrated intensity for C_{58}^+/C_{60}^+ as function of laser energy at different wavelengths — 266 nm, 355 nm and 532 nm. For the first two wavelengths, the behavior of this ratio for PAH and fullerene cations is very similar. At 532 nm, the behavior of the ratio from $C_{60}H_{22}^+$ deviates from that of the other molecules considered.

3.4. DISCUSSION

The fragmentation pattern of PAHs and fullerenes — specifically the route through C_2 loss from C_{60} — can be quantified through the C_{58}^+/C_{60}^+ ratio. Figure 3.5 demonstrates the similarity in behavior of the C_{60}^+ fragments produced from the PAHs and fullerenes at 266 and 355 nm. However, at 532 nm, the C_{60}^+ fragments produced from $C_{66}H_{26}^+$ behave like those produced from C_{70}^+ (i.e. there is very little fragmentation even at high laser power), while the C_{60}^+ fragments produced from $C_{60}H_{22}^+$ behave similarly to the other wavelengths and fragment readily.

Based on Figs. 3.3 and 3.5, we conclude that fragmentation of $C_{66}H_{26}^+$ leads to the presence of both non-fullerene C_{60}^+ isomer(s) as well as the C_{60}^+ fullerene. We conclude that the loss of C_2 units from the pure carbon cluster, C_{66}^+ , initiates isomerization of some of the initial fully dehydrogenated PAHs to fullerene cages, which — similar to the C_{70}^+ fullerene — subsequently shrink to smaller and smaller fullerene cages. The results show that this process is very efficient, and a large fraction of the initial clusters ($\sim 20\%$ at 85 mJ) are channeled to the C_{60}^+ fullerene. In contrast, since the isomerization process is initiated by C_2 -loss, the C_{60}^+ fullerene formation channel is essentially closed for the C_{60}^+ produced by dehydrogenating $C_{60}H_{22}^+$ and this species fragments fully to smaller species at 532 nm. We note though that the fragmentation pattern of this PAH for products with $m/z < 720$ resembles that of the fullerenes C_{60} and C_{70} , with peak enhancements at the “magic numbers”. Hence, after the C_{60}^+ formed from $C_{60}H_{20}^+$ loses the first C_2 , isomerization to cages can be initiated and at this point further fragmentation follows the “cage-route” as well.

Molecular dynamics calculations of the transformation of graphene flakes to ful-

III. Formation of fullerenes from PAHs

lerenes have revealed that, at high temperatures, this folding process starts through transformation of hexagons at the edges of the flake to various polygons (Lebedeva et al. 2012). Our experiments suggest that the polygon formation associated with this folding process can also be initiated by the loss of C_2 units from the edges of the fully dehydrogenated PAHs and that, once the process is started, it is “self-sustaining” and the chemical energy released quickly drives the complete reconstruction of the dehydrogenated PAH to a fullerene cage.

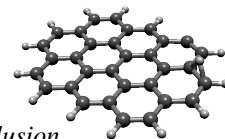
In summary, we conclude that photofragmentation of PAHs with more than 60 C-atoms leads to the formation of buckminsterfullerene (C_{60}). However, fullerenes are not the only products and isomers with different absorption and stability properties are also formed.

3.5. ASTROPHYSICAL RELEVANCE

In contrast to our laboratory studies, excitation of PAHs in PDRs is due to single photon absorption. However, irrespective whether one or multiple photons are involved, rapid intramolecular vibrational redistribution will leave the species highly vibrationally excited from which it relaxes either through fragmentation or infrared fluorescence. From our experiments it is not possible to derive the activation energy for the different fragmentation channels and further experiments are needed to confirm if these energies can be reached by single photon absorption in the ISM. In the present study, we will assume that this is the case and, hence, we directly apply our experimental results to the photoprocessing of PAHs in space.

Our results provide further insight in the evolution of PAHs in the PDR associated with the reflection nebula NGC 7023. The processes taking place in this nebula are representative for other similar environments in space. In this region, winds from the young Herbig Be star, HD 200775, have blown a cavity in the molecular cloud inside which the star was formed (Fuente et al. 1998). This cavity has broken open to the surrounding ISM. The PAH abundance is observed to decrease — starting at $\sim 25''$ from the star (some $20''$ inside of the PDR front; well within the cavity) from about 7×10^{-2} of the elemental carbon to about 2×10^{-2} of the elemental carbon at $10''$ from the star. The fullerene abundance increases from about 10^{-5} at the PDR front to about 10^{-4} some $10''$ from the star (Berné & Tielens 2012).

We can now interpret these observations in terms of the laboratory results presented here and the model described by Berné & Tielens (2012) and Montillaud et al. (2013). The first step in the PAH destruction and fullerene formation process is the loss of peripheral H. H-coverage of PAHs is a balance between UV induced fragmentation and reactions with atomic H and is controlled by the parameter $\gamma = G_0/n(H)$, where G_0 is the intensity of the UV radiation field in terms of the average interstellar radiation field (Habing 1968) and $n(H)$ is the atomic hydrogen density in cm^{-3} (Tielens 2005; Le Page et al. 1997). For small γ , a given PAH species will be fully hydrogenated while for large γ , it is fully dehydrogenated and the transition between these two hydrogenation states is very rapid. The critical value of γ separating these two cases is not well known and depends on the PAH size. According to Berné & Tielens (2012), values of



3.6. Conclusion

$\gamma \approx 3$ and $\gamma \approx 100$ can be calculated for circumcoronene, $C_{54}H_{18}^+$, and circumvalene, $C_{66}H_{20}^+$, respectively, based upon kinetic parameters adopted from experimental studies on small PAHs (Jochims et al. 1994; Tielens 2005). Montillaud et al. (2013) on the other hand, adopting slightly different values for the kinetic parameters, predict that for circumcoronene 50% of the species are fully dehydrogenated for $\gamma \approx 4 \times 10^{-2}$ while for circumvalene, this occurs at $\gamma \approx 4 \times 10^{-1}$. Further experimental studies for large PAHs relevant for the ISM will have to settle this issue.

We can compare these values to the γ appropriate for the PDR in NGC 7023. In the cavity of NGC 7023, between 12 and 25'' from the star, where most of the PAH to fullerene conversion is observed to occur, γ is estimated to change from 65 to 650 (Berné & Tielens 2012), well into the regime where PAHs in excess of 60 C-atoms will become dehydrogenated. Species that become fully dehydrogenated are rapidly converted into cages but only those initially larger than 60 C-atoms will form C_{60} . The high stability of C_{60} allows it to accumulate over irradiation time, as can be deduced from Fig. 3.5.

The observed high fraction of PAHs destroyed inside the cavity and the relatively small amount of C_{60} formed in NGC 7023 coupled with the seemingly high efficiency with which large PAHs are converted into the fullerene C_{60} in our experiments suggests then that the population of interstellar PAHs is heavily skewed towards PAHs smaller than 60 C-atoms. The typical size of the interstellar PAH population is not well known. In principle, the ratio of the intensity of the CH stretching mode to the CH out-of-plane bending mode ($I_{3.3}/I_{11.2}$) is a measure of the average size of the emitting PAHs (Alamandola et al. 1989; Draine & Li 2001; Ricca et al. 2012). However, the infrared spectrometer on the *Spitzer Space Telescope* did not extend to 3.3 μm while the beam of the Short Wavelength Spectrometer on board of the *Infrared Space Observatory* encompasses the full PDR in NGC 7023. Taking those latter values (Peeters et al. 2002) and a typical excitation energy of 7 eV appropriate for a B3 star ($T_{\text{eff}} = 17000$ K), the observed ratio (0.27) translates into an average size of ~ 60 C-atoms for the emitting PAHs in NGC 7023 (Ricca et al. 2012). Given the beam averaging in these observations, this typical size is likely an overestimate. Furthermore, comparisons of matrix isolation experiments with DFT calculations suggest that the latter tends to overestimate the intrinsic strength of the C–H stretch mode by a factor of two (Langhoff 1996). Further observational and experimental studies are required to address these issues.

3.6. CONCLUSION

In agreement with earlier studies, our photofragmentation studies reveal that PAH cations initially fragment through rapid H-loss. The resulting completely dehydrogenated species fragment further through sequential steps of C_2 losses. We compared the results of the fragmentation of the pure carbon clusters formed from PAH cations with those of the fullerenes for different wavelengths.

Using the wavelength dependent absorption cross-section properties of C_{60}^+ , we demonstrate that PAH fragments formed from PAHs that initially contain more than 60 C-atoms isomerize — among others species — to the fullerene C_{60} . The presence

III. Formation of fullerenes from PAHs

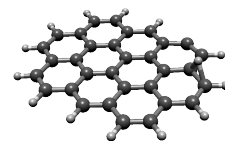
of “magic number” peaks in the fragmentation pattern of smaller PAHs suggests that these isomerize to small cages.

Based on our experimental studies, we have analyzed observational results of PAHs and fullerenes in the NGC 7023 PDR, and conclude that the observed PAH and C₆₀ relative abundances imply an interstellar PAH size distribution skewed to sizes $\lesssim 60$ C-atoms. These experiments provide direct support for the importance of top-down photochemistry for the formation of fullerenes in the ISM, as well as other species. However, it must be noted that further experiments are needed to determine the relevant fragmentation energies and the feasibility that photons with these energies are available in the ISM.

Finally, we recognize that, in a laboratory setting, the efficient complete dehydrogenation of PAHs provides a novel way to synthesize pure carbon clusters (most likely graphene flakes) of very specific sizes. Given the present interest in graphene, this synthesis method holds much potential for the study of such species under fully controlled conditions and will allow a validation of theoretically predicted properties by experiments.

ACKNOWLEDGMENTS

We are grateful to M.J.A. Witlox and R. Koehler for technical support. We are grateful to L.J. Allamandola who provided the large PAH sample. Studies of interstellar chemistry at Leiden Observatory are supported through advanced-ERC grant 246976 from the European Research Council, through a grant by the Dutch Science Agency, NWO, as part of the Dutch Astrochemistry Network, and through the Spinoza premie from the Dutch Science Agency, NWO.



IV

PHOTOINDUCED PAH DEHYDROGENATION

Polycyclic aromatic hydrocarbons (PAHs) constitute a major component of the interstellar medium carbon budget. Sequential fragmentation induced by energetic photons leads to the formation of new species, including fullerenes. However, the exact chemical routes involved in this process remain largely unexplored. In this work, we focus on the first photofragmentation steps, involving dehydrogenation. We consider a multidisciplinary approach, taking into account the results from experiments, density functional theory (DFT) calculations, and modeling using dedicated Monte-Carlo simulations. By considering hydrogen roaming along the edges of the molecule, we are able to characterize the most likely photodissociation pathways for the molecules studied here. The formation of aliphatic side groups is found to be critical for the first fragmentation and sets the balance between H- and H₂-loss. The presence of trio hydrogens, especially in combination with bay regions in small PAHs, plays an important part in the experimentally observed variations in the odd-to-even H-atom loss ratios. As PAH size increases, H₂ formation becomes dominant, and sequential hydrogen loss only plays a marginal role. In order to match theoretical and experimental results in large PAHs with solo hydrogens, we have modified the energy barriers and restricted the H-hopping to tertiary atoms. H₂-loss from large PAHs appears to be the dominant channel, suggesting an efficient formation path for H₂ in photodissociation regions (PDRs).

P. Castellanos, A. Candian, J. Zhen, et al. 2018, *Photoinduced PAH dehydrogenation: The competition between H- and H₂-loss*, *Astron. Astrophys.*, in press

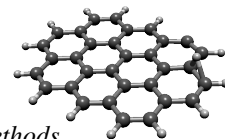
4.1. INTRODUCTION

Polycyclic aromatic hydrocarbons (PAHs) are generally accepted as carriers of the aromatic infrared bands (AIBs), a family of emission features that dominate the mid-infrared spectrum of most astronomical objects containing dust and gas (Tielens 2013, and references therein). Infrared space telescopes such as *Spitzer* have allowed further insight into the composition of the astronomical PAH family and other large C-containing molecules, such as the fullerene C_{60} , which has been unambiguously identified in planetary nebulae (e.g., Cami et al. 2010; García-Hernández et al. 2012; Otsuka et al. 2013) and in photodissociation regions (PDRs, Sellgren et al. 2010; Berné & Tielens 2012; Boersma et al. 2012). Berné & Tielens (2012) noted a clear anticorrelation of the intensity of the PAH and the fullerene IR-bands in NGC 7023. Based on this, they proposed that fullerenes can be formed in PDRs through photodestruction of large PAHs ($N_C \geq 60$) following the absorption of ultraviolet (UV) photons. The first step of this process involves the stripping of the hydrogen atoms from the edge of the molecule. This would be followed by C_2 -loss and isomerization, effectively folding the dehydrogenated PAH into a closed fullerene structure (Berné et al. 2015). Support for this model has been provided by observations of other fullerene containing PDRs (chapter II).

Chapter III presented experimental evidence supporting fullerene formation through PAH photodestruction. However, the details of this mechanism are still not understood. Studies regarding the first stage of such process — dehydrogenation — have been limited mostly to small PAHs and consider only the lower energy channels (Ling et al. 1995; Ling & Lifshitz 1998; Ekern et al. 1998; West et al. 2014). Appearance energies (AE) for the lowest energy channels, namely H-, H_2 - and C_2H_2 -loss, have been measured experimentally for PAHs up to coronene (Jochims et al. 1994). These experiments show that the preferred fragmentation channel is H-loss for all but one of the studied molecules and that the AEs for H- and C_2H_2 -loss are very close in energy — e.g., for the triphenylene cation ($C_{18}H_{12}^+$) they correspond to 16.1 ± 0.3 and 16.7 ± 0.3 eV, respectively (Jochims et al. 1994).

All experimental studies on PAH dehydrogenation show the same pattern: photo-products with an even number of hydrogen atoms have systematically higher abundances than those that retain an odd number of hydrogens (Ekern et al. 1998; West et al. 2014; Zhen et al. 2014). Additionally, PAHs with less than 24 carbon atoms do not reach full dehydrogenation before acetylene (C_2H_2) loss starts competing with pure dehydrogenation (Ekern et al. 1997; West et al. 2014), while larger PAHs appear to reach full dehydrogenation before carbon losses become important (Ekern et al. 1998; Zhen et al. 2014).

Direct fragmentation of PAHs is not the only process that needs to be taken into account upon irradiation. Isomerization in general and hydrogen hopping in particular, is known to proceed efficiently at internal energies below the threshold for direct dissociation (Bauschlicher & Ricca 2014; Paris et al. 2014; Chen et al. 2015; Trinquier et al. 2017a,b). Considering a molecule with two adjacent hydrogen atoms on the edge, as coronene for example, the molecule hybridization changes locally from sp^2 to sp^3 when a hydrogen shifts, resulting in an aliphatic-like bond and an empty carbon cen-



4.2. Experimental methods

ter. Isomerization can affect the fragmentation behavior. For example, aliphatic C–H bonds are notoriously weaker than aromatic C–H bonds (Paris et al. 2014; Trinquier et al. 2017a). Additionally, there is the possibility to lose molecular hydrogen from such an aliphatic site with a transition state significantly lower than the corresponding transition state from a fully aromatic structure (Paris et al. 2014). This mechanism has been proposed as alternative formation route of H₂ on PAH molecules in PDRs (see Wakelam et al. 2017, for a recent review). Other isomerization pathways lead to alterations of the carbon skeleton, i.e., the formation of dangling ethynyl or vinyl groups, or rearrangement of the hexagons into pentagons and/or heptagons (Bouwman et al. 2016; Trinquier et al. 2017b).

Here we report a systematic study of the H-loss pathway in PAHs under laser irradiation using ion trap time-of-flight mass spectrometry in Sect. 4.2 (Zhen et al. 2014). To interpret the experimental data, Density functional theory (DFT) calculations are used to evaluate the rates of isomerization reactions, which are then implemented in a Monte-Carlo simulation to identify the dominant fragmentation channels (Sect. 4.3). In Sect. 4.4 we detail both the experimental and theoretical results. As explained in Sect. 4.4.3, we have restricted our analysis on the isomerization to reactions exclusively involving hydrogen hopping, without modifications on the carbon skeleton. Considering these simplifications, we have limited our results to the first four hydrogen losses. As dehydrogenation progresses further, rearrangements of the carbon structure is expected to affect the validity of our results. We discuss our results in the context of previous work and its astrophysical implications in Sect. 4.5. Finally, the main conclusions and possible directions for future research are summarized in Sect. 4.6.

4.2. EXPERIMENTAL METHODS

This work encompasses nine PAHs, whose chemical formulas and structures are summarized in Fig. 4.1. These PAHs were selected as they represent a diverse range of sizes and edge structures and are commercially available. We have focused on medium to large sized PAHs, as they are thought to be more representative of interstellar PAHs. A number of small PAHs have also been included within our sample, in order to compare and validate our results against previous work.

We performed the current experiments with our instrument for photodynamics of PAHs (i-PoP) in the Sackler Laboratory for Astrophysics at Leiden Observatory. A more in-depth description of the system has been provided in Zhen et al. (2014). Relevant details, together with the specific conditions of the current set of experiments, are provided here. The set-up consists of a quadrupole ion trap (QIT) connected to a time-of-flight mass spectrometer (TOF-MS), in order to confine and irradiate precursors and to analyze their photoproducts. Commercially obtained samples of each molecule studied (Fig. 4.1) were introduced into an oven one at a time. The oven was then placed under vacuum in the same chamber as the QIT, and subsequently heated up to the sublimation temperature of the selected precursor species. Typical values range from 315 K (triphenylene) to 600 K (dicoronylene). The working pressure of the QIT chamber is $\sim 5.0 \times 10^{-7}$ mbar.

IV. Photoinduced PAH dehydrogenation

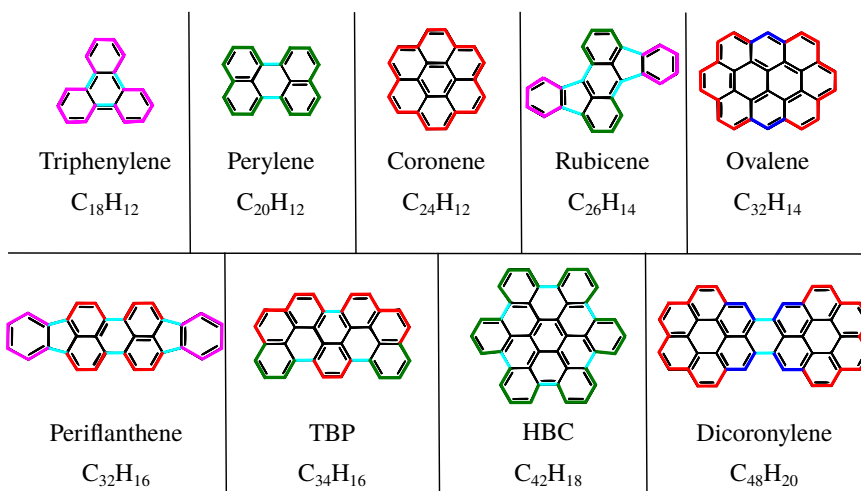
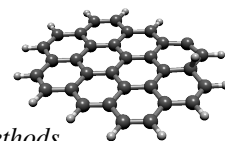


Figure 4.1.: Structures and chemical formula of the nine PAHs studied in this paper. TBP identifies tribenzoperopyrene and HBC hexabenzocoronene, respectively. The different edge structures are highlighted with different colors: solo (blue), duo (red), trio (green) and quarto (fuchsia). Edge bonds without hydrogens attached correspond to bay regions (cyan), which can take different forms.

Each operation cycle consisted of ionization, QIT filling, mass isolation and irradiation. Ionization of the gas-phase molecules was achieved via electron impact, which also induced partial dehydrogenation. The ions thus produced were then guided into the QIT using ion-optics plates. After filling the QIT for 3 s, the ion-optics voltages were set so as to prevent additional molecules from reaching the trap. Helium gas was injected continuously into the QIT chamber to cool down the ions and thus reduce the size of the ion cloud, increasing the overlap between it and the laser beam. A $\sim 650 \mu\text{s}$ long SWIFT pulse was then applied to the end caps of the QIT in order to isolate the isotopically pure parent species. The efficiency of the SWIFT mass-selection varied for different molecules, and it generally worsened as molecular mass increased. The selected ions were then irradiated with a Nd:YAG pumped dye-laser, with a repetition rate of 10 Hz. We used DCM as a dye, tuning the dye-laser to produce radiation at 656 nm (~ 2 eV). By using photons of such wavelength the internal energy of the precursor molecule can build up slowly, thus increasing our sensitivity to the lower energy fragmentation channels. The irradiation time was controlled by a shutter outside the main vacuum chamber and set to 0.3 s, thus allowing three laser pulses. Finally, an extraction pulse sent the photoproducts into the TOF-MS for detection. The final mass spectra were then created by averaging seventy of the previously described cycles at a



4.2. Experimental methods

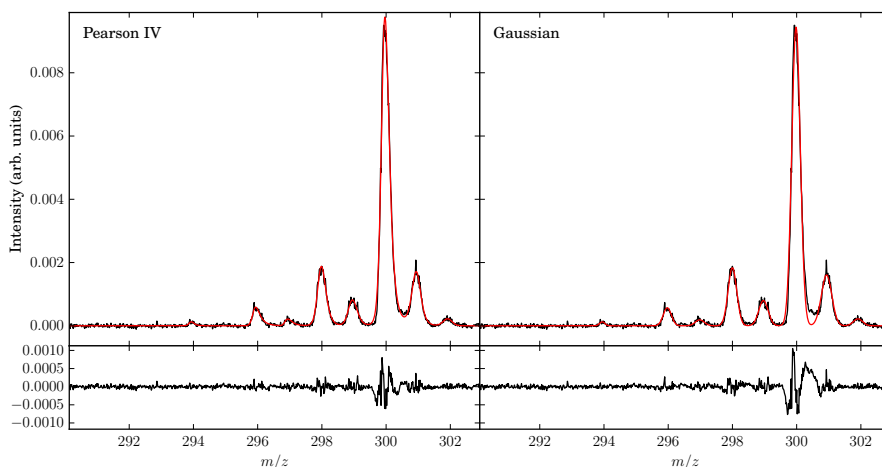


Figure 4.2.: Comparison of a Pearson IV fit (left) to a Gaussian fit (right) on the same coronene mass spectrum. The lower panel shows the difference between the fit and the experimental result.

given laser fluence.

In the case of the largest PAHs studied here (HBC and dicoronylene) the SWIFT pulse was not selective enough to eliminate the isotopic peaks, meaning that in these cases we aimed at reducing the electron-gun induced fragmentation rather than full removal of isotopic peaks. For smaller PAHs, the mass isolation was still not perfect and small levels of fragment and isotopic peaks remained, but did not influence our analysis. Independently of the SWIFT pulse efficiency for each species, the leftover isotopic contribution was arithmetically removed by calculating the ratio of the first isotopic peak to the parent peak and proportionally removing this contribution from the mass spectra. The lowest mass peak observed for a specific PAH cation does not have ^{13}C contributions, so the isotopic ratio is multiplied by the intensity of this peak and the result is removed from the immediately higher mass peak. This was then repeated all the way to the parent and isotopic peak.

The intensity of each mass peak in the spectra was calculated by fitting each individual peak using a Pearson IV function. We chose a Pearson IV function to account for the fact that the mass peaks are not perfectly symmetric, and the additional parameters improve the correspondence between the data and the fit. A comparison of the results of this fit to a Gaussian fit to the same mass spectrum is presented in Fig. 4.2. The decrease in the residuals is noticeable, particularly in the case of high intensity peaks. We estimated the error related to this integration by calculating the root-mean-square over the residual within one standard deviation from the center.

4.3. THEORETICAL METHODS

4.3.1. DENSITY FUNCTIONAL THEORY CALCULATIONS

Density Functional Theory (DFT) calculations were performed to interpret the results of the experiments. Intermediate and transition state structures were investigated with B3LYP/6-31G(d,p) using the quantum chemistry software Gaussian 09 (Frisch et al. 2009). Transition state structures were generally found with the help of the Berny algorithm; for more difficult cases the Synchronous Transit-Guided Quasi-Newton (STQN) method (Peng & Schlegel 1993; Peng et al. 1996) was used. Vibrational analysis was performed to verify the nature of the structure — i.e., no imaginary frequency for intermediate states, and one imaginary frequency for transition states — and to obtain zero-point vibrational energies (ZPEs). Bond dissociation energies (BDEs) were calculated as the difference in the total energy (electronic energy and ZPE) between products and reactants.

To evaluate the accuracy of our calculations, we compared our results to previous experiments or, when these were not available, to high level calculations on smaller and comparable systems. In the case of naphthalene cation ($C_{10}H_8^+$), barriers for H-hopping reactions calculated at B3LYP/6-31G(d,p) level were found to be overestimated by an average of 0.12 eV and 0.15 eV when compared with more accurate but highly-expensive methods such as CBS-QB3 (Montgomery et al. 2000) and G3 (Baboul et al. 2000; Dyakov et al. 2006). The experimental C–H BDEs for benzene (C_6H_6) and for the two different C–H bonds in naphthalene ($C_{10}H_8$) are 4.76 eV (Bauschlicher 1998) and 4.87/4.89 eV (Reed & Kass 2000); the values calculated with B3LYP/6-31G(d,p) are 4.80 and 4.80/4.81 eV, with relative errors inferior to 2%. This comparison validates the use of DFT for our systems.

4.3.2. REACTION RATES

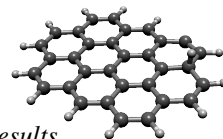
For each reaction studied with DFT the rate was calculated using Rice-Ramsperger-Kassel-Marcus (RRKM) theory (Baer & Hase 1996) in the form

$$k(E) = \frac{W^*(E - E_0)}{h\rho(E)}, \quad (4.1)$$

where h is the Planck constant, W^* is the sum of states of the transition state of the reaction, ρ is the density of states of the reactant and E_0 is the energy barrier of the reaction, calculated with DFT. Both the sum of states and density of states were calculated from the DFT normal modes using the densum program from the MULTIWELL suite (Barker et al. 2017; Barker 2001). The entropy of activation at $T = 1000$ K (ΔS_{1000}) was also calculated for each reaction using

$$\Delta S = k \ln \left(\frac{\Pi\Phi_i^*}{\Pi\Phi_i} \right) + \frac{E^* - E}{T}, \quad (4.2)$$

where E and E^* are the energy of the parent molecule and the transition state, respectively, while $\Pi\Phi_i$ and $\Pi\Phi_i^*$ are the partition functions for the same structures, with $\Phi_i = 1/(1 - \exp(h\nu_i/kT))$ and ν_i are the vibrational frequencies.



4.3.3. MONTE-CARLO SIMULATIONS

In order to model the dehydrogenation process, we have developed a Monte-Carlo code that considers the different hydrogen hopping and fragmentation channels. The rates for these reactions are molecule dependent and calculated using the methods described in the two previous sections. The possible reactions (aromatic H-loss, aromatic H₂-loss, formation of an aliphatic group, hydrogen hopping to a tertiary¹ carbon or emission of an IR photon, in the case of the initial structure) are weighted according to their degeneracies, e.g. in the base case of coronene, aromatic H-loss can happen from twelve different positions. The molecular structure of the unperturbed PAH (as in Fig. 4.1) is given as the initial configuration when running the Monte-Carlo simulations. The time-step is adjusted, taking a tenth of the reciprocal of the sum of all the rates, so that there is 90% chance of nothing happening during each time-step. The weighted rates are converted into a probability by using,

$$p_i = 1 - \exp(-k_i \Delta t), \quad (4.3)$$

where p_i and k_i are, respectively, the probability and the rate of the i -th reaction and Δt is the time-step. The outcome of the model is randomly determined while the structure, its internal energy and the time are updated after each event.

The code can be run in two different settings. In one, the initial internal energy of the molecule is set and left to evolve for a fixed amount of time in order to determine the AE of the fragments and the main dissociation channels involved. In the second setting, the code simulates the experimental conditions in our set-up. In this variation, an additional photon absorption rate is included, based on the cross-sections derived by Mallocci et al. (2007) and the laser fluence. Photon absorption is limited to the first 2 ns, as per the pulse duration. Given the 10 Hz repetition rate of the laser, the molecule is left to evolve for 0.1 s before the next photon absorption phase. In this manner, the three pulses are simulated and the molecule is permitted to evolve for one additional second in order to account for the time between the last pulse and the extraction into the TOF. In this last setting, the partial overlap of the ion-cloud with the laser beam has been included by adding the possibility (ranging from 20 to 40%) that in a given pulse the molecule will not be able to absorb photons, as it stays outside the beam area. In both formats, the simulation is run for 2500 independent trials per data point (internal energy or laser fluence, respectively) in order to have proper statistics.

4.4. RESULTS

In the next subsections we describe the results of our work. Detailed experimental results for each molecule are summarized in Sect.4.4.1. The results of DFT calculations, in particular the barriers for different channels for H- and H₂-loss are presented for a subgroup of the studied molecules in Sect. 4.4.2. Finally, in Sect. 4.4.3 we present the results of the Monte-Carlo simulations applied to three molecules of our sample

¹In this chapter we use the adjective tertiary to describe edge carbon atoms bridging two rings.

IV. Photoinduced PAH dehydrogenation

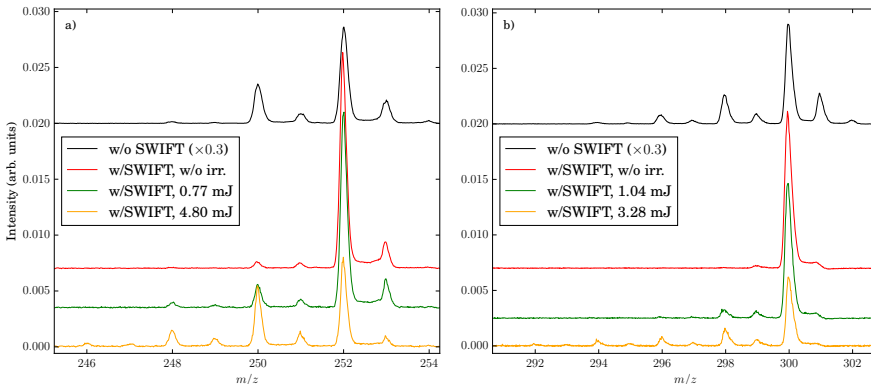


Figure 4.3.: Comparison of the mass spectra of perylene (left) and coronene (right) for different experimental conditions. In black is the spectrum before the SWIFT pulse and without irradiation, which shows electron induced fragmentation (intensity is scaled by 0.3). In red is the SWIFTed and non-irradiated mass spectrum. The green and yellow traces show the mass spectra, after SWIFT pulse and irradiation, for representative low and high laser energy, respectively.

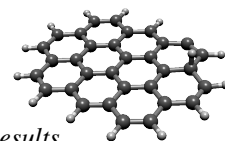
— perylene, coronene and ovalene — discussing their limitations and applicability to the experimental results of our sample.

4.4.1. EXPERIMENTS

Figure 4.3 shows examples of mass spectra for perylene and coronene. A general property found in the fragmentation pattern of PAHs studied here is that even mass peaks are enhanced with respect to the preceding odd peak, as noted in previous work (Ekern et al. 1998; Zhen et al. 2014; West et al. 2014). Figure 4.3 shows also how the odd-to-even ratio in perylene (left panel) increases both as the dehydrogenation moves along and as the laser fluence is increased. For coronene (right panel), this ratio appears to be constant, independently of the hydrogenation state. A general result of our study is that the variation of the odd-to-even ratio with dehydrogenation (1H/2H, 3H/4H etc.) is related to the edge structure of the PAH molecule. We also find that the size of the molecule plays an important role in determining the odd-to-even ratio; large ($N_C \geq 32$) molecules show a significant decrease in the odd to even hydrogen ratio at all hydrogenation states. Eventually, the size effect ends up washing away the differences arising from the edge structure.

In all our experiments the level of dehydrogenation seems to converge at high laser fluence, with the particular value depending on the molecule. We ascribe such behavior to a partial overlap between the laser beam and the ion cloud, which prevents part of the ions to dissociate. This is further supported by the fact that not only the parent molecule fragmentation stabilizes, but also the fragments themselves do not vary in intensity after that point.

Figure 4.4 shows breakdown diagrams as function of laser fluence for molecules



4.4. Results

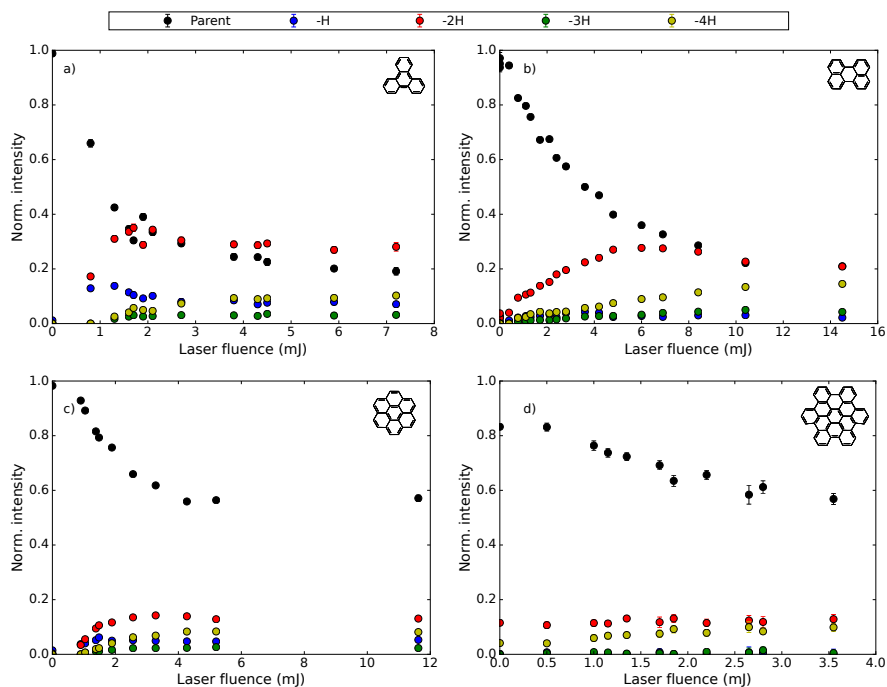


Figure 4.4.: Normalized intensity for the first 4H losses in PAHs with a single type of peripheral hydrogens. (a) Triphenylene ($C_{18}H_{12}^+$), with only quatero hydrogens connected by bay regions; (b) Perylene ($C_{20}H_{12}^+$), with only trio hydrogens, also connected by bay regions; (c) Coronene ($C_{24}H_{12}^+$), with only duo hydrogens connected through tertiary carbons; (d) Hexabenzocoronene ($C_{42}H_{18}^+$), containing only trio hydrogens connected by bay regions. In black is shown the intensity of the corresponding parent molecule, while in blue, red, green and yellow are displayed the fragments corresponding to one, two, three and four hydrogen losses respectively.

containing a single type of edge hydrogen. Edge structure appears to drive the changes observed in the different odd and even peak intensities in the case of small molecules ($N_C \leq 32$). Triphenylene is the smallest molecule considered in our sample (TPH, $C_{18}H_{12}^+$) and contains only quatero hydrogens. Only losses up to four hydrogen atoms are detected as observed by Ekern et al. (1998). Figure 4.4a shows that, while at low laser fluence H-loss and 2H-loss have a similar intensity, the 2H-loss mass peak clearly dominates at 2 mJ. A similar pattern is observed for 3H-loss and 4H-loss, although the laser fluence at which 4H-loss dominates is between 3 and 4 mJ, where H-loss and 4H-loss have almost the same intensity.

Perylene (Pery, $C_{20}H_{12}^+$; Fig. 4.4b) has only trio hydrogens and up to six hydrogen losses are detected in our experiments, two less than what was observed by Ekern et al. (1998). The odd to even ratio in successive H-losses of perylene increases as the dehydrogenation progresses. The 2H-loss mass peak is much more prominent than that for H-loss. Additionally, both the H-loss and 3H-loss intensities are nearly the

IV. Photoinduced PAH dehydrogenation

same starting at 4 mJ, while for triphenylene both intensities remain different along the whole laser fluence range. Furthermore the 4H-loss channel overcomes the H-loss channel early on, and the ratio of -3H/-4H fragments is higher than the -H/-2H fragment ratio.

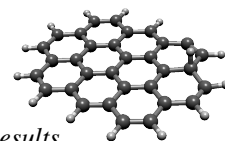
In coronene (Coro, $C_{24}H_{12}^+$; Fig. 4.4c) the fragmentation pattern resembles that of triphenylene. Coronene has only duo hydrogens and a maximum of eight hydrogen atoms are lost within the range of laser fluence explored here. Ekern et al. (1998) noted that coronene reaches full dehydrogenation under their experimental conditions. In our experiments we find that, at laser fluence ≤ 1 mJ, the H-loss and 2H-loss channels have similar intensities. As the laser fluence increases, the 2H-loss mass peak quickly dominates over the H-loss. Additionally, H- and 3H-loss peak intensities are present at all fluences. Unlike in triphenylene, 4H-loss eventually surpasses the H-loss channel at around 3 mJ. Odd-to-even ratios -H/-2H and -3H/-4H remain similar to each other.

HBC ($C_{42}H_{18}^+$; Fig. 4.4d), as perylene, contains only trio hydrogens and it is significantly larger than the molecules considered up to here. The dehydrogenation of HBC has been reported by Zhen et al. (2014); they found the same qualitative behavior observed here for perylene – the further the dehydrogenation progresses, the larger the increase on the successive odd-to-even ratio. However, such behavior is less pronounced than what we find in perylene and becomes noticeable as HBC approaches complete dehydrogenation. One clear difference for HBC with respect to the previous molecules is that the odd hydrogen loss channels are almost non-existent. While the 2H-loss intensity appears constant, it must be noted that in this case the SWIFT isolation was the least efficient, with a large amount of electron impact fragments remaining from the beginning.

PAHs with multiple edge structures (Fig. 4.5) show a mixed behaviour, corresponding to that of the edge structures present. The main factor driving the odd-to-even ratio is still related to the molecular size. Rubicene (Rub, $C_{26}H_{14}^+$; Fig. 4.5a) is the smallest molecule in our sample with a mixture of peripheral hydrogen types, in this case trios and quartos. Additionally, it has pentagonal rings along with the more typical hexagons. We detect losses of up to 8 hydrogen atoms, although the decrease of intensity of the parent peak is much more pronounced than that observed for coronene. As was the case for perylene, the H- and 3H-loss intensities are nearly constant for all laser fluences, although with a lower intensity. At laser fluences below 3 mJ the odd-to-even ratios for -H/-2H and -3H/-4H behave similarly to those observed for perylene. This situation changes at the high end of the fluence range, with the fragmentation pattern showing a closer resemblance to that of coronene, with both ratios having nearly the same values.

Periflanthene (PF, $C_{32}H_{16}^+$; Fig. 4.5b) has a combination of duo and quarto hydrogens and, as rubicene, contains two pentagonal rings in its structure. Up to twelve hydrogen losses are observed. The intensity behaviour with laser fluence qualitatively resembles that of coronene, although odd hydrogen losses are lower in intensity. Also the 4H-loss channel overcomes the H-loss channel at a much lower laser fluence.

TBP ($C_{32}H_{16}^+$; Fig. 4.5c) has mostly duo hydrogens, but there are two trio structures as well, with a mixture of bay regions and tertiary carbons as the connectors. Overall, the dissociation pattern is close to that of periflanthene, displaying the same



4.4. Results

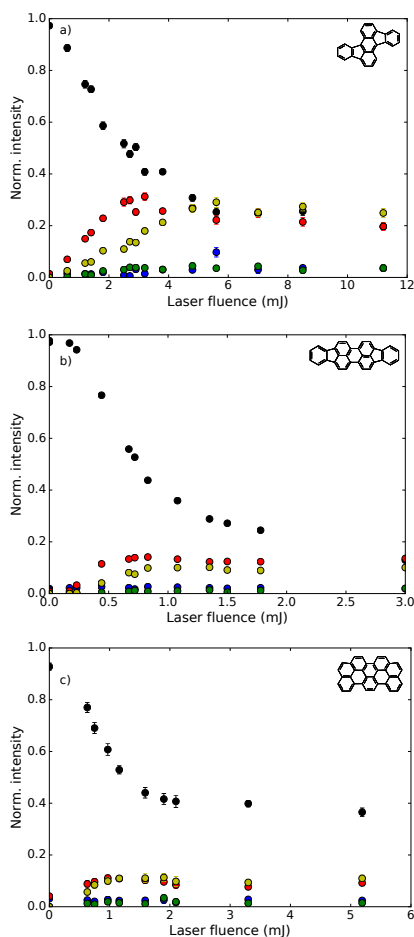


Figure 4.5.: Normalized intensity for the first 4H losses in PAHs with multiple types of peripheral hydrogens. The colors follow the same scheme as Fig. 4.4. (a) Rubicene ($C_{26}H_{14}^+$), with trio and quarto hydrogens connected by bay regions; (b) Periflanthene ($C_{32}H_{16}^+$), with trio and quarto hydrogens, also connected by bay regions; (c) TBP ($C_{34}H_{16}^+$), with duo and quarto hydrogens connected through tertiary carbons and bay regions.

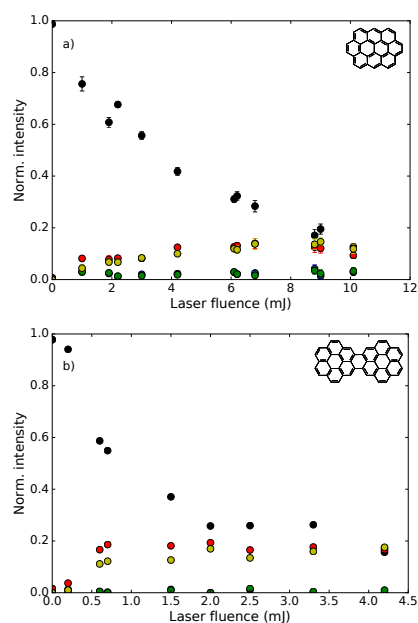


Figure 4.6.: Normalized intensity for the first 4H losses as function of the laser fluence in PAHs with duo and solo hydrogens. The colors follow the same scheme as Fig. 4.4. (a) Ovalene ($C_{32}H_{14}^+$); (b) Dicoronylene ($C_{48}H_{22}^+$), which has two bay regions.

IV. Photoinduced PAH dehydrogenation

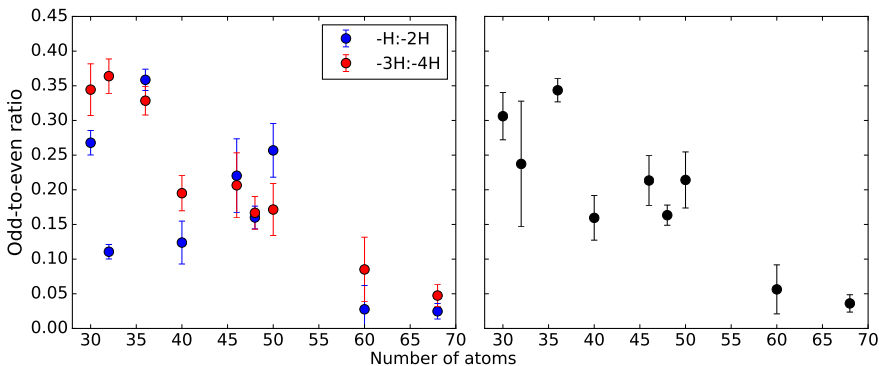
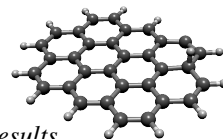


Figure 4.7.: Average odd-to-even ratio (up to 4H losses are considered) for all PAHs studied here as a function of their size in terms of the total number of atoms. The left panel details the variations for progressive dehydrogenation steps (-H/-2H and -3H/-4H) within each PAH. The right panel shows the average of both odd-to-even ratios — i.e., $(-H/-2H + -3H/-4H)/2$.

low intensity for the odd hydrogen losses. The most noticeable difference stems from the fact that 2H- and 4H-loss channel intensities are nearly identical for most of the laser fluence range, a characteristic observed at high laser fluence in rubicene, HBC and, to a lesser extent, in perylene.

Ovalene (Ova, $C_{32}H_{14}^+$; Fig. 4.6a) has a similar behavior as TBP (a molecule with the same size but a less compact structure) although the fragmentation of the parent progresses much further. Ovalene has mainly duo hydrogens but also two solo hydrogens and loses up to twelve hydrogen atoms. The odd hydrogen loss channels are, as for TBP, lower than what has been observed for other molecules, resulting in constant odd-to-even ratios as dehydrogenation progresses. The largest molecule in our sample, dicoronylene (DC, $C_{48}H_{22}^+$; Fig. 4.6b), is composed of mostly duo hydrogens with four solos connected by bay regions. This makes it similar to ovalene in terms of the proportion of edge structures. However, the odd hydrogen fragments are effectively zero, as in HBC, the only other molecule in our sample with more than 40 C-atoms.

In summary, variations in the odd-to-even ratio as the hydrogenation level of the molecule decreases appear to correlate with the number of trios for small molecules (Fig. 4.7, left panel), with the largest difference by far observed in the fragmentation pattern of perylene. Molecules with no trios, on the other hand, show a nearly equal -H/-2H and -3H/-4H ratios. However, as the size increases, the intensity of peaks corresponding to odd hydrogen fragment becomes progressively lower and the difference in successive odd-to-even ratios becomes less pronounced, as can be seen from the average ratios (Fig. 4.7, right panel). This is particularly evident as the molecules approach 50 C-atoms, for which the odd H products are barely detected. The effect of trios and the decrease in the intensity of odd peaks with increased molecular size are explored next using a combination of DFT calculations and Monte-Carlo simulations.



4.4.2. DEHYDROGENATION CHANNELS AND ISOMERIZATION

We investigated the possible dehydrogenation channels for the PAH cations studied experimentally by calculating a) bond dissociation energies (BDE) for H cleavages at different sites and b) transition and intermediate states involved in H₂ formation as function of dehydrogenation. Calculations show that BDEs for H cleavage are independent of both molecular size and degree of dehydrogenation of the molecule. The edge structure of the molecule, namely if the edge H atoms are alone (solo) or arranged in two, three or four (duo, trio and quarto, respectively, Fig.4.1) affects the dissociation energy. When an edge hydrogen is alone (solo) an average of ~ 4.8 eV are needed to remove it. In a duo group, the removal of the first H-atom (both are equivalent) is comparable to that of a solo H, ~ 4.8 eV. The same energy is required to remove the first hydrogen in trios and quartos if this H occupies an external position in the ring. In the case of the central hydrogens (one for the trio and two for the quarto), the energy required for the bond cleavage is somewhat higher, at ~ 5.0 eV. These results are in agreement with previous theoretical studies (Aihara et al. 1996).

The BDE for the second hydrogen atom in the same ring, independently on whether it belongs to a duo, trio or quarto, needs ~ 3.8 eV when it is next to the first dehydrogenated site. The lower energy with respect to the first hydrogen removal is ascribed to the spin pairing of the adjacent carbons in the nearby site, which creates a triple bond as the lowest energy structure, with a doublet electronic state (West et al. 2014). In trios and quartos, when the second hydrogen is removed from a position not immediately adjacent to the dehydrogenated carbon, the BDE is of the order of 4.0 eV. In this case a σ bond forms between the two dehydrogenated sites, creating a cyclopropenyl unit which stabilizes cationic molecules (Trinquier et al. 2017a). Removal of the third hydrogen in a trio leaves an unpaired electron and thus requires ~ 4.9 eV. The same energy is required in a quarto if the third H loss is non-adjacent to a dehydrogenated site. In the opposite case, it will require again only ~ 3.8 eV. The final hydrogen removal in a quarto is nearly independent of the position and it requires 4.2 eV.

C–H BDEs are determined mostly by the local alteration of the molecular structure near the dehydrogenation site. This results in the invariance of the BDEs as dehydrogenation progresses and in the fact that when a group, e.g. a trio, is half dehydrogenated, removal of H from another group will require 4.8 eV. Small fluctuations of the energies are observed in the presence of bay region. For instance, the BDE of the first C–H bond will require slightly lower energy (0.2 eV) when it is removed within the bay region rather than at other positions. This is due to the release of steric hindrance in the bay region (Rodríguez Castillo et al. 2018).

It is interesting to notice that the different energies for sequential H-loss in the case of trio hydrogens could explain the differences observed in the experiments for small molecules like perylene, but not why such differences apparently disappear as molecular size grows. This observation pushed us to explore other pathways leading to hydrogen loss. Given that calculations for the molecules in the sample show that the barriers for these reaction paths are independent of molecular size and dehydrogenation level, we chose perylene to describe these channels and their representative energy values (Fig. 4.8). Indeed, perylene contains both bay region and single tertiary carbon con-

IV. Photoinduced PAH dehydrogenation

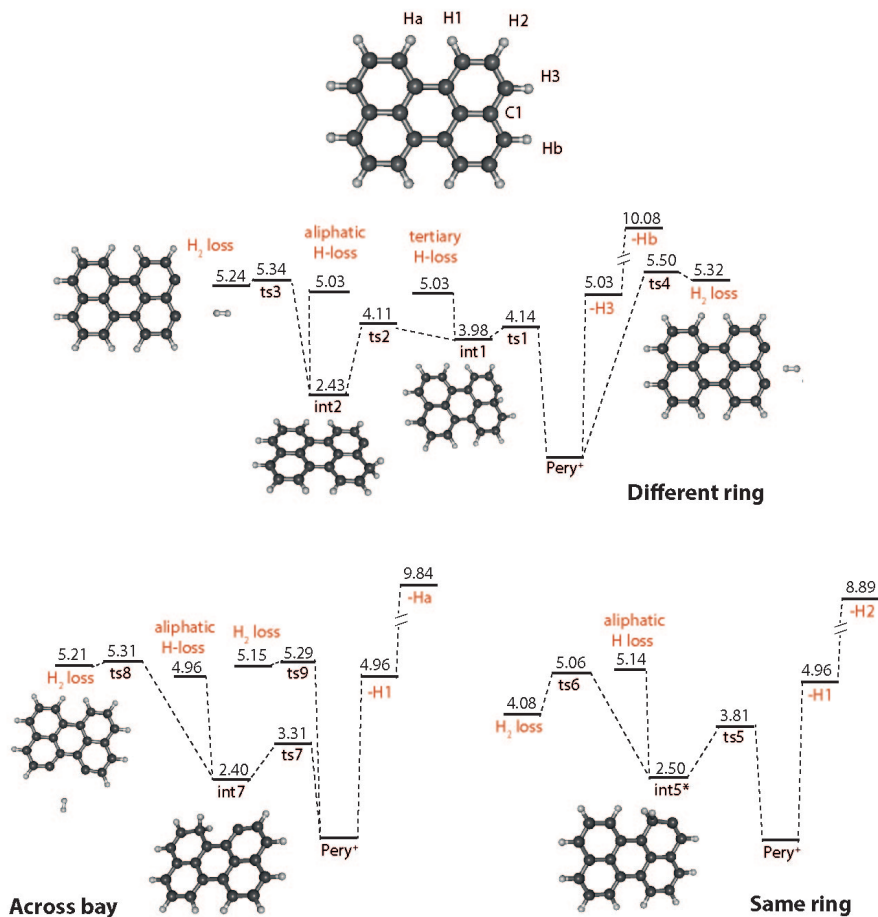
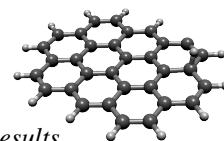


Figure 4.8.: Energy scheme for the perylene cation (top-left), showcasing the different H-hop and H-loss channels available. Isomerization/fragmentation pathways are classified according to whether they involve adjacent rings separated by a single tertiary carbon (top-right), neighboring rings separated by bay regions (bottom-left) or a single ring (bottom-right). Intermediate and transition states are labeled as int and ts, respectively. Loss channels are highlighted in red and all energies are given in eV with respect to that of the perylene cation. The * highlights an intermediate state that can have an energy of 3.20 eV if the aliphatic group is formed by hopping of H1 or H3 towards H2, as opposed to H2 hopping towards H1 (illustrated here) or H3 (see main text).



4.4. Results

nections between rings so all the pathways investigated are present at once.

Direct molecular hydrogen formation (not involving aliphatic C–H bonds) can proceed through the stretching of the C–H bonds in rings separated by a tertiary carbon (C1, Fig. 4.8, top-right) as found for zig-zag edges PAHs (Joblin 2003; Paris et al. 2014; Chen et al. 2015). H₂ formation in this case involves the hydrogens labeled H3 and Hb, with a transition state (ts4) of 5.50 eV. In rings separated by bay regions (Fig. 4.8, bottom-left), C–H stretch of the nearby hydrogen bonds (involving H1 and Ha) can also lead to H₂ formation, in this case with a lower transition state of 5.29 eV (ts9).

Molecular hydrogen formation and single H-loss are also possible once aliphatic C–H bonds are available (in the form of CH₂ groups) via H-hopping. Within the same ring (Fig. 4.8, bottom-right), we have such a situation when a hydrogen atom hops to a nearby occupied site (ts5), creating a CH₂ group adjacent to an empty site (int5). For trios and quartos, the presence of the CH₂ group in the central carbon(s) (that is, H1 or H3 moving into H2) will lead to charge localization. While the transition state involved is the same, the intermediate will be ~0.8 eV higher in energy than for H-hopping in the opposite direction. Once the CH₂ group is formed, a single C–H bond can be severed (requiring an additional 2.64 eV) or H₂ can be formed and released via transition state (ts6) requiring slightly lower energy (2.56 eV with respect to int5). This difference is within the accuracy of our DFT calculations, and for different molecules it can favor H-loss rather than H₂-loss.

H₂ loss can be achieved also in rings separated by tertiary carbons. For perylene (Fig. 4.8, top-left), this can happen when H3 hops to the tertiary carbon C1 (int1) through a transition state. From there either H-loss can proceed directly with an additional 1.05 eV or H3 can jump a second time towards Hb (ts2; requiring 0.13 eV). The resulting isomer (int2) now has an aliphatic group adjacent to an occupied carbon, and H-loss requires an additional 2.60 eV. The resulting energies of the transition and intermediate states for this type of H-hopping are in good agreement with previous results (Paris et al. 2014; Chen et al. 2015). The transition state for H₂-loss (ts3) on the other hand, now needs 2.91 eV above int2 to take place. Finally, an aliphatic group can form in the bay region if H1 jumps to the neighboring hydrogen Ha, without passing through the tertiary carbons (ts7). This configuration (int5) can again lead to H-loss (2.56 eV above int7) or to H₂-loss (via ts8, 2.91 eV above int7).

4.4.3. MONTE-CARLO SIMULATIONS

ASSUMPTIONS AND LIMITATION

Before moving to the results of the Monte-Carlo simulations, it is useful to describe in detail the rates considered and the assumptions made in modeling the reactions involved in the dehydrogenation process. These assumptions stem from the results of DFT calculations for perylene, coronene and ovalene cations and affect the rates included in the simulations. The rates used for the Monte-Carlo simulations are summarized in Tables 4.1 to 4.3. Rates are separated in terms of those involving hydrogen losses, H-roaming within a single ring, jumps to and from tertiary carbons, and hydrogen jumps across bay regions. H-loss can proceed directly from a fully aromatic ring or

IV. Photoinduced PAH dehydrogenation

Table 4.1.: Rates included in Monte-Carlo simulations and parameters for Perylene⁺.

Transition type	E_0 (eV)	ΔE (eV)	ΔS_{1000} (J K ⁻¹ mol ⁻¹)
Hydrogen losses			
Arom. H-loss	4.96	4.96	3.40
Seq. arom. H-loss	3.93	3.93	34.35
Arom. H ₂ -loss	5.50	5.32	35.36
Aliph. H-loss (del.)	2.64	2.64	-4.43
Aliph. H-loss (loc.)	1.93	1.93	20.48
Aliph. H ₂ -loss (del.)	2.56	1.58	27.03
Aliph. H ₂ -loss (loc.)	1.84	0.86	-2.61
Tert. H-loss	1.05	1.05	0.87
Bay H ₂ -loss	5.29	5.15	43.74
H-roaming inside single ring			
Aliph. form. (del.)	3.81	2.50	0.08
Aliph. form. (loc.)	3.81	3.21	0.46
Aliph. to empty (del.)	1.27	-2.50	-8.09
Aliph. to empty (loc.)	0.60	-3.21	-13.14
Aliph. exchange*	1.50	0.00	21.14
Arom. exchange*	2.39	0.00	-3.71
H-roaming to/from tertiary carbon			
Aliph. to tert.*	1.68	1.55	-8.82
Tert. to aliph.*	0.12	-1.55	-12.11
Arom. to tert.*	4.14	3.98	5.40
Tert. to arom.*	0.16	-3.98	-10.62
H-roaming across bay region			
Aliph. form.	3.31	2.40	-11.77
Aliph. to empty	0.91	-2.40	-21.80
Aliph. exchange	1.82	0.00	-18.86
Arom. exchange	1.20	0.00	-11.56

*: E_0 and ΔS depend on hydrogenation level of ring involved.

can have a reduced barrier for rings that have already lost an odd number of hydrogens. Instances where intermediates have a localized charge upon aliphatic formation are indicated in Tables 4.1 and 4.3. In the case of ovalene, the formation of the aliphatic in the position immediately next to a solo site has been labeled as delocalized, while the duos which are non-contiguous to the solo have been labeled as “far” in Table 4.3. This localization clearly will affect the rates of both the aliphatic H-loss and the H₂-loss.

We considered only hydrogen roaming across the edge of the molecules. H-roaming within a single ring includes reactions that create an aliphatic CH₂ group, with a hy-

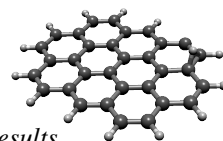


Table 4.2.: Rates included in Monte-Carlo simulations and parameters for Coronene⁺.

Transition type	E_0 (eV)	ΔE (eV)	ΔS_{1000} (J K ⁻¹ mol ⁻¹)
Hydrogen losses			
Arom. H-loss	4.86	4.86	-6.70
Seq. arom. H-loss	3.84	3.84	46.56
Arom. H ₂ -loss	5.42	5.23	24.17
Aliph. H-loss	2.49	2.49	38.80
Aliph. H ₂ -loss	2.59	1.76	22.74
Tert. H-loss	1.78	1.78	14.64
H-roaming inside single ring			
Aliph. formation	3.18	2.36	-18.82
Aliph. to empty	0.82	-2.36	-11.82
Aliph. exchange	0.79	0.00	-14.30
Arom. exchange	2.71	0.00	12.07
H-roaming to/from tertiary			
Aliph. to tert.*	1.15	0.66	-12.44
Tert. to aliph.*	0.49	-0.66	-9.99
Arom. to tert.*	3.57	3.07	-17.40
Tert. to arom.*	0.50	-3.07	-7.83

*: E_0 and ΔS depend on hydrogenation level of ring involved.

drogen hopping to a nearby occupied site, and its reverse. Aliphatic exchange refers to one of the hydrogens from a CH₂ group moving into a nearby carbon already occupied by a hydrogen atom. The aromatic exchange corresponds to hydrogen atoms jumping to unoccupied neighboring carbon atoms. The exchange reactions within the same ring are affected by the number of empty sites in the ring in question. For instance, in the case of perylene, the aromatic exchange in a trio with two unoccupied sites has $E_0 = 3.30$ eV, while listed in Table 4.1 is the value for aromatic exchange when only one site is unoccupied and we have $E_0 = 2.39$ eV.

Hydrogen shifts to or from tertiary carbons also exhibit a change in the barriers depending on the hydrogenation level of the ring involved in the shift. This is especially noticeable for shifts involving aromatic units. Additionally, hydrogen jumps from tertiary carbons are the only reactions found here that are affected by the edge structure in question. For instance, in the case of ovalene, H-hopping into an occupied solo requires $E_0 = 0.17$ eV, while the same reaction into an occupied duo has $E_0 = 0.52$ eV, which has a significant effect in the rate (Table 4.3).

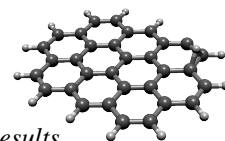
Our DFT calculations show that the barriers for even and odd H-loss and H₂-loss are insensitive to the degree of dehydrogenation. However, dehydrogenation affects the energy barriers and ΔS of H-roaming reactions, especially when H is moving along

IV. Photoinduced PAH dehydrogenation

Table 4.3.: Rates included in Monte-Carlo simulations and parameters for Ovalene⁺.

Transition type	E_0 (eV)	ΔE (eV)	ΔS_{1000} (J K ⁻¹ mol ⁻¹)
Hydrogen losses			
Arom. H-loss (solo)	4.82	4.82	15.58
Arom. H-loss (duo)	4.84	4.84	3.93
Seq. arom. H-loss	3.83	3.83	16.71
Arom. H ₂ -loss	5.26	5.15	35.43
Aliph. H-loss (solo)	2.61	2.61	-2.53
Aliph. H-loss (duo; loc.)	1.92	1.92	-8.41
Aliph. H-loss (duo; del.)	2.23	2.23	-7.36
Aliph. H-loss (duo; far)	2.15	2.15	13.69
Aliph. H ₂ -loss (solo)	3.23	3.03	23.88
Aliph. H ₂ -loss (duo; loc.)	1.99	1.18	12.83
Aliph. H ₂ -loss (duo; del.)	3.01	1.45	30.02
Aliph. H ₂ -loss (duo; far)	2.22	1.39	15.28
Tert. H-loss	1.49	1.49	-6.97
H-roaming inside single ring			
Aliph. formation (loc.)	3.60	2.92	0.69
Aliph. to empty (loc.)	0.68	-2.92	-11.25
Aliph. formation (del.)	3.57	2.65	1.07
Aliph. to empty (del.)	0.92	-2.65	-9.82
Aliph. formation (far)	3.65	2.71	0.29
Aliph. to empty (far)	0.94	-2.71	-9.95
Aliph. exchange	0.90	0.00	-13.54
Arom. exchange	2.70	0.00	7.11
H-roaming to/from tertiary			
Aliph. (solo) to tert.	1.65	1.48	-12.57
Tert. to aliph. (solo)	0.17	-1.48	-11.70
Arom. (solo) to tert.	3.98	3.75	-1.40
Tert. to arom. (solo)	0.23	-3.75	-10.22
Aliph. (duo) to tert.*	1.12	0.60	-11.78
Tert. to aliph. (duo)*	0.52	-0.60	-10.64
Arom. (duo) to tert.*	4.07	3.36	2.53
Tert. to arom. (duo)*	0.71	-3.36	-5.25

*: E_0 and ΔS depend on hydrogenation level of ring involved.



4.4. Results

the edge from one ring to the next through a tertiary carbon in the three molecules considered. In all of the other cases the fluctuations are a few percent, thus within the accuracy of the calculated barriers. Hence we consider all the rates, except the H-roaming across different rings, to be independent of the hydrogen coverage of the molecule.

Additionally, even though H-shifts are known to differ in energy as the distance between the CH_2 and the radical site changes (Trinquier et al. 2017a), we decided to consider single rates for hydrogen shifts of similar nature. The energy differences found by Trinquier et al. (2017a) in the case of neutral coronene are up to 0.4 eV, which should not significantly affect these rates.

Rearrangements of the carbon skeleton, including formation of ethynyl and vinyl groups, have recently been studied (Bauschlicher & Ricca 2014; Bouwman et al. 2016; Trinquier et al. 2017b) in the context of PAH fragmentation. Since here we focus only on the dehydrogenation process, we calculated as an example the loss of H from coronene after the formation of an ethynyl group. This requires 5.41 eV, while loss of any other hydrogen in the molecule only needs 4.87 eV. Thus these reaction paths were not included in our simulations. Additionally, we tested the importance of ethynyl formation in coronene and found it to be negligible; while ethynyl groups are indeed formed, H-loss is not efficient in such configuration. The reverse reaction quickly will lead to the closure of the ring and dehydrogenation will occur from other structures, without significantly affecting the AEs (see Sect. 4.4.3 for more details). Thus, we have not considered isomerization channels involving the carbon skeleton.

RESULTS

The Monte-Carlo simulations provide detailed insight in the main fragmentation processes but also highlight some discrepancies. While such discrepancies are minor for perylene and coronene, the case of ovalene must be further discussed before diving into the general results. When running the full Monte-Carlo simulations, it became immediately clear that hydrogen roaming to tertiary atoms posed an insurmountable challenge to the understanding of the experimental results. The barriers involved in H-shifts to tertiary atoms (see Table 4.3) imply that the solo sites act as attractors for H-atoms, leading to a fragmentation pattern that cannot be reconciled with our experiments. This issue led us to consider canceling hydrogen shifts to tertiary atoms. Such modification only has a minor effect in simulations involving perylene and coronene, but greatly modifies the case for ovalene. While it was necessary to implement further modifications to reproduce the experiments performed on ovalene (see later), canceling H-roaming to tertiary atoms remained indispensable. Given this, all results presented in this section refer to cases where H-roaming is limited to jumps within a single ring or across bay regions. Simulation results involving the jumps to tertiary carbons are presented in Sect. 4.A.

To validate our Monte-Carlo simulations, we run them under the conditions given by Jochims et al. (1994) in an attempt to reproduce their results. In their experiments, they derive AEs of different fragmentation channels within a 10^{-4} s timescale for perylene and coronene, among other PAHs. For these two PAHs, they determined the AE of

IV. Photoinduced PAH dehydrogenation

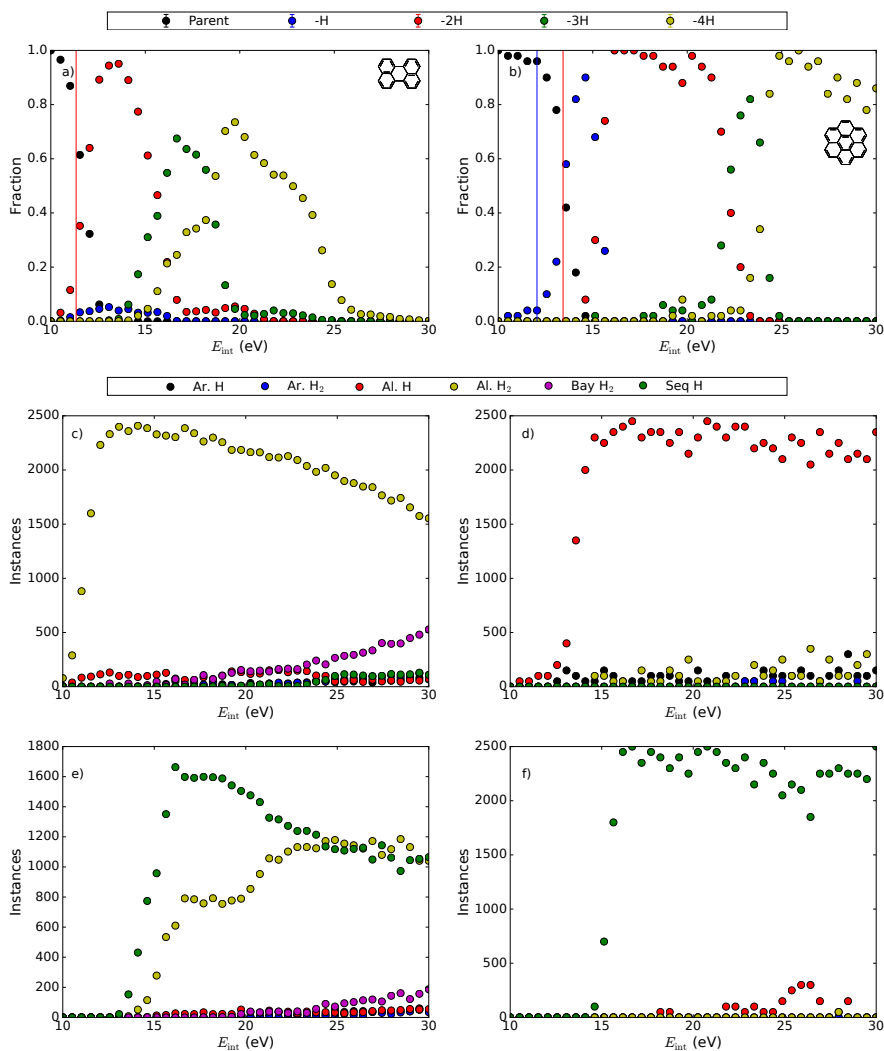
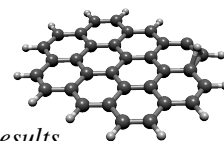


Figure 4.9.: Results of Monte-Carlo simulations of the experiments by Jochims et al. (1994) for the hydrogen loss channels of perylene (a) and coronene (b) after 10^{-4} s. The vertical lines indicate the experimentally derived AE for H-loss (blue) and H₂-loss (red). Panels (c) and (d) show the competition between the different dehydrogenation channels involved in the first fragmentation from perylene and coronene, respectively. Panels (e) and (f) also show the competition between the different channels, but in this case for the second fragmentation step (from perylene after H₂-loss and from coronene after H-loss).



4.4. Results

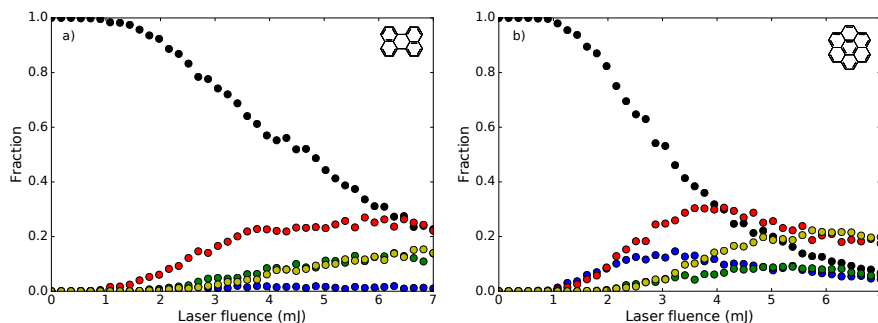


Figure 4.10.: Results of Monte-Carlo simulations of the i-PoP experiments on the fragmentation of perylene (a) and coronene (b) after irradiation with three laser pulses at 656 nm. The colors follow the same scheme as those of the top panels of Fig. 4.9.

the H-loss (not observed in perylene and 12.05 eV for coronene) and H₂-loss channels (11.34 and 13.43 eV for perylene and coronene, respectively). Figure 4.9a and b show the results of the Monte-Carlo simulations up to 30 eV of internal energy for perylene and coronene; the vertical lines mark the AEs derived by Jochims et al. (1994). The energies at which the fragmentation products appear during the simulations show a reasonable agreement with the experiments by Jochims et al. (1994). The differences appear in the H₂/2H-loss channels; in perylene these become relevant at lower energy within our models with respect to the experimental values, while the opposite is true for coronene. The differences in both cases are $\lesssim 1$ eV and the non-detection of the H-loss channel in perylene is well reproduced as well, leading us to conclude that our Monte-Carlo simulation provides an acceptable model to study PAH fragmentation.

Additional channels (3H-loss and 4H-loss) are also observed at higher energies, with perylene undergoing quick full dehydrogenation. As was explained in Sect. 4.3, we focus only in losses of up to four H-atoms since beyond this point other isomerization and fragmentation channels involving the carbon skeleton can become important. In these simulations, we have also investigated the different contributions to the fragmentation channels involved along the dehydrogenation process. Figure 4.9c and d clearly show that the first loss (H₂ for perylene and H for coronene) occurs preferentially from aliphatic sites rather than from aromatic hydrogens. This means that hydrogen shifts play a significant role in PAH dehydrogenation. However, whether the fragmentation proceeds through H- or H₂-loss is molecule dependent. Figure 4.9c additionally shows that H₂-loss across the bay regions becomes a competing channel at high internal energies in perylene. The second loss in coronene (Fig. 4.9f) happens almost exclusively through the sequential hydrogen loss — i.e. the lone hydrogen in the ring that has already lost a hydrogen atom. The same fragmentation channel dominates the second loss in perylene (Fig. 4.9e) in the beginning, due to the fact that a hydrogen atom crossing the bay region into an empty site is a very fast, almost barrierless reaction (Table 4.1). This leads to a significant fraction of isomers with two H-atoms in two trios, leading in turn to four potential hydrogen losses with a reduced barrier. However, as the internal

IV. Photoinduced PAH dehydrogenation

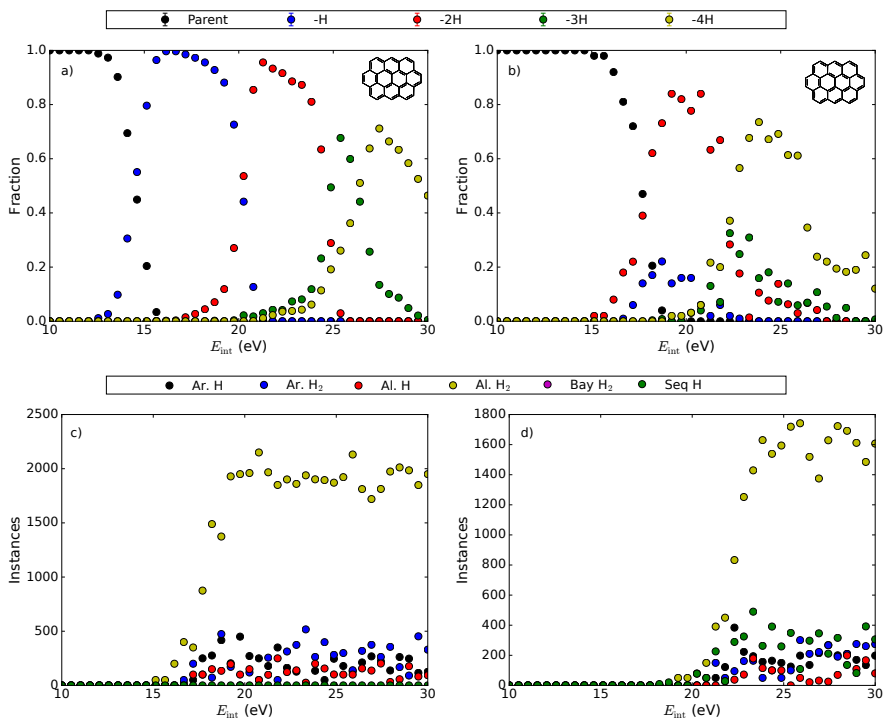
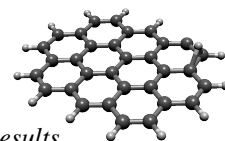


Figure 4.11.: Results of Monte-Carlo simulations for ovalene. Panel (a) shows the simulation considering the barriers as per DFT calculations (including site variations; see Table 4.3), while panel (b) shows the results once the aliphatic loss barriers are set to the values from coronene. Panels (c) and (d) show the channel competition for the results shown in panel (b), with (c) showing the competition for the first fragmentation and (d) for the second fragmentation (from ovalene after H_2 -loss).

energy increases, the competition with the formation of a second aliphatic group and the loss of another H_2 unit becomes relevant and both become equally likely.

We next applied the Monte-Carlo simulations to study PAH behaviour under the conditions of our own experiments with i-PoP. The internal energy is now able to increase as the molecule absorbs photons during the simulated laser pulses. Figure 4.10a and b shows the results for both perylene and coronene, respectively. While differences remain, the qualitative behavior of the simulations provides a good match to the differences observed experimentally (Fig. 4.5b and c). In the case of perylene, we observe that the ratio of odd and even H-losses does increase as dehydrogenation progresses. However, the 3H:4H ratio derived experimentally is not as large at high laser fluence as the one obtained from the simulations. Coronene provides a closer match to the experimental data, with the H:2H and 3H:4H ratios reaching roughly the same values, although the fluence values at which the channels appear do not match exactly.

AEs of the dehydrogenation channels for ovalene have not been determined experi-



4.4. Results

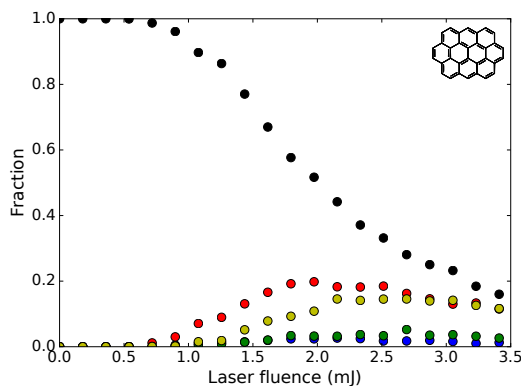


Figure 4.12.: Results of Monte-Carlo simulations of the i-PoP experiments on the fragmentation of ovalene after irradiation with three laser pulses at 656 nm, following the simulation parameters used in Fig. 4.11b. The colors follow the same scheme as those of the top panels of Fig. 4.11.

mentally. Still, we looked into the fragmentation pattern and how well the simulation reproduces our own experiments. As can be seen in Table 4.3, the various aliphatic losses from the duos have all different activation energies and enthalpies, depending on the position of the aliphatic groups. Figure 4.11a shows the result of the simulation in terms of the internal energy, taking into consideration all these differences in the aliphatic losses. Comparison with the same simulation but for coronene (Fig.4.9a) suggests that this behaviour with internal energy will not reproduce the experimental results. We have tested a set of possible solutions, considering all the aliphatic losses with the same parameters, whether they correspond to localized, delocalized or to the far-away carbons, but to no avail. In all these cases, the fragmentation pattern leads to different ratios of odd to even losses as dehydrogenation progresses or to the ratio being about twice as large as the experimental results. Due to the similarity of edge structure in coronene and ovalene, we explored the possibility to set the energy barriers for aliphatic formation and losses in ovalene as in coronene, while keeping the entropy of formation corresponding to the delocalized aliphatic intermediate state of ovalene. The result is shown in Fig. 4.11b; the fragmentation is now occurring in steps of two, with a small fraction of the molecules retaining 13 or 11 hydrogen atoms (1H or 3H loss). Given that this setting reproduces more closely the experimental results, we will present the results of this simulation, and discuss the implications of our choice in the following section.

In ovalene, as in perylene, the dominant loss channel is aliphatic H_2 -loss (Fig. 4.11c), although a variety of other channels also contribute to a smaller extent. However, unlike perylene, ovalene has a compact structure, without bay regions, which prevents the exchange of hydrogens between different rings after the first loss. This leads to the second loss (from ovalene after H_2 -loss) being nearly identical in nature to the first one (Fig. 4.11d). The results of the Monte-Carlo simulation considering the conditions of the experiment is shown in Fig. 4.12. A qualitative comparison with the experimen-

IV. Photoinduced PAH dehydrogenation

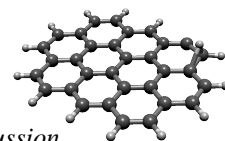
tal results (Fig. 4.6a), shows a remarkably similar behavior, with ovalene missing two hydrogens dominating at low laser fluence, and later ovalene missing four hydrogens reaching a similar level. Along the same lines, the low fraction of fragments with odd hydrogenation is very well reproduced, with both monodehydrogenated ovalene and ovalene with three lost hydrogens having nearly the same fractional abundance. However, it must be noted that the laser fluence range where the fragmentation happens in the Monte-Carlo simulations is much lower than that observed in the experiments.

4.5. DISCUSSION

The experimental results show that the edge structure affects the intensity of successive odd and even hydrogenation losses in small PAHs, producing variation in the even-to-odd peak ratios as dehydrogenation progresses. Larger ($N_C \geq 30$) PAHs behave similarly and show a pronounced decrease in the intensity of the odd peaks, with little to no variations in the odd to even ratios as the dehydrogenation progresses. The edge effect in small PAHs can be understood by directly looking at the energetics of the DFT calculations and is further supported by the results of our Monte-Carlo simulations. In all cases, the formation of aliphatic CH_2 groups during hydrogen hopping is a crucial step in the dehydrogenation, since the vast majority of the losses from PAHs with an even number of hydrogens occurs through aliphatic H- or H_2 -loss. The preferred channel among these two appears to be highly dependent on the particular molecule. While the barriers for both processes tend to be close in energy (usually within the accuracy of DFT calculations), ΔS_{1000} shows larger variations.

The Monte-Carlo simulations for perylene and coronene allow us to understand the effect of edge structure and the different experimental dehydrogenation patterns both molecules exhibit. The absence of the -H fragment in perylene is due to the dominant channel being H_2 -loss from an aliphatic site, while the increased intensity of the -3H fragment with respect to the -4H is explained as the rapid exchange of hydrogens between nearby rings across the bay regions. On the other hand, coronene retains a considerable fraction of fragments with an odd number of hydrogens, although the evens are always more abundant, confirming earlier experiments (Jochims et al. 1994; Joblin 2004). Our simulations show that coronene loses hydrogens sequentially, thus explaining the pattern and the constant odd to even ratios. Aliphatic H-loss dominates the first loss, while the second hydrogen loss proceeds much more rapidly due to the reduced barrier in partially hydrogenated rings.

Using the results for coronene and perylene, we can rationalize the fragmentation patterns observed in the other molecules studied here and look for general trends applicable to PAHs as a whole. In Sect. 4.4.2 we saw that BDEs for H losses in duo and quarto behave similarly thus making the case for the overall fragmentation pattern – enhanced even peaks over odd peaks – observed in triphenylene. Furthermore, the presence of bay regions and the possibility of a fast H hopping across them in this molecule also explains the differences observed between triphenylene and coronene, that is, odd peaks are slightly more intense in the former. The same case can be made for rubicene, where the presence of trios and bay regions in combination with quarto



4.5. Discussion

hydrogens gives rise to its unusual fragmentation pattern. All small PAHs ($N_C < 32$) in our sample show variations in the dehydrogenation behaviour that can be connected to the presence of bay regions and the different edge structures present. The actual strength of odd-to-even ratios are indicative of whether H- or H₂-loss dominates the fragmentation. In our case, the low intensity for the first H-loss in perylene suggests that this is the only molecule which undergoes significant molecular hydrogen formation as part of its fragmentation process, a conclusion also supported by other studies (Jochims et al. 1994).

Figure 4.7 shows that the average odd-to-even ratio correlates with molecular size. Furthermore, the dependence on the edge structure appears to be washed away as the molecular size increases. This is particularly striking in the case of HBC: no variations in odd-to-even ratio are observed as dehydrogenation progresses, although the structure of HBC resembles that of perylene (trios and bay region), where the ratios do change. Such changes have been observed in other experiments involving HBC, although only when the hydrogenation level is much lower than what we currently investigated and with an overall lower degree of variations (Zhen et al. 2014). The difference between perylene and HBC is probably due to a larger degree of competition between aliphatic and bay region H₂-loss. This being the case, the influence of the H-hopping across bay regions would be greatly reduced and sequential H-loss would become a secondary channel until further down the dehydrogenation process.

The inability of our Monte-Carlo simulations to reproduce the experimental results for ovalene when all the possible rates are considered, tells us that there must be issues with the DFT results. Given the structural similarity between coronene and ovalene (both compact molecules dominated by duo edges), it is tempting to speculate that the problem arises when dealing with the only structural difference, namely the presence of solo hydrogens. Hydrogens in solo positions are known to be the most reactive sites in PAHs (Aihara et al. 1996). Our quantum chemistry calculations show that once a H atom has moved from a duo group to the tertiary C between solo and duo (R1 from hereafter), the intermediate state lies quite high in energy (3.7 eV) with respect to the standard ovalene. From there, moving to the solo site (R2) requires only 0.17 eV — almost a barrierless reaction — which makes the solo site the place where the roaming H will end up being. From there, aliphatic H-loss has a lower barrier than H₂-loss and thus dominates. This situation would change if a) the barrier of R2 was higher or b) once on the tertiary C, the H would jump into the carbon skeleton rather than of along the edges. We then recalculated the barrier of R2 using the M06-2X functional, which is known to give more reliable values for barrier height (Zhao & Truhlar 2011), but we found a value 0.21 eV which does not affect the reaction rate. We also calculated the barrier for H-roaming inside the ring, and found that both forward and reverse barriers are comparable to other jumps to tertiary.

Only by using the barriers derived for coronene in the aliphatic formation and loss processes, we were able to produce a qualitative agreement with the experiments for ovalene. In order to explain the observed decrease of the odd-to-even ratio as PAH size increases (Fig. 4.7), the photofragmentation needs to be dominated by H₂-loss, whether from aliphatic sites or bay regions. By looking in particular at the case of HBC, it is possible that the H₂-loss channel in bay regions will become a more competitive

IV. Photoinduced PAH dehydrogenation

Table 4.4.: Summary of first and second loss channel efficiencies in dehydrogenation reactions for PAHs.

Loss channel	$N_C < 32$		$N_C \geq 32$	
	Trio/Bay	Duo/Quarto	Trio/Bay	Duo/Quarto
Aromatic H-loss	✓	✓		
Aromatic H ₂ -loss				
Aliphatic H-loss		✓		
Aliphatic H ₂ -loss	✓		✓✓	✓✓
Bay-region H ₂ -loss			✓✓	

Black and red tick marks correspond to the first and second loss channel, respectively.

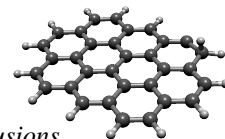
Solo hydrogens can only be lost via aromatic H-loss.

channel — as seen at high E_{int} in perylene. Aromatic H₂-loss, on the other hand, is never observed to be a competitive channel. This is expected due to its high energy barrier (more than 1 eV above most other dissociation channels). A summary of the dominant reactions according to the type of edge structure and PAH size is presented in Table 4.4.

4.6. CONCLUSIONS

In this chapter we combined experiments, theory and modeling to understand the dehydrogenation behaviour, in particular the odd-to-even ratio, of a sample of nine different and representative PAHs up to astronomical sizes $N_C = 48$. The results of the modeling are not only consistent to our own experimental results, but also reproduce reasonably well the observed appearance energies and fragmentation channels observed by Jochims et al. (1994). The Monte-Carlo simulations show two main factors acting on the behaviour of the odd-to-even H-loss pattern observed during PAH dehydrogenation: edge structure and size. The edge structure effects are important in small PAHs and are related to the presence of trios and bay regions, both of which increase the relative intensity of odd H peaks with respect to even peaks as dehydrogenation progresses. As PAH size increases, the odd-to-even peak ratio decreases, effectively reducing the variations due to different edge structures until they become almost unrecognizable for $N_C \geq 32$. The decrease of the odd-to-even ratio with increasing PAH size can clearly be observed in Fig. 4.7, with the largest molecules displaying ratios close to zero. In line with the Monte-Carlo simulations, the lack of odd H peaks can be interpreted considering that in larger molecules aliphatic H₂-loss dominates over aliphatic H-loss.

The loss channels from PAHs with even hydrogenation are all dominated exclusively by aliphatic losses, whether in the form of atomic or molecular hydrogen. Thus, hydrogen hopping along the edge of PAHs is an indispensable ingredient to the dehydrogenation of PAHs and should be taken into account when modeling the photochemistry



4.6. Conclusions

of PAHs in space. This is particularly true when considering H_2 formation on PAHs, given that such a loss from a fully aromatic molecule has a rate limiting barrier at much higher energy than the equivalent process from an aliphatic site.

H-hopping across different rings through a tertiary carbon shows little to no importance in small molecules and was problematic in the case of ovalene, resulting in ratios and fragmentation patterns inconsistent with the experimental results. This begs for a detailed assessment on the capabilities of DFT for studying fragmentation and isomerization processes in large molecules in general and solo containing PAHs in particular.

Our study could not elucidate which properties determine the preference for one loss channel or another. The size dependence observed in our experiments suggests that molecular size might be a crucial parameter in favoring H_2 -loss. Further experiments, particularly in large PAHs with a significant number of solo hydrogens are needed to help elucidate the role of this edge structure in the dehydrogenation process and establish the accuracy of the rates and barriers derived from DFT calculations.

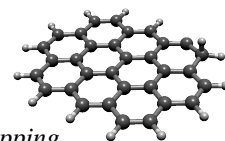
From an astrochemical perspective, this work suggests that molecular hydrogen can be an important by-product of the photodestruction of large, astronomically relevant PAHs. Such connection has been suggested before, but the vast majority of previous studies focused on hydrogen abstraction, which is only relevant in regions where PAHs are found in superhydrogenated states (e.g., where $G_0/n(H)$ is very small, where G_0 is the UV field intensity and $n(H)$ the atomic hydrogen density: Montillaud et al. 2013; Boschman et al. 2015; Andrews et al. 2016). However, in regions where the UV radiation field is low, most of the H is typically already molecular. The current results point to the possibility of H_2 formation at the very edge of PDRs (high $G_0/n(H)$), which is precisely where the transition between molecular and atomic hydrogen occurs. Astronomical models for PAH fragmentation based upon these results will help elucidate whether the fragmentation process can indeed act as an efficient factory for molecular hydrogen.

ACKNOWLEDGMENTS

We thank M.J.A. Witlox and R. Koehler for technical support on i-PoP. Studies of interstellar chemistry at Leiden Observatory are supported through advanced-ERC grant 246976 from the European Research Council, through a grant by the Netherlands Organization for Scientific Research (NWO) as part of the Dutch Astrochemistry Network, and a Spinoza premie. We acknowledge the European Union (EU) and Horizon 2020 funding awarded under the Marie Skłodowska-Curie action to the EUROPAH consortium, grant number 722346. AC acknowledges NWO for a VENI grant (number 639.041.543). JZ acknowledges financial support from the Fundamental Research Funds for the Central Universities and from the National Science Foundation of China (NSFC, grant number 11743004). HL acknowledges NWO for a VICI grant (number 639.043.905). DFT calculations were carried out on the Dutch national e-infrastructure (Cartesius) with the support of SURF Cooperative, under NWO EW projects MP-270-13 and SH-362-15.

4.A. MONTE-CARLO WITH TERTIARY H-HOPPING

Figure 4.13 shows the results of the Monte-Carlo simulations of perylene, coronene and ovalene. In this case all rates have been allowed, including H-hopping to and from tertiary carbons, which were excluded in the main text. Perylene (Fig. 4.13a) shows no noticeable changes with respect to the results with exclusion of the tertiary rates (Fig. 4.9a). Coronene (Fig. 4.13b) displays minor changes in AE for its fragments with respect to the results from Fig. 4.9b, but the overall behavior is not modified. Note that in the present case the match with the AE of Jochims et al. (1994) is better. However, the case of ovalene (Fig. 4.13c) is markedly different from the simulation run with no tertiary jumps (Fig. 4.11a and b). As explained in the main text, this is due to the solo hydrogens acting as attractors for the roaming hydrogens.



4.A. Monte-Carlo with tertiary H-hopping

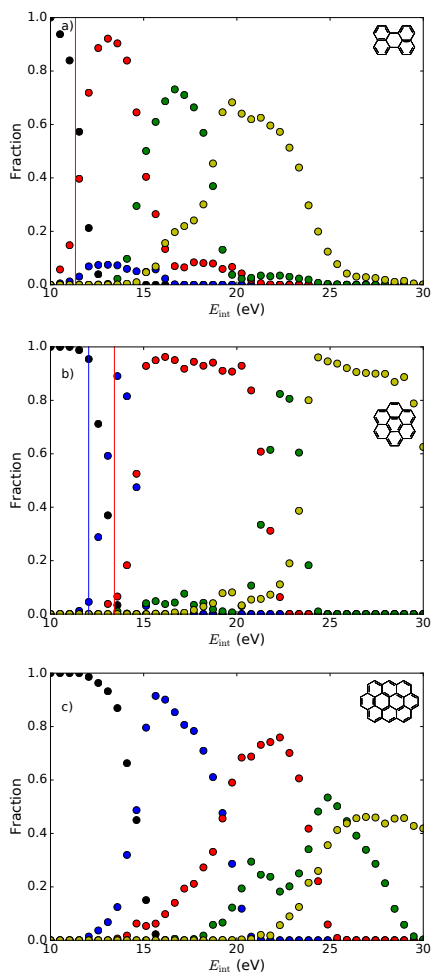
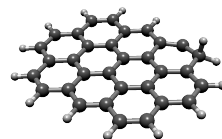


Figure 4.13.: Monte-Carlo results for perylene, coronene and ovalene fragmentation as a function of internal energy. These results take into consideration the possibility of H-hopping involving tertiary carbons. The colors follow the same scheme as those of the top panels of Fig. 4.9.



V

MOLECULAR HYDROGEN FORMATION IN PDRS

The physicochemical conditions of photodissociation regions (PDRs) are largely determined by the influence of far ultraviolet radiation. Far-ultraviolet photons can efficiently dissociate molecular hydrogen, a process that must be balanced at the HI/H_2 interface of the PDR. Given that reactions involving hydrogen atoms in the gas phase are highly inefficient under interstellar conditions, H_2 formation models mostly rely on catalytic reactions on the surface of dust grains. Additionally, molecular hydrogen formation in polycyclic aromatic hydrocarbons (PAHs) through the Eley-Rideal mechanism has been considered as well, although it has been found to have low efficiency in PDR fronts. In a previous work, we have described the possibility of efficient H_2 release from medium to large sized PAHs upon photodissociation, with the exact branching between H/H_2 -loss reactions being molecule dependent. Here we investigate the astrophysical relevance of this process, by using a model for the photofragmentation of PAHs under interstellar conditions. We focus on three PAHs cations (coronene, ovalene and circumcoronene), which represent three possibilities in the branching of atomic and molecular hydrogen losses. We find that, for ovalene (H_2 -loss dominated) the rate coefficient for H_2 formation reaches values of the same order as H_2 formation in dust grains. This result suggests that this hitherto disregarded mechanism can account, at least partly, for the high level of molecular hydrogen formation in dense PDRs.

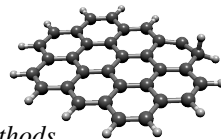
P. Castellanos, A. Candian, H. Andrews, et al. 2018, *Photoinduced PAH dehydrogenation: Molecular hydrogen formation in PDRs*, *Astron. Astrophys.*, in press

5.1. INTRODUCTION

Photodissociation regions (PDRs) correspond to mainly neutral areas in the interstellar medium (ISM) where the physical and chemical conditions are to a large extent determined by the ultraviolet (UV) field (see Hollenbach & Tielens 1997). These include a variety of environments, from the neutral gas surrounding luminous HII regions, reflection nebulae, the galactic warm neutral medium and diffuse clouds, among others. As their name indicates, PDRs are regions where the transition from neutral, atomic gas to its molecular counterpart takes place (Sternberg et al. 2014; Bialy & Sternberg 2016). As such, the balance between formation and photodissociation of the simplest, diatomic molecules is of special interest, particularly considering that chemical reactions in the gas phase are highly unlikely. Given that H_2 is the most abundant interstellar molecule, its formation mechanism is of particular importance (see Wakelam et al. 2017, for a recent review). Most works on the formation of molecular hydrogen focus on two mechanisms. On the one hand, there are Langmuir-Hinshelwood reactions, where two physisorbed H atoms migrate on a dust grain surface and, after reacting, are released as H_2 (e.g., Pirronello et al. 1997; Katz et al. 1999). On the other hand, we have Eley-Rideal mechanisms, where a gas phase hydrogen atom reacts with another, chemisorbed hydrogen and both are desorbed as H_2 (e.g., Duley 1996; Habart et al. 2004). The former process is known to be efficient at low dust temperatures ($T_d \leq 20$ K), while the latter can be effective at higher temperatures, more representative of dense PDRs.

The emission from polycyclic aromatic hydrocarbons (PAHs) dominates the mid-infrared (mid-IR) spectrum of a wide variety of astronomical sources containing dust and gas, including PDRs (Tielens 2013, and reference therein). The peak emission of PAH bands is found to coincide with H_2 emission lines, prompting the suggestion of a link between both species (Habart et al. 2003). This link can be due to H_2 formation via H_2 abstraction from superhydrogenated PAHs (Rauls & Hornekær 2008) or the H_2 -loss from the fragmentation of PAHs (Jochims et al. 1994). The latter mechanism is associated with the general idea of interstellar top-down chemistry with PAHs as precursors. Observations of PDRs have revealed that, as the PAH band intensity decreases, the fullerene (C_{60}) band intensity increases (Berné & Tielens 2012). This suggests that photoprocessing of PAHs leads to their fragmentation and eventual formation of fullerenes among other intermediate species. Furthermore, several small hydrocarbons — such as C_2H , C_3H_2 , C_3H^+ and C_4H — are known to be related to PAH mid-IR emission bands in PDRs, an association that has also been considered indicative of a top-down formation mechanism (Pety et al. 2005; Guzmán et al. 2015; Cuadrado et al. 2015). The formation of small and large hydrocarbon products through top-down photochemistry requires intense UV-fields, which is consistent with the observations of the aforementioned molecules deep within the atomic part of the PDR. However, H_2 formation will be effective in slightly more shielded environments, namely the HI/H_2 transition region.

Habart et al. (2004) used the ratio of rotational to rovibrational H_2 lines to determine the formation rate coefficient ($R(\text{H}_2)$) in dense, hot PDRs. Their estimate yields values of $R(\text{H}_2) \sim 10^{-16} \text{ cm}^3 \text{ s}^{-1}$, almost an order of magnitude higher than the standard



5.2. Methods

value found in diffuse clouds ($3 \times 10^{-17} \text{ cm}^3 \text{ s}^{-1}$ Jura 1975; Gry et al. 2002). The H_2 formation rate in the diffuse ISM is generally well accounted for when considering only grain surface reactions (Hollenbach & Salpeter 1971), but these reactions alone fall short at explaining the situation in dense PDRs. In order to account for this deficiency, reactions involving PAHs have been invoked as alternative mechanisms for H_2 formation. Such a connection is further supported, seeing as there is a clear spatial correlation linking H_2 and PAH emission (Habart et al. 2003). The proposed routes include an Eley-Rideal mechanism analogous to that described for dust, involving the abstraction of molecular hydrogen from superhydrogenated PAHs (Rauls & Hornekær 2008; Mennella et al. 2012), and direct photodissociation of PAHs involving H_2 -loss (Jochims et al. 1994; Ling et al. 1995). The importance of both formation pathways has been investigated using different models for a variety of PDR conditions (e.g., Bron et al. 2014; Boschman et al. 2015; Andrews et al. 2016). These models have established that surface reactions (i.e., Eley-Rideal) on PDR fronts cannot efficiently form H_2 , given that under these conditions superhydrogenated PAHs make up a nearly negligible fraction of the total population. While photodissociation through H_2 -loss is found to be the dominant H_2 formation pathway from PAHs, its rate makes a negligible contribution to the total H_2 formation in PDRs. However, we note that for H_2 -loss from PAHs, all models rely on photodissociation parameters extrapolated from experimental and theoretical work on rather small PAHs (up to 24 C-atoms).

In the previous chapter modeling the experimental dissociation pattern of PAHs, we have determined the barriers and enthalpy change required for H- and H_2 -loss from medium sized PAHs. That study included an analysis on small, previously studied PAHs in order to validate our results against previous work. We found that H-hopping within PAHs is an essential part in the dehydrogenation process, creating an aliphatic-like side group (CH_2), which can lead to the release of atomic or molecular hydrogen. In small PAHs, H-loss is found to be the dominant channel, in accordance with other results found in the literature (Jochims et al. 1994; Ling et al. 1995; Ling & Lifshitz 1998). Large PAHs show the predominant channel to be H_2 -loss, although with the caveat that solo hydrogens can only be lost in atomic form from aromatic positions.

In the present study we utilize our previously calculated rates for coronene and ovalene, and expand our calculations to circumcoronene. In Sect. 5.2 we discuss our model for H_2 formation through photolysis of PAHs. The results are presented in Sect. 5.3 and in Sect. 5.4 we discuss H_2 formation in PDRs and summarize our conclusions.

5.2. METHODS

Density Functional Theory (DFT) calculations on the structures of intermediate and transition states were performed using B3LYP/6-31G(d,p) and the quantum chemistry software Gaussian 09 (Frisch et al. 2009). Transition state structures were in most cases determined with the Berny algorithm, while the Synchronous Transit-Guided Quasi-Newton (STQN) method (Peng & Schlegel 1993; Peng et al. 1996) was used in more complex cases. Reaction rates were calculated using Rice-Ramsperger-Kassel-Marcus (RRKM) theory (Baer & Hase 1996), using the sum of states for the transition state

V. Molecular hydrogen formation in PDRs

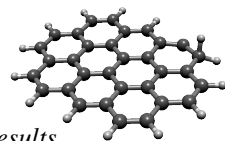
and the density of states for the parent structures. The sum and density of states were calculated using the normal vibrational modes derived from DFT, by means of the densum program from the MULTIWELL suite (Barker et al. 2017; Barker 2001).

The aforementioned methods were used to study the dehydrogenation of a series of PAHs, together with experimental and Monte-Carlo techniques (chapter IV). The results of that work show that the fragmentation process is dominated by formation of “aliphatic” groups due to hydrogen roaming — i.e., the formation of CH_2 groups on the edge of the molecule. From this point on, dehydrogenation can proceed either by atomic or molecular hydrogen loss, in a manner that is molecule dependent. In this work, we will use the results already derived for coronene and ovalene. As mentioned in chapter IV, in order to fit the experimental data of ovalene, the energy barriers for aliphatic H- and H_2 -loss had to be adjusted to match those of coronene, while keeping the values for ΔS_{1000} as derived from the DFT calculations. The original study did not include the circumcoronene cation and experiments on the dehydrogenation of this molecule are currently lacking. However, we have calculated the intermediate structures and transition states involved in the formation of aliphatic groups and the loss of atomic and molecular hydrogen. In order to keep consistency with the previous calculations, the energy barriers for the loss channels in circumcoronene have also been modified to match those of coronene.

We note that coronene, ovalene and circumcoronene all have duo hydrogens and, in the case of ovalene and circumcoronene, solo hydrogens with no bay-regions. Following the conclusions from chapter IV, we have disregarded reactions involving tertiary carbons (an edge carbon bridging two neighboring rings). Aliphatic formation is thus only possible within duos, and aromatic H-loss is the only fragmentation channel available for the solos. The isomerization rates considered in this work involve the rate of formation of an aliphatic group and its reverse. For photodissociation, both aliphatic and aromatic H- and H_2 -losses are calculated. All rates are based on the fully hydrogenated form of the PAH in question, with the exception of aromatic H-loss from a partially hydrogenated duo, for which the parent structure is that of the fully aromatic PAH after a single H-loss. The latter loss rate is considered separately, given that the energy barrier is ~ 1 eV lower than for a full duo.

In order to assess the astronomical relevance of H_2 formation, we implemented our calculated rates into the model for hydrogenation and dehydrogenation of PAHs of Andrews et al. (2016). Their model includes a variety of physical and chemical processes for PAHs in interstellar environments, including ionization, electron recombination, hydrogen attachment, photodissociation (as H- and H_2 -loss) and H_2 formation from superhydrogenated molecules following Eley-Rideal abstraction. The focus of the present work is to investigate H_2 formation through photodissociation on PDRs. Given that the transition from fully hydrogenated PAHs to fully dehydrogenated PAHs (the PDR front) occurs at fairly high values of G_0 (the UV field intensity), processes involving superhydrogenated PAHs — such as Eley-Rideal abstraction — can be disregarded. Under the same considerations, and taking into account that our DFT calculations are focused on cations, we keep electron recombination to a minimum by setting $n_e = 10^{-7} \text{ cm}^{-3}$.

The photodissociation rates considered in the model by Andrews et al. (2016) are



5.3. Results

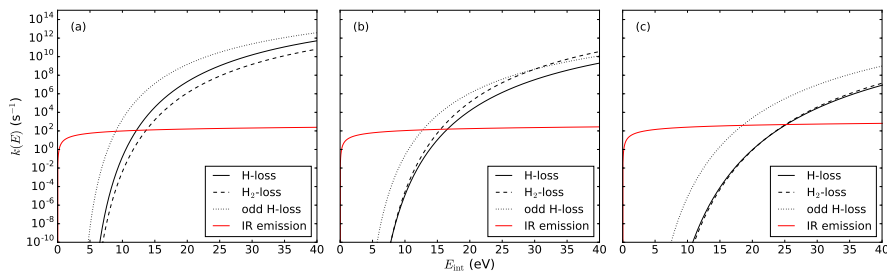


Figure 5.1.: Hydrogen loss rates as a function of internal energy for the coronene (a), ovalene (b) and circumcoronene (c) cations. H- and H₂-loss are considered as from the parent molecule, while odd H-loss refers to hydrogen loss from a partly filled duo.

considered in terms of H- and H₂-loss. Given that in their original formulation the formation of aliphatic groups via hydrogen hopping was not taken into account, the model receives as input a single rate for each loss. In order to work around this issue, we have calculated effective photodissociation rates. For this, the fraction of the time the PAH in question exists with an aliphatic group is calculated using

$$f_{\text{al}}(E) = \frac{k_{\text{al}}(E)}{k_{\text{al}}(E) + k_{\text{al,r}}(E)}, \quad (5.1)$$

where $k_{\text{al}}(E)$ is the aliphatic formation rate as a function of energy, and $k_{\text{al,r}}(E)$ is the rate for the reverse reaction. For both rates the corresponding degeneracies are taken into account — e.g. in fully hydrogenated coronene, the twelve hydrogen atoms can hop towards the neighboring H in the same duo, while for the reverse reaction either of the two hydrogen atoms can hop back into the empty carbon. The time fraction the molecule is in a fully aromatic configuration, on the other hand, will be given by $1 - f_{\text{al}}(E)$. The effective H-loss rate is calculated by multiplying the respective fractions to the corresponding photodissociation rates and adding together the contributions of aliphatic and aromatic losses. The same process is applied to H₂-loss.

5.3. RESULTS

The effective fragmentation rates, as derived from DFT calculations, are shown in Fig. 5.1. The three PAHs selected for this work provide examples of the three types of photofragmentation balance that can be found: H-loss dominated (coronene), H₂-loss dominated (ovalene) and competitive (circumcoronene). While these rates include contributions from aromatic rates, aliphatic losses are in all cases the dominant channel for the respective loss by as much as five orders of magnitude in the relevant energy range. The only exception to this is the odd hydrogen loss, for which the aromatic H-loss dominates in all three molecules. For fragmentation to take place, the dominant loss rate must exceed the IR photon emission rate, which is the case at 12.2, 15.5 and 25.1 eV for coronene, ovalene and circumcoronene, respectively. Considering the 13.6 eV cutoff

V. Molecular hydrogen formation in PDRs

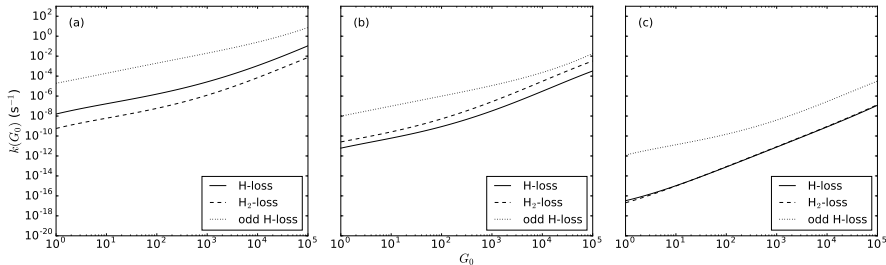


Figure 5.2.: Hydrogen loss rates as a function of G_0 for the coronene (a), ovalene (b) and circumcoronene (c) cations. H- and H_2 -loss are considered as from the parent molecule, while odd H-loss refers to the loss from a partly filled duo.

for UV photons in the ISM, this means that, while coronene can be fragmented by single photon absorption. Dehydrogenation of other PAHs will be dominated by multiple photon absorption.

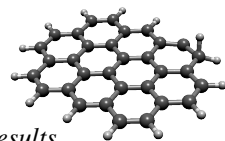
Figure 5.2 shows the fragmentation rates as a function of G_0 . These were calculated following the procedure described by Andrews et al. (2016), taking into account the temperature probability function following Bakes et al. (2001, and references therein). Such a model considers as well the possibility of multiphoton events which, as mentioned, are needed in order to fragment larger PAHs. The effects of multiple photon absorption can be observed in Fig. 5.2, as deviations from a linear behavior are observed at $G_0 = 10^3$ in coronene, but earlier on for ovalene and circumcoronene. The three variations on the H-/ H_2 -loss balance described before are still evident here, with odd H-losses dominating in cases where it is available. The effects of degeneracy are minor in all three PAHs, with variations due to hydrogenation level remaining below an order of magnitude in all cases.

The fragmentation of the PAHs studied here follows an established pattern under interstellar conditions. When hydrogen within duos are part of the molecule in question, these are the preferred dehydrogenation sites in all cases. Even hydrogen losses can proceed via aliphatic H- or H_2 -loss according to the characteristics of the PAH under consideration, as explained before. Odd hydrogen losses always occur via aromatic C–H bond cleavage with a reduced barrier. Considering that the rates involved in H-loss from the solos are exclusively aromatic and do not have the reduced barrier of partly hydrogenated duos, these are the last hydrogens to be lost in the molecule.

We have calculated the efficiency of H_2 formation (ξ_{H_2}) considering the fragmentation and hydrogen addition rates as a function of the hydrogenation state (i) using,

$$\xi_{H_2}(Z) = \sum_i \frac{2k_{H_2}(Z, i)f(Z, i)}{\kappa_{\text{add}}n(\text{H})}, \quad (5.2)$$

where κ_{add} is the hydrogen addition rate coefficient, $f(i)$ corresponds to the fraction of the PAH with hydrogenation state i and $n(\text{H})$ is the atomic hydrogen density. For cations, we use $\kappa_{\text{add}} = 1.4 \times 10^{-10} \text{ cm}^3 \text{ s}^{-1}$ following Andrews et al. (2016). Given



5.3. Results

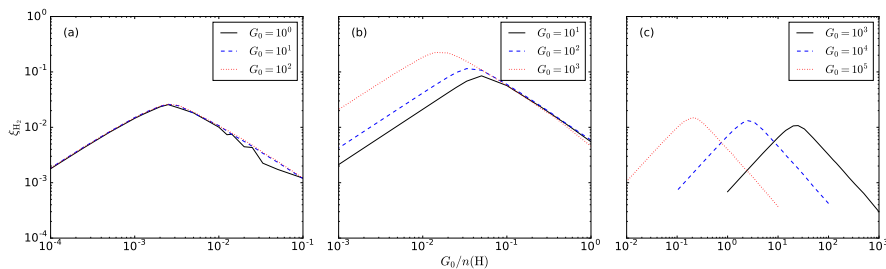


Figure 5.3.: H_2 formation efficiency in the photofragmentation of the coronene (a), ovalene (b) and circumcoronene (c) cations in a variety of interstellar environments.

that in our model we only take into account a single ionization state, the following results represent the total H_2 formation efficiency, based on the cations. Figure 5.3 presents the efficiency of coronene, ovalene and circumcoronene under different UV field intensities and atomic hydrogen densities. Coronene and circumcoronene exhibit ξ_{H_2} in the order of 1–2% under all the environmental conditions explored here. More interestingly, ovalene shows efficiencies at least one order of magnitude higher, depending on the values of G_0 and $n(\text{H})$. However, H_2 formation efficiency in ovalene does not approach unity at any G_0 , even though one could naively expect this given that aliphatic losses are heavily dominated by H_2 -loss. The source of this apparent contradiction is due to the highly efficient loss from partly hydrogenated duos. Hydrogen addition cannot efficiently compete with this form of dehydrogenation, quenching the full rehydrogenation of duos which in turn prevent the formation of a new H_2 unit.

In the case of coronene, the efficiency exhibits the same behavior as a function of G_0 , independently of G_0 . This is due to fact that coronene fragmentation at these values of G_0 is dominated by single photon events (Fig. 5.2). Ovalene and, more prominently, circumcoronene show a large spread in the peak position of ξ_{H_2} with respect to $G_0/n(\text{H})$ as a function of G_0 . This again demonstrates the degree of non-linearity of multiphoton events in PAH fragmentation. From the results presented in Fig. 5.1, it is evident that two-photon events will dominate the fragmentation of ovalene while, for circumcoronene, three photons are required to initiate the dehydrogenation process.

An increase in the peak value of ξ_{H_2} with G_0 reflects the result of the competition between the dehydrogenation channels. Ovalene shows an evident increase in the peak value of the efficiency of molecular hydrogen formation, reflecting the increase of k_{H_2} with increasing G_0 and the near lack of competition with H-loss channels. In coronene, on the other hand, no such increase in ξ_{H_2} is observed, as it is to be expected considering that H-loss is the dominant channel. Unlike coronene, circumcoronene does show a slight increase in H_2 formation efficiency as G_0 increases, but it is nowhere near as evident as for ovalene. The fact that molecular and atomic hydrogen loss are in close competition prevents the increase of ξ_{H_2} to the extent observed in ovalene.

Figure 5.4 shows the contribution of different hydrogenation states to the total population of the molecules, at selected values of G_0 . The peak in the corresponding efficiency curves (Fig. 5.3) coincides with the value of $G_0/n(\text{H})$ that has the largest

V. Molecular hydrogen formation in PDRs

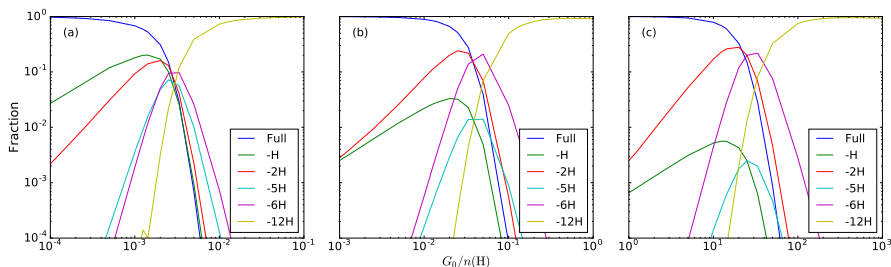
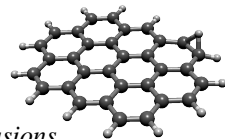


Figure 5.4.: Fragmentation pattern for the coronene (a), ovalene (b) and circumcoronene (c) cations. They are taken at 10, 100 and 1000 G_0 , respectively. -12H corresponds to the point in all molecules where aliphatic loss is no longer possible. Solo hydrogens are still left in the molecule at this stage in ovalene and circumcoronene (two and six, respectively).

contribution from the -6H fragment in all cases. This is to be expected, given that dehydrogenation from duos is the only pathway contributing to H_2 formation and coronene, ovalene and circumcoronene have the same number of duos. For PAHs with a different number of duos or other types of edge structures this situation will vary, but in general molecular hydrogen formation efficiency peaks at the point where half of the structures capable of producing H_2 have become dehydrogenated.

The dehydrogenation pattern shows an enhancement of even hydrogen molecules with respect to odd ones, a well known experimental fact (chapter IV). However, the degree to which PAH fragments with an even number of hydrogens dominates depends on a number of factors. Most notoriously, the dominant fragmentation channel plays a significant role. When comparing coronene and ovalene (Figs. 5.4a and b) it is clear that the fraction of fragments with an odd number of hydrogens in coronene has a larger contribution than that of ovalene. This is to be expected given that fragmentation from coronene is dominated by H-loss. However, there is also a dependency on how dominant the odd H-loss is over the even dehydrogenation channels. Case in point, circumcoronene has higher contributions from photoproducts with an even number hydrogens than ovalene, although the latter is clearly dominated by H_2 -loss dominated, while the former shows a strong competition. Nevertheless, the odd H-loss rate in circumcoronene is faster than any of the even hydrogen loss channels, which leads to a reduced contribution of fragments with an odd hydrogenation.

The tail of ξ_{H_2} at large $G_0/n(H)$ must be considered carefully. Once full dehydrogenation is achieved, the carbon skeleton can isomerize into cages and/or further fragment (Berné & Tielens 2012, and chapter III). This will remove the carbon “flake” from the population, rendering meaningless the calculated value of ξ_{H_2} . However, the presence of solo hydrogens appears to act as a bottleneck in the fragmentation process. As seen in Fig. 5.4, ovalene and circumcoronene retain their last few hydrogens even at fairly large values of $G_0/n(H)$, which merely reflects the low dehydrogenation rate of aromatic solo hydrogens. Nevertheless, one must take into account that this model does not consider isomerizations of the carbon skeleton, neither before nor after full dehydrogenation has taken place. Given that the rate of aromatic H-loss from solo hy-



drogens is rather slow, the internal energy of the molecule can build up further than when aliphatic losses are available. This can, in turn lead to other isomerization routes and/or fragmentation via C containing units.

5.4. DISCUSSION AND CONCLUSIONS

Using the results of the previous section, we can give a simplified expression for ξ_{H_2} . From Fig. 5.4 it is evident that, while the dehydrogenation process is ongoing, most of the molecules will have an even hydrogenation level. This, together with the fact that variations of k_{H_2} with dehydrogenation are not very significant, leads to,

$$\xi_{\text{H}_2} = \frac{2k_{\text{H}_2}}{\kappa_{\text{add}}n(\text{H})}. \quad (5.3)$$

This approximation is generally valid within a factor two up to the peak of the molecular hydrogen formation efficiency and will rapidly diverge from the exact value at large $G_0/n(\text{H})$. The values of G_0 and $n(\text{H})$ at which ξ_{H_2} will peak are, unfortunately, more involved to calculate and a simple analytic expression valid for all PAHs cannot be derived. This is due to the effect of multiphoton absorption (a non-linear process) being an indispensable part of PAH dehydrogenation. Additionally, the dissociation parameters determined here show a wide range of variations among different PAHs, even within the same “family”, as seen for coronene and circumcoronene. The unpredictability of the peak position of H_2 formation efficiency showcases how critical it is to derive accurate photodissociation parameters (in the form of energy barriers and activation enthalpies) and to have experimental confirmation of such values.

The values derived here for ξ_{H_2} at high values of $G_0/n(\text{H})$ have to be carefully considered. Fully dehydrogenated PAHs will rapidly undergo isomerization into fullerenes and other compounds that are not accounted for here. While the presence of solo hydrogens in PAHs appears to delay the onset of the full dehydrogenation, the high value of internal energy that the molecule can reach opens up the possibility of other unimolecular reactions not considered thus far. This caveat should not erode the fact that, in regions where partial hydrogenation makes up the larger fraction of the PAH population, the values derived here are highly accurate.

Even though the exact extent of H_2 formation through PAH fragmentation is heavily dependent on the specifics of the molecule under investigation, the current results do paint a more positive picture of the process than previous work. In a manner analogous to the formation rate in dust grains (R_{d} Hollenbach & McKee 1979; Burke & Hollenbach 1983), the H_2 formation rate in PAHs has been defined by Andrews et al. (2016) as,

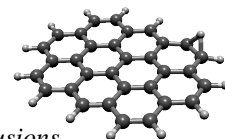
$$R_{\text{PAH}}(\text{H}_2) = \frac{1}{2}\xi_{\text{H}_2}\kappa_{\text{add}}X_{\text{PAH}} \simeq 4 \times 10^{-18} \left(\frac{f_{\text{C}}}{0.1}\right) \left(\frac{50}{N_{\text{C}}}\right) \left(\frac{\xi_{\text{H}_2}}{0.1}\right) \text{cm}^3\text{s}^{-1}, \quad (5.4)$$

where X_{PAH} corresponds to the abundance of PAHs per hydrogen atom, f_{C} is the fraction of elemental carbon locked in PAHs and N_{C} is the number of C-atoms per PAH.

V. Molecular hydrogen formation in PDRs

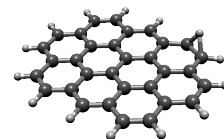
Since the most favorable case within our PAH sample corresponds to ovalene, we will be basing our calculation on its results and using the physical conditions for the well studied NW PDR of NGC 7023. Following this we find $R_{\text{PAH}}(\text{H}_2) \sim 10^{-17} \text{ cm}^3 \text{ s}^{-1}$. This is comparable to the H_2 formation rate on dust grains — $1.5 \times 10^{-17} \text{ cm}^3 \text{ s}^{-1}$ at $T_{\text{gas}} = 400 \text{ K}$ and $T_{\text{d}} = 35 \text{ K}$ — as calculated from the standard expression given by Hollenbach & McKee (1979). While the value for $R_{\text{PAH}}(\text{H}_2)$ calculated here is about two orders of magnitude higher than the previous estimate (Andrews et al. 2016), it is nevertheless not enough to account for the disparity between the H_2 formation rate in PDRs as derived from calculations and observations (Habart et al. 2004). As was recognized by Andrews et al. (2016), Eley-Rideal abstraction from superhydrogenated PAHs is not an efficient process within the photodissociation front of NGC 7023, where they note that Bron et al. (2014) use a value two orders of magnitude higher than the experimentally determined cross-section for coronene films (Mennella et al. 2012).

Molecular hydrogen formation from PAH photofragmentation can be an important process in PDRs, particularly in the region of transition between HI and H_2 . Although the H_2 formation rate derived here is still unable to fully account for the large, observationally determined values in dense PDRs, they represent a step forward towards bridging the gap. Furthermore, these results lend further support to the case for top-down interstellar chemistry, with PAHs as a starting point, to explain the presence of molecules which are otherwise hard to account for using more traditional chemical pathways. The exact contribution to the overall H_2 formation is heavily dependent on molecular properties in ways that have yet to be fully understood. A solution to this issue lies in close collaborations of theoretical and experimental work in order to determine the precise dissociation parameters. Nevertheless, it is evident from this work that, in molecules where the dominant dissociation channel is H_2 -loss, ξ_{H_2} far exceeds previous estimates. Under such conditions, molecular hydrogen formation from PAHs can be on par — and even exceed — the estimated contribution of molecular hydrogen formation from dust grains through Eley-Rideal H_2 abstraction.



ACKNOWLEDGMENTS

Studies of interstellar chemistry at Leiden Observatory are supported through the advanced-ERC grant 246976 from the European Research Council, through a grant by the Netherlands Organization for Scientific Research (NWO) as part of the Dutch Astrochemistry Network, and a Spinoza premie. We acknowledge the European Union (EU) and Horizon 2020 funding awarded under the Marie Skłodowska-Curie action to the EUROPAH consortium, grant number 722346. AC acknowledges NWO for a VENI grant (number 639.041.543). DFT calculations were carried out on the Dutch national e-infrastructure (Cartesius) with the support of SURF Cooperative, under NWO EW projects MP-270-13 and SH-362-15.

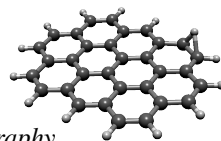


BIBLIOGRAPHY

- Abergel, A., Teyssier, D., Bernard, J. P., et al. 2003, *Astron. Astrophys.*, 410, 577
- Abgrall, H., Le Bourlot, J., Pineau des Fôrets, G., et al. 1992, *Astron. Astrophys.*, 253, 525
- Aihara, J., Fujiwara, K., Harada, A., et al. 1996, *Theochem. J. Mol. Struct.*, 366, 219
- Alecián, E., Catala, C., Wade, G. A., et al. 2008, *Mon. Not. R. Astron. Soc.*, 385, 391
- Allamandola, L. J., Hudgins, D. M., & Sandford, S. A. 1999, *Astrophys. J. Lett.*, 511, L115
- Allamandola, L. J., Tielens, A. G. G. M., & Barker, J. R. 1985, *Astrophys. J. Lett.*, 290, L25
- Allamandola, L. J., Tielens, A. G. G. M., & Barker, J. R. 1989, *Astrophys. J. Suppl. S.*, 71, 733
- Alvaro Galué, H. 2014, *Chem. Sci.*, 5, 2667
- Alvaro Galué, H. & Oomens, J. 2012, *Astrophys. J.*, 746, 83
- Andrews, H., Boersma, C., Werner, M. W., et al. 2015, *Astrophys. J.*, 807, 99
- Andrews, H., Candian, A., & Tielens, A. G. G. M. 2016, *Astron. Astrophys.*, 595, A23
- Aumann, H. H., Beichman, C. A., Gillett, F. C., et al. 1984, *Astrophys. J. Lett.*, 278, L23
- Baboul, A. G., Curtiss, L. A., Redfern, P. C., & Raghavachari, K. 2000, *J. Chem. Phys.*, 110, 7650
- Badger, R. M. 1934, *J. Chem. Phys.*, 2, 128
- Baer, T. & Hase, W. L. 1996, *Unimolecular Reaction Dynamics No. 31* (Oxford, UK: Oxford University Press)
- Bakes, E. L. O. & Tielens, A. G. G. M. 1994, *Astrophys. J.*, 427, 822
- Bakes, E. L. O., Tielens, A. G. G. M., & Bauschlicher, Jr., C. W. 2001, *Astrophys. J.*, 556, 501
- Barker, J. R. 2001, *Int. J. Chem. Kinet.*, 33, 232
- Barker, J. R., Nguyen, T. L., Stanton, J. F., et al. 2017, *MultiWell-2017 Software Suite*, University of Michigan, Ann Arbor, US
- Bauschlicher, Jr., C. W. 1998, *Astrophys. J. Lett.*, 509, L125
- Bauschlicher, Jr., C. W. & Ricca, A. 2014, *Theor. Chem. Acc.*, 133, 1479
- Becker, L. & Bada, J. L. 1994, *Nature*, 372, 507
- Bernard-Salas, J., Cami, J., Peeters, E., et al. 2012, *Astrophys. J.*, 757, 41
- Berné, O., Montillaud, J., & Joblin, C. 2015, *Astron. Astrophys.*, 577, A133

Bibliography

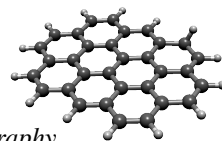
- Berné, O., Mulas, G., & Joblin, C. 2013, *Astron. Astrophys.*, 550, L4
- Berné, O. & Tielens, A. G. G. M. 2012, *Proc. Natl. Acad. Sci.*, 109, 401
- Bialy, S. & Sternberg, A. 2016, *Astrophys. J.*, 822, 83
- Boersma, C., Bauschlicher, Jr., C. W., Ricca, A., et al. 2014, *Astrophys. J. Suppl. S.*, 211, 8
- Boersma, C., Bouwman, J., Lahuis, F., et al. 2008, *Astron. Astrophys.*, 484, 241
- Boersma, C., Rubin, R. H., & Allamandola, L. J. 2012, *Astrophys. J.*, 753, 168
- Boschman, L., Cazaux, S., Spaans, M., Hoekstra, R., & Schlathölter, T. 2015, *Astron. Astrophys.*, 579, A72
- Bouwman, J., de Haas, A. J., & Oomens, J. 2016, *Chem. Commun.*, 52, 2636
- Brand, J. & Blitz, L. 1993, *Astron. Astrophys.*, 275, 67
- Bregman, J. D., Dinerstein, H. L., Goebel, J. H., et al. 1983, *Astrophys. J.*, 274, 666
- Bron, E., Le Bourlot, J., & Le Petit, F. 2014, *Astron. Astrophys.*, 569, A100
- Brown, A. G. A., de Geus, E. J., & de Zeeuw, P. T. 1994, *Astron. Astrophys.*, 289, 101
- Burke, J. R. & Hollenbach, D. J. 1983, *Astrophys. J.*, 265, 223
- Cameron, R. M. 1976, *Sky Telescope*, 52, 327
- Cami, J., Bernard-Salas, J., Peeters, E., & Malek, S. E. 2010, *Science*, 329, 1180
- Campbell, E. K., Holz, M., Gerlich, D., & Maier, J. P. 2015, *Nature*, 523, 322
- Candian, A., Sarre, P. J., & Tielens, A. G. G. M. 2014, *Astrophys. J. Lett.*, 791, L10
- Carraro, G., Turner, D., Majaess, D., & Baume, G. 2013, *Astron. Astrophys.*, 555, A50
- Casey, S. C. 1991, *Astrophys. J.*, 371, 183
- Cazaux, S., Boschman, L., Rougeau, N., et al. 2016, *Sci. Rep.*, 6, 19835
- Cernicharo, J., Daniel, F., Castro-Carrizo, A., et al. 2013, *Astrophys. J. Lett.*, 778, L25
- Cesarsky, D., Lequeux, J., Ryter, C., & Gérin, M. 2000, *Astron. Astrophys.*, 354, L87
- Chase, B., Herron, N., & Holler, E. 1992, *J. Phys. Chem.*, 96, 4262
- Chen, T., Gatchell, M., Stockett, M. H., et al. 2015, *J. Chem. Phys.*, 142, 144305
- Cherchneff, I., Barker, J. R., & Tielens, A. G. G. M. 1992, *Astrophys. J.*, 401, 269
- Cherchneff, I., Le Teuff, Y. H., Williams, P. M., & Tielens, A. G. G. M. 2000, *Astron. Astrophys.*, 357, 572
- Chiar, J. E., Tielens, A. G. G. M., Adamson, A. J., & Ricca, A. 2013, *Astrophys. J.*, 770, 78
- Choi, C. H., Kertesz, M., & Mihaly, L. 2000, *J. of Phys. Chem. A*, 104, 102
- Churchwell, E., Whitney, B. A., Babler, B. L., et al. 2004, *Astrophys. J. Suppl. S.*, 154, 322
- Chuvilin, A., Kaiser, U., Bichoutskaia, E., Besley, N. A., & Khlobystov, A. N. 2010, *Nat. Chem.*, 2, 450
- Cuadrado, S., Goicoechea, J. R., Pilleri, P., et al. 2015, *Astron. Astrophys.*, 575, A82
- Doroshenko, V. M. & Cotter, R. J. 1996, *Rapid Commun. Mass Sp.*, 10, 65
- Doucet, C., Habart, E., Pantin, E., et al. 2007, *Astron. Astrophys.*, 470, 625
- Draine, B. T. 2003, *Annu. Rev. Astron. Astr.*, 41, 241
- Draine, B. T. 2010, *Physics of the Interstellar and Intergalactic Medium* (Princeton, US: Princeton University Press)
- Draine, B. T. & Lee, H. M. 1984, *Astrophys. J.*, 285, 89
- Draine, B. T. & Li, A. 2001, *Astrophys. J.*, 551, 807



- Duley, W. W. 1996, *Mon. Not. R. Astron. Soc.*, 279, 591
- Dupac, X., Bernard, J.-P., Boudet, N., et al. 2003, *Astron. Astrophys.*, 404, L11
- Dyakov, Y. A., Ni, C.-K., Lin, S. H., Lee, Y. T., & Mebel, A. M. 2006, *Phys. Chem. Chem. Phys.*, 8, 1404
- Ekern, S. P., Marshall, A. G., Szczepanski, J., & Vala, M. 1997, *Astrophys. J. Lett.*, 488, L39
- Ekern, S. P., Marshall, A. G., Szczepanski, J., & Vala, M. 1998, *J. Phys. Chem. A*, 102, 3498
- Fabian, J. 1996, *Phys. Rev. B*, 53, 13864
- Flaccomio, E., Damiani, F., Micela, G., et al. 2003, *Astrophys. J.*, 582, 398
- Foing, B. H. & Ehrenfreund, P. 1994, *Nature*, 369, 296
- Frenklach, M. & Feigelson, E. D. 1989, *Astrophys. J.*, 341, 372
- Frisch, M. J., Trucks, G. W., Schlegel, H. B., et al. 2009, *Gaussian 09 Revision D.01*, Gaussian Inc. Wallingford, US 2009
- Fuente, A., Martín-Pintado, J., & Gaume, R. 1995, *Astrophys. J. Lett.*, 442, L33
- Fuente, A., Martín-Pintado, J., Rodríguez-Franco, A., & Moriarty-Schieven, G. D. 1998, *Astron. Astrophys.*, 339, 575
- García-Hernández, D. A., Iglesias-Groth, S., Acosta-Pulido, J. A., et al. 2011, *Astrphys. J. Lett.*, 737, L30
- García-Hernández, D. A., Villaver, E., García-Lario, P., et al. 2012, *Astrophys. J.*, 760, 107
- Genzel, R., Lutz, D., Sturm, E., et al. 1998, *Astrophys. J.*, 498, 579
- Gielen, C., Cami, J., Bouwman, J., Peeters, E., & Min, M. 2011, *Astron. Astrophys.*, 536, A54
- Gillett, F. C., Forrest, W. J., & Merrill, K. M. 1973, *Astrophys. J.*, 183, 87
- Gry, C., Boulanger, F., Nehmé, C., et al. 2002, *Astron. Astrophys.*, 391, 675
- Gudipati, M. S. & Yang, R. 2012, *Astrophys. J. Lett.*, 756, L24
- Guillois, O., Ledoux, G., & Reynaud, C. 1999, *Astrophys. J. Lett.*, 521, L133
- Guzmán, V. V., Pety, J., Goicoechea, J. R., et al. 2015, *Astrophys. J. Lett.*, 800, L33
- Habart, E., Boulanger, F., Verstraete, L., et al. 2003, *Astron. Astrophys.*, 397, 623
- Habart, E., Boulanger, F., Verstraete, L., Walmsley, C. M., & Pineau des Forêts, G. 2004, *Astron. Astrophys.*, 414, 531
- Habart, E., Natta, A., Testi, L., & Carillet, M. 2006, *Astron. Astrophys.*, 449, 1067
- Habing, H. J. 1968, *B. Astron. I. Neth.*, 19, 421
- Handschuh, H., Ganteför, G., Kessler, B., Bechthold, P. S., & Eberhardt, W. 1995, *Phys. Rev. Lett.*, 74, 1095
- Harvey, P. M., Thronson, Jr., H. A., & Gatley, I. 1980, *Astrophys. J.*, 235, 894
- Heger, M. L. 1922, *Lick Observatory Bulletin*, 10, 141
- Herbst, E. & van Dishoeck, E. F. 2009, *Annu. Rev. Astron. Astr.*, 47, 427
- Høg, E., Fabricius, C., Makarov, V. V., et al. 2000, *Astron. Astrophys.*, 355, L27
- Hollenbach, D. J. & McKee, C. F. 1979, *Astrophys. J. Suppl. S.*, 41, 555
- Hollenbach, D. J. & Salpeter, E. E. 1971, *Astrophys. J.*, 163, 155
- Hollenbach, D. J. & Tielens, A. G. G. M. 1997, *Annu. Rev. Astron. Astr.*, 35, 179
- Hollenbach, D. J. & Tielens, A. G. G. M. 1999, *Rev. Mod. Phys.*, 71, 173
- Hony, S., van Kerckhoven, C., Peeters, E., et al. 2001, *Astron. Astrophys.*, 370, 1030

Bibliography

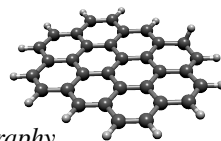
- Houck, J. R., Roellig, T. L., van Cleve, J. E., et al. 2004, *Astrophys. J. Suppl. S.*, 154, 18
- Hudgins, D. M. & Sandford, S. A. 1998, *J. Phys. Chem. A*, 102, 344
- Iglesias-Groth, S., Cataldo, F., & Machado, A. 2011, *Mon. Not. R. Astron. Soc.*, 413, 213
- Iijima, S. 1991, *Nature*, 354, 56
- Jansen, D. J., van Dishoeck, E. F., & Black, J. H. 1994, *Astron. Astrophys.*, 282, 605
- Joblin, C. 2003, in *SF2A-2003: Semaine de l'Astrophysique Française*, ed. F. Combes, D. Barret, T. Contini, & L. Pagani (Les Ulis, France: EDP Sciences), 175
- Joblin, C. 2004, in *The Dense Interstellar Medium in Galaxies*, ed. S. Pflanzner, C. Kramer, C. Staubmeier, & A. Heithausen, Vol. 91 (Berlin, Germany: Springer Proc. Phys.), 517
- Jochims, H. W., Rühl, E., Baumgärtel, H., Tobita, S., & Leach, S. 1994, *Astrophys. J.*, 420, 307
- Jørgensen, J. K., Favre, C., Bisschop, S. E., et al. 2012, *Astrophys. J. Lett.*, 757, L4
- Jura, M. 1975, *Astrophys. J.*, 197, 575
- Kato, T., Kodama, T., Shida, T., et al. 1991, *Chem. Phys. Lett.*, 180, 446
- Katz, N., Furman, I., Biham, O., Pirronello, V., & Vidali, G. 1999, *Astrophys. J.*, 522, 305
- Kemper, C., Spaans, M., Jansen, D. J., et al. 1999, *Astrophys. J.*, 515, 649
- Kessler, M. F., Steinz, J. A., Anderegg, M. E., et al. 1996, *Astron. Astrophys.*, 315, L27
- Knapp, G. R., Brown, R. L., & Kuiper, T. B. H. 1975, *Astrophys. J.*, 196, 167
- Koskinen, P., Malola, S., & Häkkinen, H. 2008, *Phys. Rev. Lett.*, 101, 115502
- Krätschmer, W., Lamb, L. D., Fostropoulos, K., & Huffman, D. R. 1990, *Nature*, 347, 354
- Kroto, H. W., Heath, J. R., O'Brien, S. C., Curl, R. F., & Smalley, R. E. 1985, *Nature*, 318, 162
- Kuan, Y.-J., Charnley, S. B., Huang, H.-C., Tseng, W.-L., & Kisiel, Z. 2003, *Astrophys. J.*, 593, 848
- Kwok, S. 2016, *Astron. Astrophys. Rev.*, 24, 8
- Lada, E. A., DePoy, D. L., Evans, II, N. J., & Gatley, I. 1991, *Astrophys. J.*, 371, 171
- Langhoff, S. R. 1996, *J. Phys. Chem.*, 100, 2819
- Le Page, V., Keheyani, Y., Bierbaum, V. M., & Snow, T. P. 1997, *J. Am. Chem. Soc.*, 119, 8373
- Lebedeva, I. V., Knizhnik, A. A., Popov, A. M., & Potapkin, B. V. 2012, *J. Phys. Chem. C*, 116, 6572
- Léger, A. & Puget, J. L. 1984, *Astron. Astrophys.*, 137, L5
- Leitch, E. M., Readhead, A. C. S., Pearson, T. J., & Myers, S. T. 1997, *Astrophys. J. Lett.*, 486, L13
- Lifshitz, C. 2000, *Int. J. Mass Spectrom.*, 198, 1
- Ling, Y., Gotkis, Y., & Lifshitz, C. 1995, *Eur. J. Mass Spectrom.*, 1, 41
- Ling, Y. & Lifshitz, C. 1998, *J. Phys. Chem. A*, 102, 708
- López-García, M. A., López-Santiago, J., Albacete-Colombo, J. F., Pérez-González, P. G., & de Castro, E. 2013, *Mon. Not. R. Astron. Soc.*, 429, 775



- Mackie, C. J., Candian, A., Huang, X., et al. 2015, *J. Chem. Phys.*, 143, 224314
- Mackie, C. J., Candian, A., Huang, X., et al. 2018, *Phys. Chem. Chem. Phys.*, 20, 1189
- Maier, J. P. 1994, *Nature*, 370, 423
- Malloci, G., Joblin, C., & Mulas, G. 2007, *Chem. Phys.*, 332, 353
- Maltseva, E., Petrigani, A., Candian, A., et al. 2015, *Astrophys. J.*, 814, 23
- Mamyrin, B. A. 2001, *Int. J. Mass Spectrom.*, 206, 251
- March, R. E. 1997, *J. Mass Spectrom.*, 32, 351
- McEwan, M. J., Scott, G. B. I., Adams, N. G., et al. 1999, *Astrophys. J.*, 513, 287
- McGuire, B. A., Carroll, P. B., Loomis, R. A., et al. 2016, *Science*, 352, 1449
- McKellar, A. 1940, *Publ. Astron. Soc. Pac.*, 52, 187
- Menéndez, J. & Page, J. B. 2000, in *Light Scattering in Solids VIII*, ed. M. Cardona & G. Güntherodt (Berlin, Germany: Springer), 27
- Mennella, V. 2006, *Astrophys. J. Lett.*, 647, L49
- Mennella, V., Brucato, J. R., Colangeli, L., & Palumbo, P. 2002, *Astrophys. J.*, 569, 531
- Mennella, V., Hornekær, L., Thrower, J., & Accolla, M. 2012, *Astrophys. J. Lett.*, 745, L2
- Mennella, V., Muñoz Caro, G. M., Ruitkamp, R., et al. 2001, *Astron. Astrophys.*, 367, 355
- Merrill, P. W. & Sanford, R. F. 1938, *Astrophys. J.*, 87, 118
- Merrill, P. W., Sanford, R. F., Wilson, O. C., & Burwell, C. G. 1937, *Astrophys. J.*, 86, 274
- Micelotta, E. R., Jones, A. P., Cami, J., et al. 2012, *Astrophys. J.*, 761, 35
- Micelotta, E. R., Jones, A. P., & Tielens, A. G. G. M. 2010, *Astron. Astrophys.*, 510, A36
- Moffat, A. F. J., Shara, M. M., & Potter, M. 1991, *Astron. J.*, 102, 642
- Montgomery, J. A., Jr., Frisch, M. J., & Ochterski, J. W. 2000, *J. Chem. Phys.*, 112, 6532
- Montillaud, J., Joblin, C., & Toubanc, D. 2013, *Astron. Astrophys.*, 552, A15
- Mookerjee, B., Sandell, G., Jarrett, T. H., & McMullin, J. P. 2009, *Astron. Astrophys.*, 507, 1485
- Neugebauer, G., Habing, H. J., van Duinen, R., et al. 1984, *Astrophys. J. Lett.*, 278, L1
- Nuevo, M., Materese, C. K., & Sandford, S. A. 2014, *Astrophys. J.*, 793, 125
- Ohama, A., Dawson, J. R., Furukawa, N., et al. 2010, *Astrophys. J.*, 709, 975
- Oomens, J., Meijer, G., & von Helden, G. 2001, *J. Phys. Chem. A*, 105, 8302
- Oomens, J., Sartakov, B. G., Meijer, G., & von Helden, G. 2006, *Int. J. Mass Spectrom.*, 254, 1
- Otsuka, M., Kemper, F., Hyung, S., et al. 2013, *Astrophys. J.*, 764, 77
- Otsuka, M., Kemper, F., Sargent, B., et al. 2012, in *Astron. Soc. Pac. Conf. Ser.*, Vol. 458, *Galactic Archaeology*, ed. W. Aoki, M. Ishigaki, T. Suda, T. Tsujimoto, & N. Arimoto, 137
- Pankonin, V. & Walmsley, C. M. 1976, *Astron. Astrophys.*, 48, 341

Bibliography

- Paris, C., Alcamí, M., Martín, F., & Díaz-Tendero, S. 2014, *J. Chem. Phys.*, 140, 204307
- Pearson, K. 1895, *Philos. T. R. Soc. Lond.*, 186, 343
- Peeters, E., Bauschlicher, Jr., C. W., Allamandola, L. J., et al. 2017, *Astrophys. J.*, 836, 198
- Peeters, E., Hony, S., van Kerckhoven, C., et al. 2002, *Astron. Astrophys.*, 390, 1089
- Peeters, E., Tielens, A. G. G. M., Allamandola, L. J., & Wolfire, M. G. 2012, *Astrophys. J.*, 747, 44
- Peng, C., Ayala, P. Y., Schlegel, H. B., & Frisch, M. J. 1996, *J. Comput. Chem.*, 17, 49
- Peng, C. & Schlegel, H. B. 1993, *Isr. J. Chem.*, 33, 449
- Pety, J., Teyssier, D., Fossé, D., et al. 2005, *Astron. Astrophys.*, 435, 885
- Piatti, A. E., Bica, E., & Claria, J. J. 1998, *Astron. Astrophys. Sup.*, 127, 423
- Pilbratt, G. L., Riedinger, J. R., Passvogel, T., et al. 2010, *Astron. Astrophys.*, 518, L1
- Pilleri, P., Herberth, D., Giesen, T. F., et al. 2009, *Mon. Not. R. Astron. Soc.*, 397, 1053
- Pilleri, P., Montillaud, J., Berné, O., & Joblin, C. 2012, *Astron. Astrophys.*, 542, A69
- Pirronello, V., Biham, O., Liu, C., Shen, L., & Vidali, G. 1997, *Astrophys. J. Lett.*, 483, L131
- Poater, J., Visser, R., Solà, M., & Bickelhaupt, F. M. 2007, *J. Org. Chem.*, 72, 1134
- Poglitsch, A., Waelkens, C., Geis, N., et al. 2010, *Astron. Astrophys.*, 518, L2
- Pope, A., Chary, R.-R., Dickinson, M., & Scott, D. 2007, in *Astron. Soc. Pac. Conf. Ser.*, Vol. 380, *Deepest Astronomical Surveys*, ed. J. Afonso, H. C. Ferguson, B. Mobasher, & R. Norris, 387
- Rapacioli, M., Joblin, C., & Boissel, P. 2005, *Astron. Astrophys.*, 429, 193
- Rauls, E. & Hornekær, L. 2008, *Astrophys. J.*, 679, 531
- Rauw, G., De Becker, M., Nazé, Y., et al. 2004, *Astron. Astrophys.*, 420, L9
- Rauw, G., Manfroid, J., Gosset, E., et al. 2007, *Astron. Astrophys.*, 463, 981
- Reed, D. R. & Kass, S. R. 2000, *J. Mass Spectrom.*, 35, 534
- Ricca, A., Bauschlicher, Jr., C. W., Boersma, C., Tielens, A. G. G. M., & Allamandola, L. J. 2012, *Astrophys. J.*, 754, 75
- Rieke, G. H. 2009, *Exp. Astron.*, 25, 125
- Roberts, K. R. G., Smith, K. T., & Sarre, P. J. 2012, *Mon. Not. R. Astron. Soc.*, 421, 3277
- Rodríguez Castillo, S., Simon, A., & Joblin, C. 2018, *Int. J. Mass Spectrom.*
- Rosen, H. & Novakov, T. 1978, *Atmos. Environ.*, 12, 923
- Rosenberg, M. J. F., Berné, O., & Boersma, C. 2014, *Astron. Astrophys.*, 566, L4
- Rubin, R. H., Simpson, J. P., O'Dell, C. R., et al. 2011, *Mon. Not. R. Astron. Soc.*, 410, 1320
- Russell, R. W., Soifer, B. T., & Willner, S. P. 1977, *Astrophys. J. Lett.*, 217, L149
- Sellgren, K. 1984, *Astrophys. J.*, 277, 623
- Sellgren, K., Werner, M. W., Ingalls, J. G., et al. 2010, *Astrophys. J. Lett.*, 722, L54
- Sephton, M. A. & Botta, O. 2008, *Space Sci. Rev.*, 135, 25
- Sheffer, Y., Wolfire, M. G., Hollenbach, D. J., Kaufman, M. J., & Cordier, M. 2011, *Astrophys. J.*, 741, 45



- Shetty, R., Kauffmann, J., Schnee, S., & Goodman, A. A. 2009, *Astrophys. J.*, 696, 676
- Smith, J. D. T., Armus, L., Dale, D. A., et al. 2007a, *Publ. Astron. Soc. Pac.*, 119, 1133
- Smith, J. D. T., Draine, B. T., Dale, D. A., et al. 2007b, *Astrophys. J.*, 656, 770
- Snow, T. P. 2001, *Spectrochim. Acta A*, 57, 615
- Snow, T. P., Le Page, V., Keheyan, Y., & Bierbaum, V. M. 1998, *Nature*, 391, 259
- Snyder, L. E., Lovas, F. J., Hollis, J. M., et al. 2005, *Astrophys. J.*, 619, 914
- Stafford, Jr., G. C., Kelley, P. E., Syka, J. E. P., Reynolds, W. E., & Todd, J. F. J. 1984, *Int. J. Mass Spectrom.*, 60, 85
- Steiman-Cameron, T. Y., Haas, M. R., Tielens, A. G. G. M., & Burton, M. G. 1997, *Astrophys. J.*, 478, 261
- Sternberg, A., Le Petit, F., Roueff, E., & Le Bourlot, J. 2014, *Astrophys. J.*, 790, 10
- Swings, P. & Rosenfeld, L. 1937, *Astrophys. J.*, 86, 483
- Thaddeus, P. & McCarthy, M. C. 2001, *Spectrochim. Acta A*, 57, 757
- Thi, W.-F., van Dishoeck, E. F., Bell, T., Viti, S., & Black, J. 2009, *Mon. Not. R. Astron. Soc.*, 400, 622
- Thrower, J. D., Jørgensen, B., Friis, E. E., et al. 2012, *Astrophys. J.*, 752, 3
- Thrower, P. A. 1999, *Carbon*, 37, 1677
- Tielens, A. G. G. M. 2005, *The Physics and Chemistry of the Interstellar Medium* (Cambridge, UK: Cambridge University Press)
- Tielens, A. G. G. M. 2008, *Annu. Rev. Astron. Astr.*, 46, 289
- Tielens, A. G. G. M. 2013, *Rev. Mod. Phys.*, 85, 1021
- Trinquier, G., Simon, A., Rapacioli, M., & Gadéa, F. X. 2017a, *Mol. Astrophys.*, 7, 27
- Trinquier, G., Simon, A., Rapacioli, M., & Gadéa, F. X. 2017b, *Mol. Astrophys.*, 7, 37
- Vijh, U. P., Witt, A. N., & Gordon, K. D. 2004, *Astrophys. J. Lett.*, 606, L65
- Wakelam, V., Bron, E., Cazaux, S., et al. 2017, *Mol. Astrophys.*, 9, 1
- Werner, M. W., Roellig, T. L., Low, F. J., et al. 2004, *Astrophys. J. Suppl. S.*, 154, 1
- West, B., Useli-Bacchitta, F., Sabbah, H., et al. 2014, *J. Phys. Chem. A*, 118, 7824
- Westerlund, B. 1961, *Ark. Astron.*, 2, 419
- Whiteoak, J. B. Z. & Uchida, K. I. 1997, *Astron. Astrophys.*, 317, 563
- Wiesenfeld, L., Oomens, J., & Cheung, A. S. C. 2018, *Phys. Chem. Chem. Phys.*, 20, 5341
- Witt, A. N., Graff, S. M., Bohlin, R. C., & Stecher, T. P. 1987, *Astrophys. J.*, 321, 912
- Young Owl, R. C., Meixner, M. M., Fong, D., et al. 2002, *Astrophys. J.*, 578, 885
- Zhang, Y. & Kwok, S. 2011, *Astrophys. J.*, 730, 126
- Zhang, Y. & Kwok, S. 2015, *Astrophys. J.*, 798, 37
- Zhao, Y. & Truhlar, D. G. 2011, *J. Chem. Theory and Comput.*, 7, 669
- Zhen, J., Castellanos, P., Linnartz, H., & Tielens, A. G. G. M. 2016, *Mol. Astrophys.*, 5, 1
- Zhen, J., Paardekooper, D. M., Candian, A., Linnartz, H., & Tielens, A. G. G. M. 2014, *Chem. Phys. Lett.*, 592, 211
- Zheng, G., Wang, Z., Irlé, S., & Morokuma, K. 2007, *J. Nanosci. Nanotechnol.*, 7, 1662

Bibliography

Zimmerman, J. A., Eyler, J. R., Bach, S. B. H., & McElvany, S. W. 1991, *J. Chem. Phys.*, 94, 3556

Zuckerman, B., Buhl, D., Palmer, P., & Snyder, L. E. 1970, *Astrophys. J.*, 160, 485

NEDERLANDSE SAMENVATTING

Astrochemie bestudeert de vorming en fragmentatie processen van moleculen in het interstellair medium, waar de condities waaronder chemische reacties plaatsvinden erg verschillen van die op aarde; Dichtheden en temperaturen zijn heel veel lager en ultraviolette straling is sterker en kan gevormde complexen eenvoudig afbreken. Deze moleculen zijn niet alleen interessant door de chemische reacties die ze kunnen ondergaan onder de exotische omstandigheden in de ruimte, maar ook omdat ze kunnen worden gebruikt om de fysische omstandigheden in de gebieden waarin ze zich bevinden te kunnen karakteriseren. Aangezien ultraviolet licht efficiënt is in het afbreken van moleculen, heeft een groot veld binnen de astrochemie zich met name toegespitst op de meer “afgeschermd” gebieden, waar de dichtheden naar interstellair standaard hoog zijn (maar nog steeds erg laag vergeleken met dichtheden op Aarde) en de destructieve fotonen niet diep in deze gebieden kunnen doordringen. Echter, het is al enige tijd bekend dat grote koolstof houdende moleculen door hun bijzondere stabiliteit in sterk bestraalde gebieden veel langer kunnen overleven dan andere moleculen.

Van de reacties die relevant zijn in de ruimte, zijn degene die op het oppervlak plaatsvinden van kleine stofdeeltjes, die intiem gemixt zijn met het gas in het interstellair medium, het best bestudeerd. In gebieden in de ruimte waar ultraviolette straling niet efficiënt kan doordringen en de temperatuur tot slechts tientallen graden boven het absolute nulpunt valt, vriezen atomen en moleculen vast op stofdeeltjes en vormen dunne laagjes ijs. Hierdoor neemt de kans dat moleculen interacties aangaan en door middel van chemische reacties meer complexe moleculen vormen toe. Dit type reacties kan voor enkele moleculen efficiënt zijn in de gasfase, maar de waarschijnlijkheid dat het gebeurt is erg laag. Dit mechanisme, waarbij kleine eenheden samengevoegd worden om complexere moleculen te vormen, wordt “bottom-up” interstellair chemie genoemd.

Zoals eerder genoemd, worden er grote koolstof houdende moleculen waargenomen die overleven in gebieden waar de meeste moleculen niet kunnen overleven. Van deze moleculen zijn polycyclische aromatische koolwaterstoffen (PAKs) - een familie van moleculen die aan de hand van hun infrarood emissiebanden kunnen worden waargenomen - de meest voorkomende. PAKs zijn moleculen die bestaan uit ringen die aan elkaar vastzitten (polycyclisch) en aromatische bindingen bevatten (een type binding waarbij elektronen gedeeld worden over het gehele molecuul en niet gebonden zijn aan specifieke atomen). De aaneengesloten ringen lijken op een honingraatstructuur, waarbij de hoeken bestaan uit koolstofatomen en de buitenkant afgesloten wordt met

waterstofatomen. Deze moleculen zijn typisch erg groot en er zitten tussen de 50 en 100 koolstof in deze moleculen opgesloten. Hoewel deze PAKs erg stabiel zijn, fragmenteren ze uiteindelijk ook en hun fragmentatie producten zijn erg verschillend van de producten die op interstellair ijs gevormd worden. Dit proces kan ook met andere moleculen beginnen, maar de stabiliteit en veel voorkomendheid van PAKs zorgt ervoor dat ze de ideale kandidaat zijn voor dit type reacties. Deze aanpak in de interstellaire chemie wordt “top-down” chemie genoemd en de karakterisering ervan en de impact op de sterrenkunde is het voornaamste onderwerp van dit proefschrift.

PAKs zijn niet de enige grote stabiele moleculen waarvan we weten dat ze zich in het interstellaire medium bevinden. Minder dan een decennium geleden zijn enkele fullerenen gedetecteerd op basis van hun mid-infrarood emissie banden in meerdere objecten zowel binnen als buiten de Melkweg. In tegenstelling tot PAKs bestaan fullerenen uit gesloten in plaats van platte structuren en ze bevatten alleen maar koolstof atomen, gerangschikt in vijftringen en zesringen. De meest stabiele en representatieve fullereen is buckminsterfullereen, welke bestaat uit zestig koolstof atomen en lijkt op een klassieke zwart-witte voetbal. Er is gesuggereerd dat fullerenen gevormd worden door de fragmentatie van PAKs in regio's die fotodissociatie gebieden (PDRs) worden genoemd. Deze gebieden bestaan uit zones waar de stralingsvelden de chemische en fysische processen domineren. De naam komt voort uit het feit dat in deze gebieden de overgang tussen atomair en moleculair gas plaatsvindt. De kant van de PDR die de meeste straling opvangt bestaat hoofdzakelijk uit neutraal atomair gas en als de afstand tot de stralingsbron toeneemt, wordt de dichtheid hoger en worden moleculen gevormd, waarmee de overgang naar een moleculaire wolk is ingezet.

Het precieze gebied waar de overgang tussen atomair en moleculair gas in een PDR plaatsvindt hangt af van het molecuul dat wordt beschouwd. Het eerste molecuul wat gevormd wordt is waterstof (H_2) welke het meest voorkomt in de ruimte. Waterstof kan onder de omstandigheden in de ruimte niet in de gas fase gevormd worden en een katalytische reactie is vereist om de aanwezigheid te verklaren. De meest gangbare reactie vindt plaats op het oppervlak van interstellaire stofdeeltjes tussen twee waterstof atomen. Echter, waarnemingen van H_2 vorming in dichte PDRs tonen aan dat de vormingssnelheid honderd maal sneller is dan verwacht op basis van de reacties op de stofdeeltjes. Reacties waarin PAKs een rol spelen zijn ook voorgesteld als een mogelijk pad naar H_2 , maar de resultaten zijn nog niet voldoende overtuigend.

Een groot deel van dit proefschrift is gebaseerd op experimentele data die gemeten zijn op een instrument genaamd instrument voor fotodynamica van PAKs (i-PoP). Het apparaat bestaat uit een quadropool ionenval waaraan een time-of-flight massa spectrometer is gekoppeld. De moleculen die bestudeerd worden, worden verdampt met behulp van een oven in een hoog vacuüm kamer waarin de druk lager is dan 10^{-10} keer de atmosferische druk. Vervolgens worden de moleculen geïoniseerd met behulp van energetische elektronen en worden de ionen gevangen in een elektrisch veld, waarin ze bestraald kunnen worden met een laser. Het mengsel van aanvankelijke moleculen en fragmentatieproducten wordt geanalyseerd met behulp van time-of-flight massa spectrometrie, waarbij de lichte bestanddelen een korte vluchtduur vertonen en de zware ionen later aankomen op de detector. Hierdoor kunnen de massa's van de fotoproducten bestudeerd worden, maar de specifieke structuren van de moleculen zijn nog

onbekend.

Dit proefschrift behandelt de fotofragmentatie van PAKs in het interstellair medium, met een speciale nadruk op de vorming van fullerenen en moleculair waterstof. Deze producten zijn zeker niet de enige producten zijn die gevormd worden in PAK fragmentatie, maar zijn wel bijzonder relevant voor sterrenkunde en hun stabiliteit maakt ze ideaal om de top-down chemie te volgen. Fullerenen blijken veelvoorkomende moleculen te zijn en er is sterk bewijs dat ze drager zijn van de diffuse interstellair banden (DIBs). DIBs, absorptiebanden die ruim een eeuw geleden voor het eerst zijn waargenomen, vormen de langst staande open vraag van de hedendaagse sterrenkunde. De stof die deze absorptiebanden veroorzaakt is waarschijnlijk moleculair, maar een eenduidige toekenning is nog niet gedaan.

De vorming van fullerenen wordt behandeld in hoofdstuk II door gebruik te maken van mid- en ver-infrarood data van *Spitzer* en *Herschel* van een zevental PDRs. De abundantie van PAKs en fullerenen bewijzen dat er trends zitten in de vorming van deze stoffen in de bronnen die ruimtelijk opgelost zijn. Universele trends over alle PDRs zijn echter niet gevonden. De bronnen waar fullerenen gedetecteerd zijn, worden gekenmerkt door fysische condities die consistent zijn met volledige de-hydrogenatie van grote PAKs, wat de eerste stap vormt in het vormen van fullerenen in het top-down model. Echter, de abundantie van fullerenen, alsook het gebrek aan een algemene trend suggereert dat andere parameters, zoals de leeftijd van de PDR, een belangrijke rol speelt in fullerenen vorming.

Hoofdstuk III beschrijft experimenteel bewijs voor de vorming van fullerenen door bestraling van grote PAKs. Door de massa spectra van de fotodissociatie van PAKs en fullerenen te vergelijken, is duidelijk te zien dat ze dezelfde “magische massa’s” vormen. Deze corresponderen met fullerenen structuren met een hogere stabiliteit dan andere moleculen met dezelfde massa. Experimenten aan fullerenen hebben aangetoond dat alle fragmentatie stopt zodra de fragmenten de massa van C_{60}^+ bereiken. PAKs kunnen verder dissociëren, maar het patroon van de magische massa’s verdwijnt na C_{60}^+ en een grote fractie van C_{60}^+ blijft bestaan, zelfs wanneer het bestraald wordt met intense laser straling. Dit werk toont solide bewijs dat fullerenen gevormd worden door top-down chemie in het interstellair medium.

PAH de-hydrogenatie is een kritisch proces in het beantwoorden van twee vragen die in dit proefschrift centraal staan; Het is de eerste stap in de vorming van fullerenen uit PAKs en het is het moment waarop moleculair waterstof gevormd kan worden. Daarom wordt in hoofdstuk IV een uitgebreide studie van dit proces beschreven. Het verlies van de eerste vier waterstofatomen van negen PAKs is experimenteel bestudeert met specifieke focus op de verhouding tussen het verliezen van even en oneven aantallen waterstofatomen, aangezien dit kern informatie bevat over de competitie tussen sequentieel atomair waterstof verlies en moleculair waterstof verlies. Van drie van de PAKs is een kwantumchemisch model gemaakt wat de fragmentatie beschrijft, inclusief het rondwalen van het waterstofatoom langs de rand van de PAK. De experimentele resultaten en het model zijn met elkaar vergeleken en de mobiliteit van het waterstof is heel belangrijk gebleken in het begrijpen van de fragmentatie. De vorming van moleculair waterstof blijkt belangrijker te worden, naar mate de PAK groter wordt.

Om het belang van de vorming van moleculair waterstof in de dichte PDRs te be-

Nederlandse samenvatting

grijpen, zijn de voorgaande resultaten gebruikt in een bestaand model van de fotodissociatie van PAKs in PDRs. De resultaten betreffende een selectie van drie PAKs, gespreid over alle mogelijke waterstof verlies scenario's (H-verlies is dominant, H₂ verlies is dominant en beide processen zijn competitief) is gepresenteerd in hoofdstuk V. In PAKs waarin H-verlies dominant is, of de beide processen competitief zijn, is de waterstof vorming niet significant verschillend dan in voorgaande studies. Als waterstof verlies gedomineerd wordt door H₂-verlies, neemt de efficiëntie ongeveer toe met een factor ~20. Deze toename is niet voldoende om de waargenomen vorming te verklaren, maar maakt het verschil wel aanzienlijk kleiner. Een verdere studie van het effect van de grootte van de PAK op de dissociatie snelheden kan dit verschil mogelijk verder verkleinen.

ENGLISH SUMMARY

Astrochemistry studies the formation and fragmentation processes of molecules in the interstellar medium, where the conditions for chemistry are very different from those on Earth since densities and temperatures are far lower and the ultraviolet radiation is stronger and can easily break down most complexes. These molecules are not only interesting from the perspective of the chemical reactions they can undergo under the exotic conditions of space, but also because they can be used to trace the physical conditions of the regions where they reside. Since ultraviolet light is efficient when it comes to destroying molecules, a large part of the research in astrochemistry has been focused on more “shielded” regions, where the density is high for the general interstellar medium (but still low when compared to those typically found on Earth) and thus the more destructive photons cannot enter deep inside the region. However, it has been known for some time that large carbon molecules can survive far longer than others in highly irradiated environments due to their high stability.

Among those relevant for space, the best studied chemical reactions are those that occur on the surface of dust grains, which are intermixed with the gas in the interstellar medium. In regions of space where ultraviolet radiation cannot penetrate efficiently and the temperatures drop to only a few dozen degrees above absolute zero, atoms and molecules can freeze on top of dust grains. This increases the chance for them to interact with each other and react to form more complex molecules. This type of reactions in the gas phase can be efficient for a few molecules, but are generally much less likely to occur. This mechanism, where small units are joined together (either in the gas phase or as part of ices), is referred to as “bottom-up” interstellar chemistry.

As mentioned before, large carbon molecules are observed to survive for longer under physical conditions that can quickly destroy most other molecules. Of these, the most abundant are polycyclic aromatic hydrocarbons (PAHs), a whole family of molecules which can be observed by their vibrational emission lines in the mid-infrared. PAHs correspond to molecules consisting of multiple rings joined together (thus polycyclic), and characterized by “aromatic” bonds (a specific type of chemical bonding where some of the electrons are delocalized over the surface of the molecule). The joined rings resemble honeycomb cells, with the vertexes made out of carbon atoms, and the outer edge is terminated by hydrogen atoms. These molecules are typically large, with their carbon content estimated to be between fifty and a hundred atoms. Even though these hydrocarbons are highly stable, they will eventually fragment as well and their destruction can form product molecules very different from those cre-

ated on icy dust grain surfaces. This process can have also different molecules as a starting point, but the abundance and stability of PAHs makes them ideal candidates to dominate this type of chemical reactions. This approach to interstellar chemistry is known as “top-down”, and its characterization and impact in astronomy is the main focus of this thesis.

PAHs are not the only large, stable molecule known to exist in the interstellar medium. Less than a decade ago, the fullerene family of molecules were also detected through their mid-infrared emission in multiple galactic and extragalactic objects. Unlike PAHs, fullerenes have a closed cage rather than planar structure and contain exclusively carbon atoms, with a mixture of pentagons and hexagons. The most stable and representative fullerene is buckminsterfullerene, which contains sixty carbon atoms and resembles an old fashioned, black and white football. It has been hypothesized that fullerenes can be formed through the fragmentation of PAHs in areas of the interstellar medium known as photodissociation regions (PDR). These correspond to zones where the strong radiation fields dominate the chemical and physical processes of the interstellar medium. Their name stems from the fact that it is within these regions that the transition between atomic and molecular gas takes place. The side of the PDR which faces the radiation field is dominated by neutral, atomic gas and, as the distance from the source of photons increases, the density increments as well and the particles coalesce into molecules, gradually passing into what is called the molecular cloud.

The exact zone of transition between atomic and molecular gas inside PDRs depends on which molecule is being considered. The first molecule to form (if we look at the PDR from the radiation source and into the molecular cloud) is molecular hydrogen (H_2), which is also the most abundant molecule in the universe. H_2 cannot be formed in the gas phase under the conditions of the interstellar medium, instead requiring catalytic reactions to account for its formation rate. The most common such reaction consists on the deposition of hydrogen atoms onto the surface of interstellar dust grains, where they can react and be released as molecular hydrogen. However, observations of the H_2 formation rate in dense PDRs show that it is about a hundred times larger than the formation rate expected from reactions on dust grains. Reactions involving PAHs have been considered in attempts to reconcile H_2 formation models, but thus far the results have been unsatisfactory.

Much of this thesis work is based on experimental data, collected using the instrument for photodynamics of PAHs (i-PoP). This consists of a quadrupole ion trap attached to a time-of-flight reflectron mass spectrometer. The molecules studied are evaporated using an oven under high vacuum (with pressure about 10^{-10} times lower than atmospheric) and ionized through collisions with electrons. The ions thus formed are then stored in the quadrupole ion trap, where they are irradiated using a laser. The mixture of the original molecule and its fragmentation products are then observed through the time-of-flight mass spectrometer, where species with different masses arrive at the detector at different times. This allows for an understanding of the composition of the photoproducts, but lacks direct evidence on the specific structures formed at each mass.

This thesis deals with the photofragmentation of PAHs in the interstellar medium, with special emphasis on the formation of fullerenes and molecular hydrogen. While these are certainly not the only possible products of PAH fragmentation, they are of

particular relevance for astronomy and their high stability makes them ideal probes of top-down chemical processing. Fullerenes appear to be an abundant species in the interstellar medium and there is strong evidence suggesting that they are the source of some of the diffuse interstellar bands (DIBs). The DIBs are one of the longest standing open questions in astronomy, having been discovered almost a hundred years ago, they appear as absorption lines in the spectra of stars, but its origin is clearly interstellar. The carrier of the DIBs are thought to be molecular but no undisputed identification has been provided. Molecular hydrogen is the most abundant molecule in the universe, but its formation rate in dense PDRs cannot be accounted for using only reactions on dust grains or direct PAH photodissociation. PAHs are known to be abundant in dense PDRs and to fragment at the PDR front (the transition zone between molecular and atomic hydrogen). Isomerization reactions, where the molecular structure changes without the loss of atoms, can enhance H₂ formation from PAH. The approach followed here to investigate both these processes is based on a combination of observations, experiments, theoretical calculations and computational models.

The question of fullerene formation has been addressed in chapter II by using mid- and far-infrared data from *Spitzer* and *Herschel* on a sample of seven PDRs. The abundance of PAHs and fullerenes show evidence of formation trends within resolved sources, but universal trends among all PDRs were not found when taking into account either the radiation field or the ratio of the radiation field over the atomic hydrogen density (related to hydrogen recombination). The sources where fullerenes were conclusively detected have physical conditions consistent with full dehydrogenation of large PAHs, the first step in fullerene formation in a top-down model. However, the abundance of fullerenes, as well as the lack of an overall trend suggest that other parameters, such as PDR age, play a key factor in fullerene formation.

Chapter III provides experimental evidence for the formation of fullerenes from large PAHs. By comparing the photodissociation pattern in mass spectra of PAHs and fullerenes, both clearly display the same “magic numbers”. These correspond to fullerene structures with higher stability than others with similar mass. Additionally, both species were also irradiated using light with a 532 nm wavelength, at which the C₆₀⁺ fullerene does not absorb light. Experiments using fullerenes showed that all fragmentation stops when the fragments reach the mass of C₆₀⁺. PAHs can dissociate further, but the “magic number” pattern disappears after C₆₀⁺ and a high fraction of the C₆₀⁺ peak remains even at high laser power. This experimental work shows solid evidence for top-down formation of fullerenes in the interstellar medium.

PAH dehydrogenation is a critical process in tackling both questions posed on this thesis. It is the first step in the formation of fullerenes, and it is the instance in which molecular hydrogen can proceed. As such, an extensive study of this process is presented in chapter IV. The first four hydrogen losses from a sample of nine PAHs were studied experimentally, specifically focusing on the ratio between odd and even hydrogen losses as they hold key information on the competition between sequential atomic hydrogen loss and molecular hydrogen loss. For three of the PAHs, a model of the fragmentation process including the possibility of hydrogen mobility along the edge of the molecule, was made on the base of quantum chemical calculations. The experimental results were compared to those of the model and the hydrogen mobility reactions

English summary

were found to be critical in explaining the fragmentation process. Molecular hydrogen formation was found to grow in importance as PAH size increases.

To assess the importance of molecular hydrogen formation from PAHs in the context of dense PDRs, the previous results were used to modify an existing model of PAH photodissociation in PDRs. A selection of three PAHs, spanning the possible dehydrogenation scenarios (i.e.: H-loss dominated, H₂-loss dominated and competitive), are presented in chapter V. In PAHs for which H-loss dominates or the two loss processes are in high competition, the molecular hydrogen formation efficiency is not significantly different from those derived in other studies. If the PAH dehydrogenation is dominated by H₂-loss, the efficiency increases by a factor ~20. While this increase is not enough to match the observed formation rate, it reduces the disparity by a great margin. Further work on the size dependence of the dissociation rates has the potential of clearing up this issue.

RESUMEN EN CASTELLANO

La astroquímica estudia los procesos de formación y fragmentación de moléculas en el medio interestelar, donde las condiciones físicas son radicalmente distintas con respecto a las que se encuentran en la Tierra, debido a que la densidad y la temperatura son mucho más bajas, mientras que la radiación ultravioleta es más intensa y es capaz de destruir fácilmente la mayoría de estas. Las moléculas que se encuentran en el espacio no son sólo interesantes desde la perspectiva de las reacciones químicas que ocurren bajo las exóticas condiciones del medio interestelar, si no que también pueden ser usadas para determinar las condiciones físicas de las regiones en las que se encuentran. Dado que los fotones ultravioleta tienen la capacidad de destruir moléculas de forma eficiente, una buena parte de la investigación en astroquímica se ha enfocado en las áreas más “resguardadas”, donde la densidad es alta para lo que es el medio interestelar (aunque es aún baja en comparación con las que típicamente se encuentran en ambientes terrestres) permitiendo así que los fotones más destructivos no puedan penetrar profundamente en estas regiones. Sin embargo, desde hace algún tiempo se sabe que grandes moléculas de carbono pueden sobrevivir por largos períodos en ambientes sometidos a radiación intensa, debido a su estabilidad.

De las reacciones químicas más relevantes en el espacio, las mejor estudiadas son aquellas que ocurren en la superficie de los granos de polvo que se encuentran entremezclados con el gas en el medio interestelar. En regiones donde la radiación ultravioleta no es capaz de penetrar eficientemente y donde la temperatura es sólo de unos pocos grados sobre el cero absoluto, distintos átomos y moléculas pueden congelarse sobre los granos de polvo. Esto incrementa la posibilidad de que interactúen entre sí y reaccionen para formar moléculas más complejas. Por otro lado, este tipo de encuentros entre átomos o moléculas en la fase gaseosa es eficiente en la formación de unas pocas moléculas, pero son mucho más improbables por lo general. Este mecanismo, por el cual pequeñas partes se unen para formar especies de mayor tamaño (ya sea en la fase gaseosa o en mantos de hielo), se conoce como química interestelar “de abajo hacia arriba”.

Como ya se ha dicho, se ha observado que moléculas de carbono de gran tamaño sobreviven por largo tiempo bajo condiciones físicas que destruirían rápidamente la mayor parte de las demás. De estas, las más abundantes son los hidrocarburos aromáticos policíclicos (HAP o PAH, por sus siglas en inglés), una familia de moléculas que son observadas a partir de sus líneas de emisión vibracionales en el infrarrojo medio. Los HAP están constituidos de múltiples anillos hexagonales fusionados (de ahí que

sean policíclicos) y se caracterizan por poseer enlaces “aromáticos” (un tipo de enlace químico en el cual parte de los electrones se encuentran distribuidos a lo largo de toda la molécula). La unión de los anillos sigue una estructura similar a la de las celdas de una colmena, con átomos de carbono en los vértices y con la parte exterior acabada en átomos de hidrógeno. Se estima que los HAP en el medio interestelar contienen entre cincuenta y cien átomos, lo que los hace fácilmente las moléculas de mayor tamaño encontradas en el espacio hasta el momento. A pesar de su alta estabilidad, estos hidrocarburos también se fragmentan eventualmente y, a partir de su destrucción, nuevas moléculas pueden formarse, distintas a las que se crean en los mantos de hielo de los granos de polvo. Aunque este tipo de procesamiento no está limitado a los HAP, la abundancia y estabilidad de estos últimos hace de ellos candidatos ideales para este tipo de reacciones. Esta forma de química interestelar se conoce como “de arriba hacia abajo” y su caracterización e impacto en astronomía son el tópico principal de esta tesis.

Los HAP no son las únicas moléculas estables de gran tamaño que se conocen en el medio interestelar. Hace menos de una década, otra familia de moléculas conocidas como fulerenos fue detectada a través de su emisión infrarroja en múltiples fuentes galácticas y extragalácticas. A diferencia de los HAP, los fulerenos tienen una estructura tridimensional cerrada, en lugar de plana, y contienen sólo átomos de carbono, estructurados en forma de hexágonos y pentágonos. El fullereno más estable y representativo es buckminsterfullereno, el cual está formado por sesenta átomos de carbono y tiene la forma de un balón de fútbol clásico. Se ha sugerido que los fulerenos pueden ser formados a través de la fragmentación de HAP en áreas del medio interestelar conocidas como regiones de fotodisociación (RFD o PDRs en inglés). Estas últimas son zonas donde el intenso campo de radiación domina los procesos físicos y químicos del medio interestelar. Su nombre deriva del hecho de que es en estas regiones donde la transición entre gas atómico y molecular tiene lugar. El lado de la RFD que da al campo de radiación está dominado por gas atómico en estado neutro y, a medida en que la distancia a la fuente de radiación aumenta, la densidad se incrementa a su vez y los átomos se unen formando moléculas, pasando gradualmente a lo que se denomina como nube molecular.

El área exacta en que la transición entre gas atómico y molecular ocurre dentro de la RFD depende de la molécula que se tenga en consideración. La primera molécula en formarse (si miramos la RFD desde la fuente de radiación en dirección a la nube molecular) es hidrógeno, H_2 , la cual es también la molécula más abundante del universo. No es posible formar hidrógeno molecular en la fase gaseosa del medio interestelar, por lo que se requiere de catalizadores para dar cuenta de su tasa de formación. De estas reacciones, la más común consiste en la absorción de átomos de hidrógeno en la superficie de granos de polvo, en donde pueden reaccionar entre sí y ser liberados como hidrógeno molecular. Sin embargo, observaciones de la tasa de formación de H_2 en RFD densas han dado un valor casi cien veces mayor del que se esperaría fuese debido a la formación sobre granos de polvo. Reacciones que involucran HAP como catalizadores también han sido consideradas, pero hasta el momento los resultados siguen mostrando una gran discrepancia con las observaciones.

Una gran parte de esta tesis se basa en datos experimentales, los cuales fueron

recolectados usando el instrumento para la fotodinámica de HAP (i-PoP en inglés). Este consiste en una trampa cuadrupolar de iones acoplada a un espectrómetro de masa de tiempo de vuelo con un espejo iónico. Las moléculas a ser estudiadas son evaporadas usando un horno que se encuentra en una cámara de alto vacío (con una presión aproximadamente 10^{-10} veces menor a la atmosférica) y ionizadas usando colisiones con electrones. Los iones así formados se almacenan luego en la trampa de iones cuadrupolar, usando un campo electromagnético y aquí son irradiados usando un láser. Las moléculas originales, así como los fragmentos producidos por el láser, son observados posteriormente usando el espectrómetro de masa. Las especies en cuestión son aceleradas por un campo uniforme, haciendo que los diferentes tiempos de llegada al detector correspondan con sus respectivas masas. Esto permite evaluar la composición de los productos, pero no provee información directa sobre la estructura de los mismos.

Esta tesis trata de la fotofragmentación de HAP en el medio interestelar, con un énfasis especial en la formación de fulerenos e hidrógeno molecular. A pesar de que, claramente, estos no son los únicos productos formados a partir de la fragmentación de HAP, son particularmente relevantes para la astronomía, y su alta estabilidad hace de ellos sujetos de prueba ideales de la química “de arriba hacia abajo”. Los fulerenos son abundantes en el medio interestelar y hay bastante evidencia de que son la fuente de algunas de las bandas interestelares difusas (BID o DIBs, por sus siglas en inglés). Las BID son una de las interrogantes de más larga data en astronomía. Fueron descubiertas hace casi cien años en la forma de líneas de absorción en el espectro de estrellas, pero tienen un origen interestelar. Se piensa que las BID tienen un origen molecular, pero la identificación indiscutible de una o más de ellas no ha sido posible. Por otro lado, hidrógeno molecular es la molécula más abundante del medio interestelar, pero su tasa de formación en RFD densas no puede ser explicada sólo a partir de reacciones en granos de polvo, o a través de la fotodisociación directa de HAP. Se sabe que los HAP son abundantes en RFD densas y que se fragmentan en el frente de las RFD (la zona de transición entre hidrógeno atómico y molecular). Las reacciones de isomerización, en las cuales la estructura de la molécula cambia, pero sin la pérdida de átomos, puede facilitar la formación de H_2 en HAP. La investigación de ambos procesos sigue un procedimiento multidisciplinario, combinando observaciones astronómicas, experimentos, cálculos teóricos y modelos computacionales.

La formación de fulerenos en el medio interestelar es investigada en el capítulo II a través de observaciones en el infrarrojo medio y lejano de siete RFD, usando los telescopios espaciales *Spitzer* y *Herschel*. La abundancia de HAP y fulerenos muestra evidencia de formación de estos últimos en el caso de fuentes individuales, pero no se ha encontrado una tendencia universal que conecte todas las RFD con respecto, ya sea al campo de radiación, o a la razón de este con respecto a la densidad de hidrógeno atómico (cantidad que se relaciona con la recombinación de HAP con hidrógeno). Las fuentes en las cuales se detectan con claridad las bandas de fulerenos tienen condiciones físicas consistentes con la deshidrogenización total de HAP grandes, el primer paso en la formación de fulerenos. Sin embargo, la abundancia de fulerenos y la falta de una tendencia general entre todas las RFD indican que otros parámetros, tales como la edad de la RFD, juegan un rol clave en el procesamiento de los HAP.

El capítulo III provee evidencia experimental de la formación de fulerenos a partir de HAP de gran tamaño. Comparando el patrón de fotodisociación en los espectros de masa de HAP y fulerenos, es claro que ambos muestran los mismos “números mágicos”. Estos corresponden a estructuras fullerénicas de mayor estabilidad con respecto a otras de masa similar. Ambas especies fueron también irradiadas usando luz con una longitud de onda de 532 nm, a la cual el fullereno C_{60}^+ no absorbe fotones. En fulerenos, la fragmentación se detiene completamente una vez que los productos alcanzan una masa correspondiente a C_{60}^+ , como era de esperar. Los HAP pueden disociarse más allá de este límite, pero el patrón de “números mágicos” desaparece y una importante cantidad de fragmentos con sesenta átomos de carbono permanece sin fragmentarse incluso a la más alta potencia del láser. Este trabajo experimental muestra una sólida evidencia en términos de la formación “de arriba hacia abajo” de fulerenos en el medio interestelar.

La deshidrogenización de HAP es un proceso crítico al abordar ambas interrogantes estudiadas en esta tesis. Es a la vez el primer paso en la formación de fulerenos y la instancia en la cual puede producirse hidrógeno molecular. En vista de esto, el capítulo IV presenta un estudio exhaustivo de la deshidrogenización de HAP. La pérdida de los cuatro primeros hidrógenos fue estudiada experimentalmente en una muestra de nueve HAP, con un énfasis particular en la razón entre pérdidas pares e impares, ya que estas llevan consigo información clave para entender la competencia entre la pérdida secuencial de hidrógeno atómico y la pérdida de hidrógeno molecular. En el caso de tres de los HAP, se usó un modelo (basado en cálculos químico-cuánticos) del proceso de fragmentación, incluyendo la posibilidad de que átomos de hidrógeno se muevan a lo largo del borde de la molécula. La comparación de los resultados experimentales y del modelo demuestran que el movimiento de átomos de hidrógeno es fundamental a la hora de explicar el proceso de fragmentación. Se observó a su vez que la formación de hidrógeno molecular se vuelve más importante cuanto mayor sea el tamaño del HAP en cuestión.

Para estimar la importancia de la formación de hidrógeno molecular a partir de HAP en el contexto de RFD densas, se utilizaron los resultados anteriores para modificar un modelo de fotodisociación de HAP en RFD. Una selección de tres HAP es presentada en el capítulo V, siendo ellos representativos de los posibles escenarios de deshidrogenización (ya sea dominada por pérdida de hidrógeno atómico, molecular o con alta competitividad entre ambos). En el caso de HAP en los cuales la pérdida atómica domina, o hay competencia entre los dos procesos, la eficiencia de formación de hidrógeno molecular no es significativamente distinta a la que ha sido derivada en otros estudios. Si la deshidrogenización es dominada por la pérdida de hidrógeno molecular, la eficiencia se incrementa en un factor ~ 20 . A pesar de que este aumento no es suficiente para explicar la tasa de formación observada, reduce en un gran margen la disparidad. Estudios futuros sobre la dependencia en tamaño de las tasas de disociación pueden, potencialmente, aclarar esta interrogante.

PUBLICATIONS

- *Dust-correlated centimetre-wave radiation from the M 78 reflection nebula.*
Castellanos, P.; Casassus, S.; Dickinson, C.; Vidal, M.; Paladini, R.; Cleary, K.; Davies, R. D.; Davis, R. J.; White, G. J.; Taylor, A. C.
2011, Mon. Not. R. Astron. Soc., Vol. 411, pp. 1137–1150
- *Dust-correlated cm wavelength continuum emission from translucent clouds ζ Oph and LDN 1780.*
Vidal, M.; Casassus, S.; Dickinson, C.; Witt, A. N.; **Castellanos, P.**;
Davies, R. D.; Davis, R. J.; Cabrera, G.; Cleary, K.; Allison, J. R.; Bond, J. R.;
Bronfman, L.; Bustos, R.; Jones, M. E.; Paladini, R.; Pearson, T. J.;
Readhead, A. C. S.; Reeves, R.; Sievers, J. L.; Taylor, A. C.
2011, Mon. Not. R. Astron. Soc., Vol. 414, pp. 2424–2435
- *C_{60} in photodissociation regions.*
Castellanos, P.; Berné, O.; Sheffer, Y.; Wolfire, M. G.; Tielens, A. G. G. M.
2014, Astrophys. J., Vol. 794, Art. 83
- *Laboratory formation of fullerenes from PAHs: Top-down interstellar chemistry.*
Zhen, J.; **Castellanos, P.**; Paardekooper, D. M.; Linnartz, H.;
Tielens, A. G. G. M.
2014, Astrophys. J. Lett., Vol. 797, Art. L30
- *Laboratory photo-chemistry of PAHs: Ionization versus fragmentation.*
Zhen, J.; **Castellanos, P.**; Paardekooper, D. M.; Ligterink, N.; Linnartz, H.;
Nahon, L.; Joblin, C.; Tielens, A. G. G. M.
2015, Astrophys. J. Lett., Vol. 804, Art. L7
- *Photo-fragmentation behavior of methyl- and methoxy-substituted derivatives of hexa-peri-hexabenzocoronene (HBC) cations.*
Zhen, J.; **Castellanos, P.**; Linnartz, H.; Tielens, A. G. G. M.
2016, Mol. Astrophys., Vol. 5, pp. 1–8
- *Infrared spectra of hexa-peri-hexabenzocoronene cations: HBC^+ and HBC^{2+} .*
Zhen, J.; **Castellanos, P.**; Bouwman, J.; Linnartz, H.; Tielens, A. G. G. M.
2017, Astrophys. J., Vol. 836, Art. 28

Publications

- *Laboratory gas-phase spectra of two astronomically relevant PAH cations: Diindenoperylene $C_{32}H_{16}^+$ and dicoronylene $C_{48}H_{20}^+$.*
Zhen, J.; Candian, A.; **Castellanos, P.**; Bouwman, J.; Linnartz, H.; Tielens, A. G. G. M.
2018, *Astrophys. J.*, Vol. 854, Art. 27
- *Photoinduced PAH dehydrogenation: The competition between H- and H₂-loss.*
Castellanos, P.; Candian, A.; Zhen, J.; Linnartz, H.; Tielens, A. G. G. M.
2018, *Astron. Astrophys.*, *in press*
- *Photoinduced PAH dehydrogenation: Molecular hydrogen formation in dense PDRs.*
Castellanos, P.; Candian, A.; Andrews, H.; Tielens, A. G. G. M.
2018, *Astron. Astrophys.*, *in press*

CURRICULUM VITAE

I was born in La Habana (Havana), Cuba on March 1st, 1987 to a Chilean mother and a Cuban father. Given the combined circumstances of the end of the Chilean dictatorship and the beginning of the Cuban Special Period following the fall of the Soviet Union, together with my mother and younger brother I moved to Santiago, Chile during the first half of the 90's. The first years in Chile we lived with my grandparents where my grandfather in particular had a hand in steering me towards science in general and astronomy in particular. I went to high school at the Instituto Nacional José Miguel Carrera, where the effort and encouragement of my family paid off and I was able to enroll in the the bachelor programme of Science with mention in Astronomy at Universidad de Chile. During the last few years of the bachelor, I worked together with Prof. dr. Simón Casassus on the continuum emission at 30 GHz; the anomalous microwave emission (AME). That was the first real encounter with research and what it entails, using radio observations from the Cosmic Background Imager (CBI) and mid-infrared data from *Spitzer* and *IRAS* in order to test for the hypothesis of the AME being due to very small, rapidly rotating dust grains. This work resulted on my first publication and my involvement on a separate project on the same topic, led by Dr. Matías Vidal, then a master student.

Afterwards, I applied and got enrolled in the Research Master in Astronomy at Leiden University, where I was able to study thanks to the Oort scholarship. I quickly forged friendships that last to this day and got involved in astrochemistry research, together with the work on the courses. I did my minor research project with Prof. dr. Michiel Hogerheijde, looking for emission lines of methanol in the disk of TW Hya using spectra observed with the James Clerk Maxwell Telescope and modeling the line emission using the Line Modeling Engine code (LIME). The major project was done under the supervision of Prof. dr. Alexander Tielens and it involved the search for the then recently detected C_{60} in photodissociation regions, using *Spitzer* mid-infrared spectral maps.

As a result of the work done during the Master programme I was offered a position for the PhD programme in Astronomy by Prof. Tielens, with partial funding from a Huygens fellowship. Here I worked on expanding the work done for the major research project into a fully fledged article which is included in this thesis. Even though I lacked the experience, I was interested in the experimental research done in the Laboratory for Astrophysics during the master and the possibility opened up for doing such work for my PhD. I was received there by Prof. dr. Harold Linnartz, who would also

Curriculum vitae

become my promotor, and by Dr. Junfeng Zhen. I started working with the instrument for photodynamics of PAHs (i-PoP) and, especially in the first year, I had to get myself up to speed on hands on laboratory work and on the topic of ion traps and mass spectrometry in particular. I was involved in several studies on the photodissociation of PAHs, including work done at the synchrotron facility SOLEIL in Paris, France.

Nearly every year during the PhD I have been involved in experimental work at the free electron laser for infrared experiments, FELIX, at Radboud University in Nijmegen. There the work has evolved from the first couplings of i-PoP with FELIX when studies of known systems were performed, to recording the IR spectrum of large PAHs and measurements of the spectrum of fragmentation products. These studies have involved close collaboration with Dr. Alessandra Candian in order to interpret the experimental results on the basis of density functional theory (DFT) calculations. I also spent a few months in Lyon, France, working together with Prof. dr. Franck Lépine and his group on femtosecond photodissociation dynamics of PAHs.

The research has involved a strong component of computational modeling. As part of the study on PAH dehydrogenation I have developed a comprehensive Monte-Carlo simulation code, which includes hydrogen roaming as well as multiple fragmentation channels, all based upon DFT calculation by Dr. Candian. Additionally, I have implemented modifications into the code for PAH fragmentation in PDRs created by Dr. Heather Andrews, in order to include the effect of PAH isomerization in an astronomical context.

ACKNOWLEDGMENTS

Properly acknowledging everyone who has, in one way or another, contributed to this thesis would make this book twice as long, but probably a far easier read. Considering this, I will try and summarize as much as possible what I am grateful for, and include by name those involved in it. If there are omissions (and there will be) please forgive me and know that it is not out of disregard; even nothing but a list of names would be a long undertaking and most of you know how bad I am at retaining names.

In the first place, I would like to thank Simón Casassus, with whom I worked in Chile, and who trusted me during the bachelor in such a way that made this PhD a possibility. I am very grateful to Alessandra as well, without her patience and dedication I doubt this thesis would have ever become a reality. Also to Junfeng, who eased me into transitioning from purely observational astronomy into hands-on laboratory work. With Jordy I had less time to work with, but the long conversations and discussions at coffee breaks that ended up in de Gouwe and the dinners with Wendy and Zoey were just perfect. I would like to thank as well all my colleagues at the Laboratory for Astrophysics and the ISM group, for sharing in with paper cakes, pizza meetings, day outs and many other occasions: Aart, Ainil, Cameron, Daniel, Danna, Dario, Gleb, Gwen, Héctor, Jeroen, Jerry, Kim, Kirstin, Ko-Ju, Martijn, Michał, Niels, Vincent, Xavier and others who have passed through both groups. Also the people whom I met all over the Netherlands and in plenty of different circumstances, not necessarily as part of the observatory, but who have been with me at some point: Anne, Daniel, Emanuele, Iva, Kaveh, Madusha, Marco, Mher, Nikita (большое спасибо за уроки!), Sayan, Sumit, Swasti, Vincent and Ylva.

The friends I made during the master have surprisingly stayed around or, at the very least, remained friends despite the distance. I am very grateful that the first people I met in this bizarre continent ended up being such a fantastic group, especially Francesco and Stefano, who somehow have managed never to get too far away from Leiden. Although in the case of Panchito the acknowledgments should go to Marta as well (I'll be waiting for October!). But there are many others: Agnès and her family, Isabelle, Jenny, Lucia, Naïla, Reinhard (who gave me a roof during some complicated times) and Stéphanie.

During the PhD experience, I had the chance to know more of Leiden, Europe and the world in general. Of course, I want to thank Vicente, my housemate during the first part of this process, who always had his good humor, the guitar and the spirit for an asado. Katka, for making a visit to the Balkans a real possibility and a more

Acknowledgments

than perfect experience, even in days when money was tight. Cláudio, Ece, Ines, Irene, James, Manuela, Matteo, Matthieu, Maren, Pelin, Ricardo, Sofia and so many others: thanks for all the dinners, parties and barbecues, but most of all for always being there. I will always be grateful to Müge, Monique, Ariane and Valeria for their company and for sharing for a while their own piece of the world.

Por supuesto también tengo que agradecer a toda la comunidad latina de Leiden y a sus miembros adoptivos (algunos ya mencionados), desde las más altas esferas de la realeza (Jéder) hasta el más bajo de los borrachos (Jorgito, tú sabes por qué). Nadie más puede mantener la fiesta y el baile andando incluso en estos inviernos gélidos. Especialmente quiero agradecer a Paula, con quien nos conocemos casi desde el principio; a Pedro, por tantos cigarros y conversaciones; y a Heather que siempre está para alegrar la vida. José, rata, te echamos de menos por acá, espero que pronto nos veamos con Pablito y Haydee. Carlos y Mary, ojalá que pronto vuelvan a algún lugar al que no sea tan difícil volver a encontrarnos. También agradecer a Álvaro, Aquiles, Camila, Carmen, Claudio, Cristi, Francisca, Francisco, Gaby, Igone, Javi, Kathy, Lina, Liz, María, Marta, Max, Santiago, Seba, Tania, Yanett y tantos otros.

De Chile, siempre están presentes los participantes de las tertulias en Santa Elvira y el Infierno. Muchos cariños en particular a Andrés (espero que nos veamos pronto por el sudeste asiático), Caro (hace tiempo que no sé de ti, pero ojalá todo ande bien), Coke (ya puedes ver que todas las tesis se acaban), Gladys (espero llegar a tocar la puerta para conversar un día no muy lejano) y Julián con su familia (gracias por el tremendo viaje y ojalá otro salga pronto). A Ricardo, que es y ha sido siempre un segundo padre; sigue cuidándote porque quiero verte (y bien) en el próximo viaje. A Camilo también, mucha suerte en tu propia experiencia con un doctorado. A Sandy, muchísimas gracias por las veces en que me has hecho esperar y más aún por aquellas en que llegas a tiempo; gracias por estar ahí siempre, guachita. Karla y Jero, les agradezco haberme recibido tantas veces en su departamento y por las conversaciones hasta la madrugada. Muchas gracias a Alberto, Eloísa, Mayra y Virgen, que desde Cuba también han seguido este proceso.

Finalmente, quiero agradecer a toda mi familia, ahora sí consanguínea. A mi tía Chichi, por su ayuda al escribir y corregir la carta de presentación y el currículum que me dieron la entrada al magíster. A mis hermanos, Ana, Manuel y Orlando: sé lo malagradecido que soy y lo seguido que me desaparezo, pero no saben lo bien que me hace oírlos cada vez que hablamos, por corto que sea. Viejita querida, que tantas preocupaciones te he hecho pasar, gracias por apoyarme siempre y por confiar en mí, acá jamás hubiese llegado de no ser por ti. Y, por supuesto, a los que ya no están; a mis abuelos y a mi padre.

¡Gracias a todos!